FM Airborne Passive Radar

James W. A. Brown

A thesis submitted to University College London for the degree of
Doctor of Philosophy in Electronic Engineering

Department of Electronic and Electrical Engineering
University College London

April 2013

I, James W. A. Brown confirm that the work presented in this thesis is my own. Where information has been derived from other sources, I confirm that this has been indicated in the thesis.

James W. A. Brown

London, April 2013

Abstract

The airborne application of Passive Bistatic Radar (PBR) is the latest evolution of the now established international interest in passive radar techniques. An airborne passive system is cheaper to construct, easier to cool, lighter and requires less power than a traditional active radar system. These properties make it ideal for installation on an Unmanned Aerial Vehicle (UAV), especially for the next generation of Low Observable (LO) UAVs, complementing the platforms LO design with an inherently Low Probability of Intercept (LPI) air-to-air and air-to-ground sensing capability.

A comprehensive literature review identified a lack of practical and theoretical research in airborne passive bistatic radar and a quantitative model was designed in order to understand the theoretical performance achievable using a hypothetical system and FM as the illuminator of opportunity. The results demonstrated a useable surveillance volume, assuming conservative estimates for the receiver parameters and allowed the scoping and specification of an airborne demonstrator system.

The demonstrator system was subsequently designed and constructed and flown on airborne experiments to collect data for both air-to-air and air-to-ground operation analysis. Subsequent processing demonstrated the successful detection of air targets which correlated with the actual aircraft positions as recorded by a Mode-S/ADS-B receiver. This is the first time this has been conclusively demonstrated in the literature.

Doppler Beam Sharpening was used to create a coarse resolution image allowing the normalised bistatic clutter RCS of the stationary surface clutter to be analysed. This is the first time this technique has been applied to an airborne passive system and has yielded the first quantitive values of normalised bistatic clutter RCS at VHF.

This successful demonstration of airborne passive radar techniques provides the proof of concept and identifies the key research areas that need to be addressed in order to fully develop this technology.

Acknowledgements

Publications

The following papers were published as a result of this PhD research:

J. Brown, K. Woodbridge, A. Stove, and S. Watts. "Air target detection using airborne passive bistatic radar". *Electronics Letters*, 46(20):1396-1397, 30 2010.

J. Brown, K. Woodbridge, H. Griffiths, A. Stove, and S. Watts. "Passive bistatic radar experiments from an airborne platform". *IEEE Aerospace and Electronic Systems Magazine Special Issue on PCL*, 2012.

The following paper was presented at Radar 2012 and shortlisted for the best student paper prize:

J. Brown, K. Woodbridge, A. Stove, and S. Watts. "VHF airborne passive bistatic radar ground clutter investigation". *IET Radar Conference 2012*. October 22nd to 25th 2012.

Contents

List of Figures

List of Tables

Nomenclature

Δf_B Doppler resolution

σ_B Bistatic radar cross section

$\mathbf{L}$ Baseline vector from the receiver to the transmitter

$\mathbf{P} = [x, y, z]^T$ Target coordinates

$\mathbf{R} = [x_R, y_R, z_R]^T$ Receiver coordinates

$\mathbf{T} = [x_T, y_T, z_T]^T$ Transmitter coordinates

β Bistatic angle

$\Delta \theta_R$ Receiver beamwidth

$\Delta \theta_T$ Transmitter beamwidth

ΔR_B Bistatic range resolution

ΔR_M Equivalent monostatic range resolution

λ Transmitted signal centre wavelength

ρ surface voltage reflection coefficient

σ_c^0 Normalised clutter cross-section

τ Compressed pulsewidth

τ Time delay

τ_{int} Coherent integration time

θ_R Angle between target and baseline for the receiver

A_c Clutter cell area

B Transmitted signal bandwidth

c Speed of light ($3\text{x}10^8$ m/s)

F Receiver noise factor (linear units)

f_B' Relative bistatic Doppler shift

f'_t, f'_r transmitter and receiver voltage gain in the direction of the multipath

f_B Bistatic Doppler shift of target, Hz

F_P Propagation factor

f_t, f_r transmitter and receiver voltage gain in the direction of the target respectively

G_R Receiver antenna gain

G_T Transmit antenna gain

K Boltzmann constant ($1.38\text{x}10^{-23}$)

L Length of baseline

L_S Receiver system loss factor ($L_S \geq 1$)

P_D Probability of detection

P_T Peak transmit power

P_{FA} Probability of false alarm

P_{LOS} Line-of-sight received power

P_{pf} Pattern propagation factor

R_B Bistatic range

R_R Target-to-receiver range

R_T Target-to-transmitter range

T_0 Noise reference temperature (290 K)

$\boldsymbol{\beta}$ Bistatic bisector unit vector

$\mathbf{v}_R = [v_x^R, v_y^R, v_z^R]^T$ Receiver velocity vector

$\mathbf{v} = [v_x, v_y, v_z]^T$ Target velocity vector

ADC   Analogue-to-digital converter

AEW   Airborne Early Warning

AF   Ambiguity function

AGL   Above Ground Level (eg 200 m AGL)

ARD   Amplitude Range Doppler Surface

DAB   Digital Audio Broadcasting

DR   Dynamic range

DSI   Direct Signal Interference

FM   Frequency Modulation

GPS   Global Positioning System

GPS   Global Positioning System

ISAR   Inverse Synthetic Aperture Radar

LO   Low Observable

LoS   Line-of-Sight

LPI   Low Probability of Intercept

PBR   Passive Bistatic Radar

PBR   Passive Bistatic Radar

PCL   Passive Coherent Location (PBR is the preferred term in this work)

RCS   Radar Cross Section

RFI   Radio Frequency Interference

SAR   Synthetic Aperture Radar

SCR   Signal-to-clutter ratio

SFN   Single Frequency Network

SIR   Target signal to direct signal interference ratio

UAV   Unmanned Aerial Vehicle

UCAS   Unmanned Combat Air System

VHF   Very High Frequency

Chapter 1

Introduction

1.1 Overview and Motivation

The airborne application of Passive Bistatic Radar (PBR) is the latest evolution of the now established international interest in passive radar techniques. Implicit in PBR operation is the ability to operate a surveillance system by exploiting ambient spectrum, such as communication signals, terrestrial broadcasts or satelliteborne GPS signals. Passive techniques remove the need for the system to have a dedicated transmitter hence the system is cheaper to construct, easier to cool, lighter and requires less power than a traditional active radar system. These properties make it ideal for installation on an Unmanned Aerial Vehicle (UAV), High Altitude Platform (HAP) or light aircraft; providing a Low Probability of Intercept air-to-air and air-to-ground surveillance capability to augment the platform's active systems.

Airborne passive radar is an attractive system for a military aircraft operating covertly in enemy airspace. Firstly, since the receiver is mobile, it can be sited as required to give the necessary air and ground coverage. Also, the relative motion of the system can be exploited and Synthetic Aperture Radar (SAR) and Inverse Synthetic Aperture (ISAR) imaging techniques employed to produce ground imagery. Secondly, the current significant investment in Low Observable (LO) air frames such as the F-35 Joint Strike Fighter and the next generation of Unmanned Combat Air Systems (UCAS)[1] requires a parallel investment in Low Probability of Intercept (LPI) sensor systems to allow the aircraft to sense their surroundings and potential threats, without signing their presence. From this stand-point, a passive system that can provide an Airborne Early Warning (AEW) and imaging capability,

---

[1]http://www.baesystems.com/product/BAES_020273/taranis

would be a valuable adjunct to the conventional onboard active systems.

Broadcast FM has been chosen for this research for a number of practical reasons. Firstly, it is ubiquitous both in developed and developing countries therefore a system developed for FM could potentially be employed in a wider range of locations than for other less popular broadcast schemes. Digital Audio Broadcasting (DAB) radio signals, for example, tend to be limited to developed countries. Secondly, for a given antenna size the correspondingly poor directivity at VHF means that there is likely to be considerable illumination above the horizon, as required for the detection of airborne targets. It is worth remembering that broadcast systems are designed to transmit to ground based receivers therefore higher frequency broadcasts such as DAB allow better directivity, but poorer above horizon illumination and hence a reduced detection range for PBR application. Thirdly, the multifrequency network implementation of FM transmitters means that the source of the transmitting signal can be uniquely identified, which is crucial for target location, something not as easy to do when using single frequency network (SFN) systems such as the DAB standard.

Conventional radars are typically used for safety critical applications such as air traffic management or air-to-air collision avoidance. For a passive radar system to be reliable, the illuminating signal needs to be available all the time, it needs to illuminate a useful volume and have a favourable modulation. From a military perspective, in order to counter the use of PBR systems, a nation may decide to turn off broadcast or communication signals, hence removing the illuminator. An airborne passive radar therefore needs to use an illuminator or illuminators that will always be present. Because FM receivers are relatively simple, cheap and importantly, are present in most households, FM is seen to be the means of mass communication and propaganda dissemination of last resort. Therefore it is likely that a government would be resistant to turning the FM broadcast system off as a passive radar counter measure, making FM potentially a more reliable illuminator than GPS or DAB signals.

The lack of work in the open literature on airborne passive radar means that in order for this technology to be understood and exploited, a comprehensive investigation into the system performance, the illuminator and the operating environment are required. This thesis provides the proof of concept of airborne passive bistatic radar and is a first step in developing the next generation of airborne radars with a passive LPI mode of operation.

1.2 Aims

The purpose of this course of research was to demonstrate the successful operation of an airborne passive bistatic radar using FM broadcasts as the illuminator. To achieve this goal, the following aims were set:

1. Summarise the state of the art of airborne passive radar, ground based passive radar and airborne bistatic radar. This includes examining the hardware, experimental results and the associated processing techniques

2. Develop a simulation suite to model the performance of an airborne passive radar for given illuminator parameters, receiver dynamics and target flight paths

3. Design and construction of an airborne demonstrator system

4. Carry out experimental flight trials using the demonstrator system in order to collect airborne VHF data

5. Process experimentally obtained data and analyse for:

    i. Detection of air targets

    ii. Imaging and characterisation of ground clutter

    iii. Estimates of normalised clutter cross-section.

1.3 Layout of Thesis

The layout of this thesis mirrors the approach taken during the course of research. A detailed introduction to the concept and technical theory of bistatic radar is presented in the first half of Chapter 2. Although this is derived from standard text book material, it highlights the specific conventions and terminology employed in the remainder of the thesis. The second half of Chapter 2 examines the relevant literature in passive ground based and airborne research and summarises the state of the art of airborne passive bistatic radar systems and techniques.

In Chapter 3, the theory and prior work is developed into a simulation suite allowing the system metrics to be calculated for a given scenario. The simulation is tailored specifically to the intended trials location and aircraft. The results of the simulation confirmed that a relatively simple two-channel receiver could achieve a usable performance. The design parameters from the simulation stage of Chapter 3 were then used to specify the receiver

design, as discussed in Chapter 4. Here the various design choices and compromises as well as the receiver acceptance testing are detailed. The simulation was then run using the measured receiver parameters and the intended trials location to ensure that the system would work as required.

Two airborne experimental data collection campaigns support this work and these are described in detail in Chapter 5. The air target detection processing is described and the experimental results are detailed in Chapter 6. The results of this chapter demonstrate the first documented air target detection from an airborne receiver. Chapter 7 details the development of a coarse imaging algorithm of the stationary clutter and demonstrates its application on the experimentally collected data. This imaging technique is then used to derive estimates for the clutter cross-section magnitude and its variation with bistatic angle. Chapter 8 brings together the main conclusions from this work as a whole and identifies the priority areas for future research.

1.4   Contributions Made by this Thesis

This work has made five key contributions to the field of airborne passive radar, it has:

1. Developed a low cost lightweight air mobile passive FM receiver

2. Developed novel signal processing algorithms for passive air target detection and ground imaging

3. Demonstrated the first detection of an air target using an airborne FM passive bistatic radar

4. Demonstrated the first Doppler beam sharpened image of stationary ground clutter using an airborne FM passive bistatic radar

5. Quantified the estimated levels of clutter cross-section variation with bistatic angle.

This work has contributed two journal publications [1, 2] and a conference publication [3] which was shortlisted for the best student paper award. Additionally the author has presented this work to the NATO SET-186 panel on Airborne Passive Radar and its Applications, to the US Air Force Research Laboratory, Dayton, Ohio, and to the European passive radar community at an FHR PCL focus day.

Chapter 2

Background

2.1 Bistatic Radar Theory

This section introduces the conceptual, theoretical and mathematical descriptions of PBR operation. A familiarity with these will allow the literature review to fully explore pertinent topics without necessitating extra explanation and also form a basis for developing these ideas and equations later in the thesis. This work concentrates on a specific implementation of passive bistatic radar where the target and receiver are mobile and the transmitter is stationary and non-cooperative. In this section the required theory in the detail necessary for this research is described; for a broader overview on bistatic radar consult [4].

2.1.1 Geometry Definition

The relative position and motion of the transmitter, target and receiver is termed the bistatic geometry. The bistatic geometry fundamentally influences the performance of the system in terms of detection range and resolution. Historically a north referenced bistatic geometry [4, 5] is employed to describe the properties of a bistatic system, however it is an abstract description of the bistatic geometry and is not a suitable method for implementation in a practical system. In this work, a vector approach is used as the transmitter and receiver position updates are available as a full state vector. The following definition of the geometry is used throughout this thesis where a bold typeface denotes a vector, as opposed to a scalar, quantity.

The receiver is located at $\mathbf{R} = [x_R, y_R, z_R]^T$ where x_R, y_R and z_R are the Cartesian coordinates of the aircraft position, where x points towards Grid North, y East and z the altitude, perpendicular to the x-y plane. Similarly the phase centre of the transmitter's
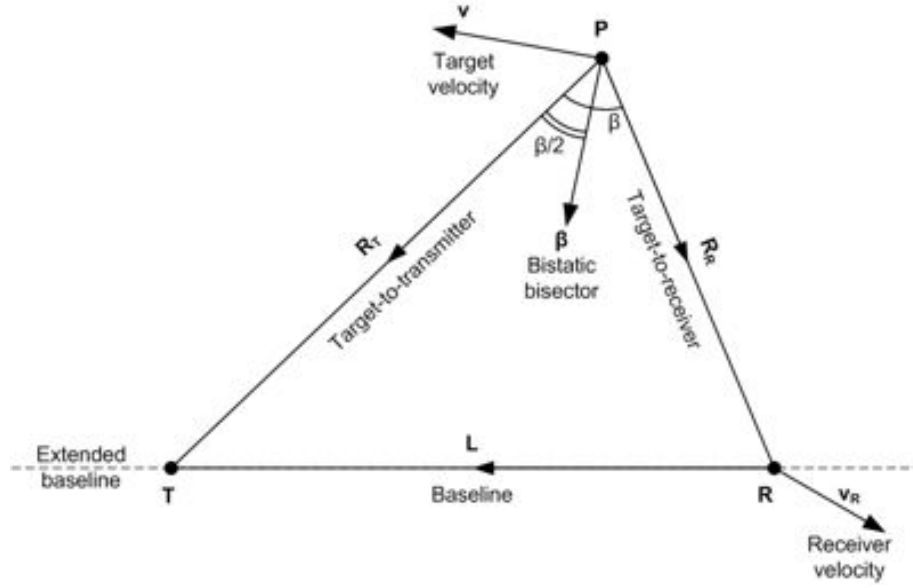
Figure 2.1: Bistatic geometry and vector definition

antenna, $\mathbf{T}$, is at $\mathbf{T} = [x_T, y_T, z_T]^T$ and the target, $\mathbf{P}$ is at $\mathbf{P} = [x, y, z]^T$. Where $(.)^T$ is the transpose operator. The receiver has velocity $\mathbf{v}_R = [v_x^R, v_y^R, v_z^R]^T$ and the target has velocity $\mathbf{v} = [v_x, v_y, v_z]^T$. With reference to Figure 2.1 the following quantities are defined. The baseline, $\mathbf{L}$, is defined as the vector from the receiver to the transmitter with length L , as defined in Equation 2.1.

$$L = |\mathbf{T} - \mathbf{R}| = \sqrt{(x_T - x_R)^2 + (y_T - y_R)^2 + (z_T - z_R)^2} \tag{2.1}$$

Similarly the target-to-transmitter and target-to-receiver ranges are defined as shown in Equations 2.2 and 2.3.

$$R_T = |\mathbf{T} - \mathbf{P}| = \sqrt{(x_T - x)^2 + (y_T - y)^2 + (z_T - z)^2} \tag{2.2}$$

$$R_R = |\mathbf{R} - \mathbf{P}| = \sqrt{(x_R - x)^2 + (y_R - y)^2 + (z_R - z)^2} \tag{2.3}$$

The bistatic angle, β, is the angle between the target-to-receiver and target-to-transmitter vector as shown in Equation 2.4. The bistatic angle varies between $180°$ when the target is on the baseline, to $0°$ when the target is on the extended baseline, or pseudomonostatic region.

$$\beta = \cos^{-1} \frac{\mathbf{R_T} \cdot \mathbf{R_R}}{R_R R_T} \tag{2.4}$$

The bistatic bisector unit vector, $\boldsymbol{\beta}$ is the unit vector along the bistatic bisector towards

the baseline as shown Figure 2.1 and Equation 2.5.

$$\boldsymbol{\beta} = \frac{\mathbf{R_R} + \mathbf{R_T}}{|\mathbf{R_R} + \mathbf{R_T}|} \tag{2.5}$$

2.1.2 Range Relationships

Cross-correlation of the direct signal and the target return allows the measurement of the bistatic range to the target, R_B , to be estimated. The bistatic range is the sum of the target-to-transmitter range, R_T and the target-to-receiver range, R_R , Equation 2.6.

$$R_B = R_T + R_R \tag{2.6}$$

For a given bistatic range and receiver and transmitter location, an ellipsoid defines an isorange surface, similar to the isorange sphere for a monostatic radar. Assuming that the location of the transmitter and receiver is known, the target-to-receiver distance can be calculated for a given angle with respect to the baseline, θ_R , as shown in Equation 2.7. In reality, θ_R can be estimated using Angle of Arrival information at the receiver.

$$R_R = \frac{R_B^2 - L^2}{2(R_B - L\cos\theta_R)} \tag{2.7}$$

The resolution of a radar is the minimum separation between point targets that allows them to be individually distinguished by radar processing in both range and Doppler. By convention, the range resolution of a pulsed monostatic radar, ΔR_M, is defined as $c\tau/2$ where c is the speed of light and τ is the compressed pulsewidth. Two point scatterers in the radar-to-target line of sight can be individually detected if two distinct pulses can be detected at the receiver therefore the minimum separation is a single pulsewidth in time or ΔR_M in space. The equivalent separation in a bistatic receiver is referenced to the bistatic bisector-to-target line of sight and leads to two concentric ellipses as shown in Figure 2.2. The bistatic range resolution, ΔR_B, can be approximated as Equation 2.8, where it can be seen that the best case range resolution occurs when β is equal to 0 and the bistatic range resolution becomes that of a monostatic system. The line at $\beta = 0$ is an extension of the baseline and is termed the pseudomonostatic region. As the bistatic angle approaches $180°$, ΔR_B approaches infinity and the approximation breaks down, a thorough analysis is provided in [4].

$$\Delta R_B = \frac{c\tau}{2\cos(\beta/2)} = \frac{c}{2B\cos(\beta/2)} = \frac{\Delta R_M}{\cos(\beta/2)} \tag{2.8}$$
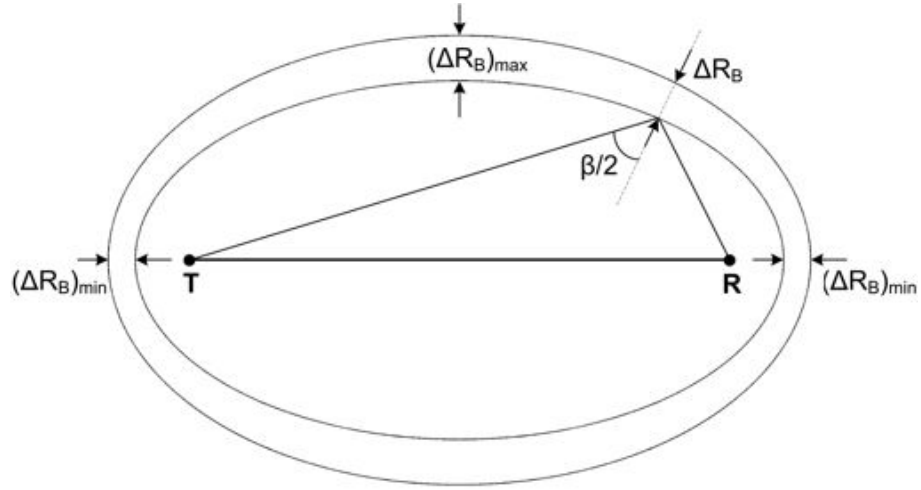
Figure 2.2: In plane range resolution

2.1.3   Doppler Relationships

The bistatic Doppler shift of a target, f_B, is proportional to the rate-of-change of bistatic range, as described by Equation 2.9.

$$f_B = \frac{1}{\lambda} \frac{dR_B}{dt} = \frac{1}{\lambda} \left[\frac{dR_T}{dt} + \frac{dR_R}{dt} \right] \tag{2.9}$$

For a mobile receiver and target, the Doppler shift is dependent on the receiver and target velocities. The rate-of-change of the target-to-transmitter path is due solely to the target motion and quantified as the projection of the target velocity vector on to the target-to-transmitter vector, as shown in Equation 2.10.

$$\frac{dR_T}{dt} = \frac{\mathbf{v} \cdot \mathbf{R_T}}{R_T} \tag{2.10}$$

The rate-of-change of the target-to-receiver path is due to both the target and receiver motion, therefore Equation 2.11

$$\frac{dR_R}{dt} = \frac{\mathbf{R_R} \cdot (\mathbf{v} - \mathbf{v_R})}{R_R} \tag{2.11}$$

It follows therefore that the bistatic Doppler shift of the target is described as Equation 2.12.

$$f_B = \frac{1}{\lambda} \left[\frac{\mathbf{v} \cdot \mathbf{R_T}}{R_T} + \frac{(\mathbf{v} - \mathbf{v_R}) \cdot \mathbf{R_R}}{R_R} \right] \tag{2.12}$$

The cross-correlation matched filtering processing employed in this work yields the relative bistatic Doppler shift, f'_B, which is the bistatic Doppler shift of the target signal relative to the Doppler shift of the direct signal from the transmitter.

$$f'_B = \frac{1}{\lambda} \left[\frac{\mathbf{v} \cdot \mathbf{R_T}}{R_T} + \frac{(\mathbf{v} - \mathbf{v_R}) \cdot \mathbf{R_R}}{R_R} - \frac{\mathbf{v_R} \cdot \mathbf{L}}{L} \right] \tag{2.13}$$

The bistatic Doppler resolution of the system, Δf_B, is dependent on the coherent integration time, τ_{int}, as shown in Equation 2.14.

$$\Delta f_B = \frac{1}{\tau_{int}} \tag{2.14}$$

The longer the integration time, the higher the Doppler resolution however it is important to ensure that the scene can be regarded as stationary throughout the coherent processing interval.

2.1.4 Sensitivity

As for monostatic radar, the radar equation gives an insight into the potential operating range of a passive bistatic radar. At this stage the exact nature of the transmitted signal is not important and the transmitter is modelled as a point source with a known Effective Radiated Power (ERP) in the direction of the target, transmitting a white noise waveform with a given centre frequency and bandwidth. The quantity of interest is the power at the receiver for a given geometry, target and transmitter. For a free-space scenario, the relationship can be developed as follows. Assuming a transmitter of peak transmit power P_T transmits a signal of bandwidth B at centre wavelength λ, with an omnidirectional antenna of gain G_T. The target lies at a distance R_T and has a bistatic Radar Cross Section (RCS), σ_B. The bistatic RCS is a measure of the amount of power reflected in the direction of the receiver and has units of area. The power reflected towards the receiver spreads omnidirectionally and at the receiver, a distance R_T from the target, the receive antenna with a gain of G_R intercepts the signal.

$$P_R = \frac{P_T G_T}{4\pi R_T^2} \sigma_B \frac{1}{4\pi R_R^2} \frac{G_R \lambda^2}{4\pi} = \frac{P_T G_T G_R \lambda^2}{(4\pi)^3 R_T^2 R_R^2} \tag{2.15}$$

As the transmitter and receiver are brought closer together, the baseline is reduced and $R_T = R_R$ and Equation 2.15 reduces to the monostatic case as expected. To account for

the non-ideal propagation in a real world environment, a one-way propagation factor, F_P, can be included in the numerator. This accounts for physical effects such as the curvature of the Earth, multipath interference, terrain scattering and diffraction and other natural environmental factors. For the purpose of this work, the propagation factor models the effect of multipath between the transmitter, target and receiver.

Signal-to-Noise Ratio

The signal-to-noise ratio is an important metric for a radar system since it determines the fidelity of many radar signal processing operations. As an example, for noise limited detection and a specified probability of false alarm, P_{FA}, the probability of detection, P_D, increases as SNR increases. Here the SNR is calculated for receiver thermal noise where the target echo power received at the receiver is calculated as Equation 2.15 and the thermal noise power in the receiver is Equation 2.16

$$P_N = kT_0BF \tag{2.16}$$

Where k is Boltzmann's constant, T_0 is the noise reference temperature (290 K), B is the receiver noise bandwidth and F is the receiver noise factor. The SNR therefore is the ratio of received power to noise power, as shown in Equation 2.17 where the propagation factor, F_P and a loss term, L_S, to represent receiver system losses, have been included ($L_S \leq 1$).

$$SNR = \frac{P_R}{P_N} = \frac{P_T G_T G_R F_P \sigma_B}{(4\pi)^3 R_T^2 R_R^2 kT_0BFL_S} \tag{2.17}$$

To increase the probability of detection for a given scenario it is necessary to maximise the SNR of the target returns. Coherently processing N samples gives rise to a processing gain, which increases the SNR. If the target and receiver are stationary then the target samples add in phase, increasing the target power by a factor N^2, however the noise samples add incoherently increasing the noise power by a factor of N. The net result is an increase in target signal-to-noise by a factor of N or $10\log_{10} N$ dB. The coherent processing gain, G_P, requires the scene to be stationary or near stationary for the duration of the coherent processing interval, τ_{int}. The maximum integration time for a target is defined as the length of time for which the phase difference of the target return does not exceed $\pi/2$. For a given radial target acceleration, a, the coherent integration time is expressed as Equation 2.18,
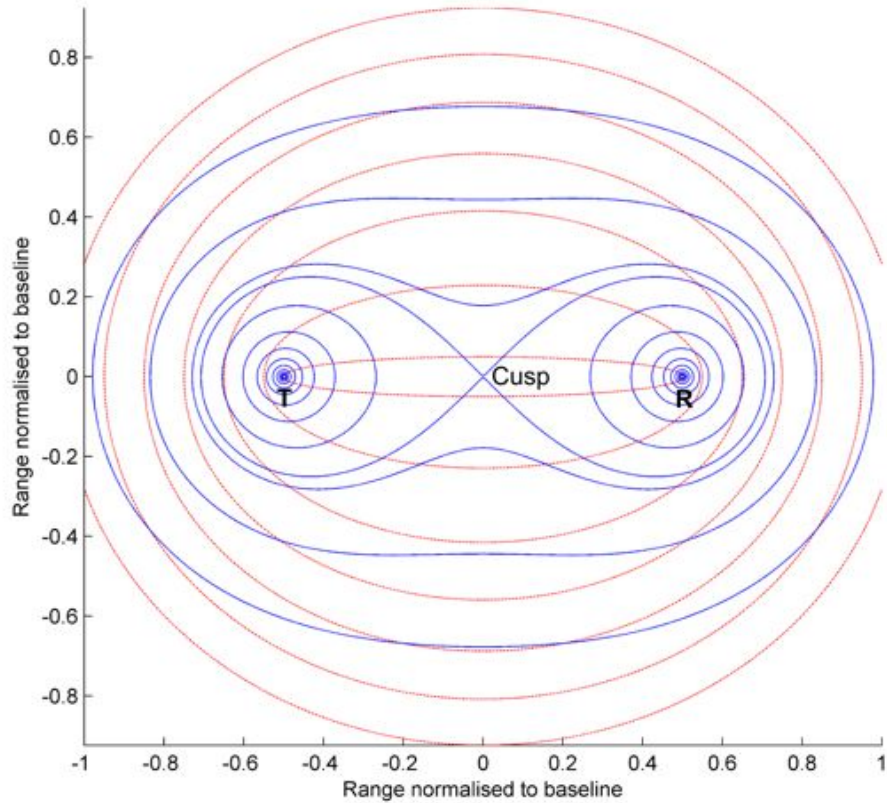
Figure 2.3: Cassini Ovals (blue line) describing contours of constant SNR for a transmitter and receiver geometry. The contours of constant range (red dotted lines) are not collinear with the contours of constant SNR.

as derived in [6].

$$\tau_{int} \leq \sqrt{\frac{\lambda}{2a}} \tag{2.18}$$

For a monostatic radar, contours of constant SNR, in 2D, form concentric circles centred on the radar as do contours of constant range. When the receiver and transmitter are separated, as in a bistatic radar, isorange and constant SNR contours are not collinear. Contours of constant bistatic range are described as $R_T + R_R =$ constant and contours of constant SNR are Cassini Ovals where $R_T R_R =$ constant. With reference to Figure 2.3, three distinct operating regions are defined: the transmitter-centred region, the receiver-centred region and the cosite region. The receiver-centred region can be used for passive situational awareness and penetrating an airspace with a silent receiver and stand-off transmitter. The transmitter-centred region can be used for monitoring activity in the vicinity of a non-cooperative transmitter and also passive situational awareness. The cosite region can be used for medium range air defence and forward scatter fences.

Signal-to-Interference Ratio

The target echo, not only has to compete with the thermal noise in the receiver and ambient RF interference (RFI) but also with the direct signal from the transmitter. The direct power received from the transmitter, P_{LOS} follows a line-of-sight path and is calculated as Equation 2.19.

$$P_{LOS} = \frac{P_T G'_T G'_R \lambda^2}{(4\pi)^2 L^2} \tag{2.19}$$

where G'_T and G'_R are primed to signify that the direct path gain will typically be different to the gain for the target signals. Unlike thermal noise, the direct signal is subject to the same integration gain as the echo signal and therefore there is no net improvement in SIR due to integration. The SIR is therefore defined as Equation 2.20 where L is the baseline distance.

$$SIR = \frac{P_R}{P_{LOS}} = \frac{G_T G_R L^2 \sigma_B}{4\pi G'_T G'_R R_T^2 R_R^2} \tag{2.20}$$

The SIR is a useful indication of the likely dynamic range required in the receiver's Analogue-to-Digital Converter(ADC) the ratio of the largest signal a digitiser can convert to the smallest signal is termed the Dynamic Range (DR) . The DR is related to the number of bits in the ADC with each bit adding 6 dB of sensitivity relative to the quantisation noise of the ADC. If the SIR is smaller than the reciprocal of the DR, the target will be undetectable, which is a common problem in PBR systems. In order to reduce the DR requirements, the direct signal can be reduced in power through a number of techniques. The effect of these techniques on the SIR can be included by introducing a factor, L_{canc}, in the denominator where $L_{canc} \leq 1$.

2.1.5 Clutter

The transmitted signal illuminates not only the target but the surrounding environment. In an urban setting for instance, a monostatic radar would receive returns from unwanted sources such as the ground, precipitation, birds etc. The returns can be minismised by tailoring the transmit and receive patterns to ensure that on transmit, only the area of interest is illuminated and on receive, the antenna is insensitive to directions not of interest. These unwanted returns are called clutter and specifically clutter from the ground is called surface clutter.

The power from surface clutter will compete with any target signal power and the effect can be examined by calculating the signal-to-clutter ratio (SCR) for a certain scenario. As

with SNR and SIR, this is another performance limiting factor of a radar system. The size of the area illuminated is called the clutter cell and this can be determined by the beamwidth, range, range resolution and Doppler resolution.

For the case where the clutter cell is beamwidth limited, the cell area, A_c, is the patch illuminated by the main beam on the ground. For low grazing angles this patch approximates a parallelogram with area (2.21)

$$A_c = \frac{(R_T \Delta\theta_T)(R_R \Delta\theta_R)}{\sin\beta} \tag{2.21}$$

where $R_T \Delta\theta_T$ and $R_R \Delta\theta_R$ are the cross-range dimensions of the beamwidths at the clutter cell. The 3 dB beamwidths, in radians, of the transmit and receive pattern being $\Delta\theta_T$ and $\Delta\theta_R$ respectively. To calculate the amount of power scattered in the direction of the receiver, the backscatter or bistatic RCS of the surface is required. The bistatic RCS can be expressed as $\sigma_c = \sigma_c^0 A_c$, where σ_c^0 is the normalised clutter cross-section and A_c is (2.21). σ_c^0 is unitless and dependent on many factors including wavelength, surface type, surface roughness, incident angle, incident polarisation and bistatic angle. This dependence on a number of factors means that relatively little data exists on the bistatic clutter cross-section of surfaces. Willis describes prominent measurement campaigns of land and sea clutter at X-band in [4] and Weiner in Chapter 9 of [7].

The Signal-to-Clutter ratio (SCR) is the ratio of the echo power from a target at a certain bistatic range to the power scattered from the ground at an equal bistatic range and is calculated as (2.22).

$$P_c = \frac{P_T G_T G_R \lambda^2}{(4\pi)^3 R_T^2 R_R^2} \sigma_c^0 A_c \tag{2.22}$$

2.2 Passive Bistatic Radar

Passive Bistatic Radar (PBR) performance is reliant on the properties of the illuminating waveform and is intrinsically a non-cooperative system. Illuminators of opportunity range from commercial broadcast transmissions to communication signals. Radar signals from weather radar or civil and military radar systems also offer potential for exploitation by PBR systems however they will not be considered here.

The important parameters of the transmitted signal are the transmit power and radiation pattern, modulating bandwidth and modulation type. Table 2.1 shows the specification of a number of illuminating signals as presented by Griffiths and Baker [8].

Transmitter	Typical Frequency	Modulation	Typical ERP
HF	10 - 30 MHz	DSB AM, 9 kHz	50 MW
FM	100 MHz	FM, 50 kHz	250 kW
UHF TV	550 MHz	5.5 MHz	1 MW
DAB	220 MHz	COFDM, 1.536 MHz	10 kW
Digital TV	750 MHz	COFDM, 6 MHz	8 kW
GSM	900 MHz, 1800 MHz	GMSK, 200 kHz	100 W
3G	2 GHz	CDMA, 3.84 MHz	100 W
WiFi	2.4 GHz	DSSS/OFDM, 20 MHz	10 W

Table 2.1: Potential illuminators of opportunity

The transmit power determines the sensitivity of the system. As shown in (2.17), for a given target and bistatic geometry the higher the transmit power, the larger the bistatic range targets can be detected at. For the same scenario however, the larger the transmit power, the higher the Direct Signal Interference (DSI) at the receiver and therefore more exacting DSI suppression techniques will be required in order to ensure a respectable operating range. The modulation type determines the range resolution and range-Doppler ambiguity performance of the system once the signals have been processed by the receiver. The radar processing aims to act on the received signal so as to maximise the SNR. This is done through a matched filter, the impulse response of which is matched to the time-reversed and conjugated transmitted signal [9]. The response of the matched filter, for a delay and Doppler frequency different to the nominal design values, can be evaluated by examining the Ambiguity Function (AF) of the signal. The delay, τ corresponds to the range of the target and the Doppler frequency, f, corresponds to the radial component of the target motion. The ambiguity function for a monostatic radar is shown in Equation 2.23.

$$|\chi(\tau, f)|^2 = \left| \int_{-\infty}^{\infty} u(t)u^*(t-\tau)e^{-j2\pi ft}dt \right|^2 \tag{2.23}$$

For a zero-Doppler cut through the AF as shown in Figure 2.4, Equation 2.23 simplifies to the squared modulus of the auto-correlation function of $u(t)$. The plot of Figure 2.4 demonstrates a typical zero-Doppler cut through the AF for an FM waveform. By convention the bistatic range resolution is measured as the distance to the first null, in this case the best case range resolution is 13.5 km. This applies when the geometry is close to monostatic. A zero-delay cut is the Fourier transform of $|u(t)|^2$.

In bistatic radar the AF is geometry dependent and a more general expression takes into account the variation in range and Doppler resolution with target position. This has been derived and analysed in [10] and is not presented here.
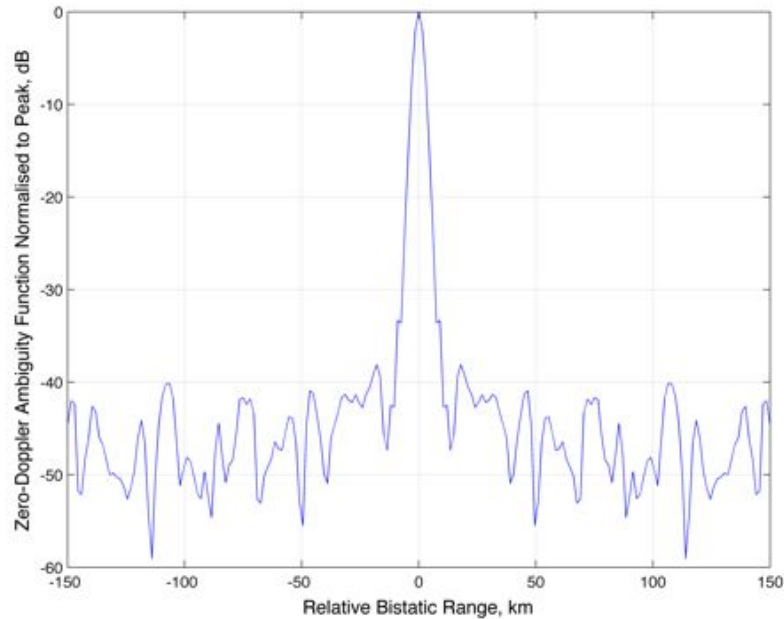
Figure 2.4: A typical zero-Doppler cut through the Ambiguity Function for a broadcast FM waveform.

Digital signals such as DAB and DVB-T have a band-limited near white spectrum and therefore have very good auto-correlation properties. They also have a constant, relatively large, modulating bandwidth that is essentially independent of the transmitted information, unlike analogue FM broadcasts. For FM broadcasts the transmitted information modulates the carrier therefore the modulating bandwidth is continuously changing and the system resolution is dependent on the instantaneous modulating bandwidth. It has been shown that large variations in resolution are observed during speech, especially during pauses but a relatively constant resolution is maintained during pop music [11].

It is valuable to examine the form of detection processing typically employed in PBR processing. Since the information transmitted is unknown, the reference signal has to be captured at the receiver directly from the transmitter. This means that the reference channel may contain target responses as well as multipath and other interfering signals. Care has to be taken to ensure that the reference signal is as pure as possible, otherwise ambiguities will occur as well as a general raising of the Amplitude Range Doppler (ARD) surface noise level. The signal from the target is captured by a second channel and this is cross-correlated as described previously with the reference signal. This two channel system is the simplest implementation of a PBR system and yields bistatic range and bistatic Doppler information for a target. Other approaches with increased system and processing complexity provide Angle-of-Arrival (AOA) information with an array based

receive antenna.

2.3 Literature Review

This section details the state of the art in terms of leading concepts, theories and experimental data relevant to this thesis. Published research involving airborne passive radar is limited however the techniques reviewed relating to airborne bistatic radar and ground based passive radar are relevant to the remainder of the thesis.

2.3.1 FM Ground Based Systems and Techniques

We start with a look at commercial FM as the illuminator and look at a simple yet remarkably effective system, the Manastash Ridge Radar (MRR) [12]. In 1997 at the University of Washington a team wished to examine the upper atmosphere using a radar system and designed a passive radar system using a commercial FM transmitter as the illuminator of opportunity. The FM signal has a good ambiguity response and a constant amplitude and therefore a high duty cycle. There is significant financial gain to not requiring a high power transmitter and associated licensing and health and safety costs. The physically separate transmitter and receiver also removes the need for complex receiver design, not needing to accommodate the collocated high power transmission with the highly sensitive receive path. The elegance of the system is the simplicity of its implementation. The DSI, is reduced to a very low level by siting the surveillance channel 100 km from the transmitter, on the opposite side of a mountain. The surveillance signal is obtained by having a surveillance antenna near the transmit site to record a near perfect copy of the transmitted signal. The receiver system is based on a direct conversion mixer with the sampling and mixing frequencies derived from a Global Positioning System (GPS) disciplined oscillator. A microwave link allows the digitised data to be transferred in a timely manner to a central hub for processing.

In 2002, Zoeller et al. [13] developed a two channel FM PBR system capable of detecting commercial aircraft out to 100 km. Unlike the MRR system, DSI reduction is at the heart of Zoeller's system. By using a high gain reference antenna, a largely uncorrupted reference signal is obtained. Orienting the surveillance channel antenna so that the transmitter is in a null and the main lobe is in the direction of expected target returns, is a first stage of DSI suppression. This was found not to give enough suppression and therefore an RF canceller was implemented prior to downconversion. This consisted of coupling the signal

from the reference channel, manually adjusting the amplitude and phase and summing in anti-phase with the surveillance channel signal. This is reported to have yielded 20 dB of cancellation of the transmitted signal in the surveillance channel. Once the signal was digitised, the zero-Doppler component was cancelled digitally to prevent the multipath sidelobes masking potential targets. As in the MRR case, the output of the system was an ARD surface showing the matched filter output as a function of bistatic range and bistatic Doppler. No tracking or further processing was implemented.

A system developed at the NATO C3 Agency in the Netherlands, by Paul Howland in 2005, comprises a two channel interferometer for target signals and a single channel reference antenna. The antennas are vertically polarised half-wave dipoles, mounted in front of a wire mesh screen, this combined with orienting the surveillance antennas with a null in the direction of the transmitter, helps to reduce the direct signal interference in the surveillance channel. To remove the degrading effect of the direct signal and stationary clutter, the surveillance channels are filtered prior to cross-correlation processing. The filtering is implemented through the joint process estimator algorithm, in two parts. The first part is a 50 stage lattice predictor, using the input signal to compute the uncorrelated, orthogonal backward prediction errors. These backward prediction errors are then used in an FIR filter to estimate the desired signal. Howland claims that the adaptive filter can suppress interference by almost 75 dB, however it is more likely that all the direct signal reduction methods contribute to this. Howland also suggests an efficient implementation of a cross-correlation routine [14] that uses decimation techniques to discard Doppler frequencies that do not exist thus considerably reducing the processing load. A standard CA-CFAR processor then identifies potential targets. Once identified, a phase comparison is made between the detections on the two surveillance antennas to gain some direction of arrival information. This is used in a Kalman filter for internal tracking in the system. This system represents quite an achievement in ground-based FM PBR with demonstrated tracking of targets out to 150 km and operating in real time.

In 2006, O'Hagan et al. at University College London, developed a PBR demonstrator system which although of a simple design, highlighted a number of important practical implementation issues. The receiver consists of amplification, filtering and a high-performance undersampling ADC. This approach ensures that the coherency is maintained between the channels and has demonstrated target detections at distances in excess of 90 km. An analysis of the of the signal levels for the scenario shows that suppression of the order of 63 dB

[15] level as the system noise floor. Also at UCL it has been shown that when operating in an urban environment, RF interference raises the effective noise figure of the system to around 25 dB [16]. In a similar way to the MRR, DSI is suppressed by placing the reference and surveillance channels are placed either side of a tall building. This alone is reported to introduce 10-15 dB of suppression. The remainder of the DSI is removed digitally through the implementation of a Least Squares adaptive cancellation algorithm termed the Extensive Cancellation Algorithm (ECA) [17], typically achieving 30 to 40 dB of direct signal suppression. Adaptive filters in general rely on having a perfect replica of the transmitted signal in order to perform the matched filtering with theoretical results indicating in excess of 50 dB Clutter Attenuation (CA). In reality, the reference signal will contain multipath and hence the reduction in measured CA. A method for the equalisation of the reference channel has been suggested by Cardinali et al. based on a constant modulus algorithm [18] however this is not implemented in the UCL system.

At the University of Cape Town, Heunis et al have developed a prototype FM PBR system based on the Universal Software Radio Peripheral (USRP) hardware platform and the opensource GNURadio software-defined radio (SDR) toolkit [19]. This approach makes the receiver system very flexible since the ADC is capable of digitising 50 to 860 MHz and has an on board FPGA which is used for the initial down conversion and low-pass filtering. A second downconversion and downsampling stage is implemented on the PC. A digital adaptive filter gave a 27 dB suppression in the direct signal and clutter levels in the range-Doppler surface.

The performance of a PBR is time varying due to the variation in instantaneous modulating bandwidth of the transmitted signal and the variation in propagation channel characteristics. Typically FM transmitters transmit multiple stations on different carrier frequencies in the 88 to 108 MHz FM band. These different channels can be exploited in an attempt to use the frequency diversity to overcome the time varying detection performance of passive systems. Bongioanni et al. at the University of Rome "La Sapienza" applied a multi-frequency approach which yielded an improved performance relative to the single channel case [20]. Having channel diversity means that on a scan-by-scan basis, the channel with the most favourable ambiguity function, in terms of resolution and sidelobe levels, and favourable propagation channel can be used for the target detection. The approach suggested by Bongioanni et al. is to incoherently sum the range-Doppler surfaces for each channel, after scaling and frequency compensation, with the demonstrated results showing

a vast detection improvement over the single channel case.

As shown in Equation 2.8, bistatic radar range resolution is dependent both on the target location with respect to the transmitter and receiver and on the modulation bandwidth of the transmitted signal. Compared to the digital modulation schemes discussed in the next section, single channel FM has a poor modulation bandwidth, typically of the order or 20 kHz for rock music content [21]. Olsen et al [22] proposed a method for improving the range resolution of the system by exploiting multiple adjacent channels from the same transmitter. Their suggested approach takes account of the different target Doppler shifts experienced for each frequency channels and the lack of phase synchronicity between channels [23]. In [24] this algorithm is extended to allow the fusing of DVB-T as well as FM signals and implemented on simulated data.

2.3.2 Digital Based Systems

The increased bandwidth and resolution of digital waveforms has spawned interest in using DAB and DVB-T signals as illuminators of opportunity. In 2006 BAE Systems developed a wideband PBR demonstrator to take advantage of DAB and DVB-T signals [25]. A four channel receive array allows digital beamforming to form a beam onto the transmitter for the reference signal. The channels were then processed to steer a null onto the transmitter to reduce the DSI in the surveillance channel, this was found to be an essential part of detecting weak signals. As for other systems, the cross-correlation is performed with a weighting to reduce the Doppler sidelobes. The wideband receive antennas were positioned to be 45° from vertical in order to be simultaneously sensitive to both vertical and horizontal polarisations. As expected receiver dynamic range was found to be a limiting factor in the sensitivity of the system and an analogue cancellation stage was found to be essential. In an enhanced version of the testbed, analogue cancellation was successfully implemented [26] although no figure for the amount of cancellation achieved is quoted. In the same way as Howland, decimation was used to ensure only Doppler frequencies of interest were calculated in the cross-correlation processing. This brought the system performance into near realtime processing made easier by the requirement not to digitally remove the zero-Doppler contributions with an adaptive filter. Presumably enough cancellation of DSI is achieved rendering adaptive cancellation unnecessary. The system was used to investigate passive target tracking using DAB. The received signal was not decoded and continued the input of many transmitters on the Single Frequency Network (SFN), leading to ghost

targets after processing. A major problem was found to be track initiation and a track initialisation algorithm was presented and found to be suitable for this application [27]. The Extended Kalman Filter was then used to track targets.

It was noted that system tracking performance could be improved through the use of the forming of narrow beams onto the relevant transmitter in order to ensure only the desired transmitter is providing the reference signal. At the University of Adelaide, Yardley and Coleman developed a DAB based PBR system [28] sited at the University of Bath. Again a four channel receiver was used with an undersampling digitiser. The direct signals were found to be around 100 dB above target returns and analogue nulling in the target directed antenna was found to be essential, although only 10 dB was achieved due to the broad bandwidth of the signal. In addition, the receive array was orientated cross-polar to the transmit polarisation. An interesting analysis is presented that shows the bistatic RCS for a small jet trainer was only a few dBs less than for the co-polar cross sections. The small reduction in bistatic RCS was found to be justified since the DSI fell by 18 dB [29]. The extraction of the pure transmitted signal from the reference channel was done using an FIR filter that removed multiple copies of the desired sequence. Initial results contained numerous false detections since the filter was not implemented however this demonstrated the need for the exact form of the illuminated signal to be estimated prior to matched filtering. Taking the approach that the spectrum of a DAB signal is essentially noise-like and that the reference signal would contain numerous delayed and complex weighted versions of the illuminating signal, Coleman proposed a standard filter for Auto-Regressive processes. The results are encouraging, showing attenuation of the interfering illumination signals from the other transmitters in the reference antenna beamwidth. The analogue null placement and cross-polar receive array was found to be sufficient to bring the dynamic range of the DSI into line with the ADC however high levels of DSI and associated multipath remained, masking smaller targets. This resulted in the use of digital DSI cancellation post ADC. Targets have been detected at bistatic ranges in excess of 60 km and the response is found to drastically vary between detections, probably due to the variation in bistatic RCS. For an airborne system where both the target and receiver are in motion, the variation in RCS could lead to missed detections which could cause tracking issues. Knowledge of likely target trajectories could allow the receiver flightpath to be optimised to reduce missed detections.

In the same manner as for FM, making use of different DAB channels from the trans-

mitter gives rise to a more robust detection ability and, when fused together, an improved resolution over a single channel. Berizzi et al at the University Pisa have used a USRP based system and UMTS and DVB-T signals to form a multi-band demonstrator system [30] and demonstrated detection of moving vehicles on a road using both illuminators. This work was extended to fuse three adjacent DVB-T channels for improved target resolution [31] from 57m for a single channel to 18m for all three channels. The work is supported by successful detections of commercial aircraft and is the first step to performing passive imaging and target classification.

2.3.3 Airborne Bistatic Systems and Techniques

In 1937 the first UK experiment with airborne bistatic radar was a system called RDF1.5 [4] with a ground based transmitter, located at Bawdsey Manor transmitting 3 μs pulses at 6.8 m and at 40 kW peak power. The receiver was placed on the interception aircraft, a Heyford bomber, which circled at a few thousand feet. Impressively the system picked up aircraft at ranges of 8 to 10 miles.

In 1980, the Sanctuary programme [32], protected its receiver sites by using an airborne transmitter at L-band. The airborne transmitter illuminated a large volume and ground-based receiver sites were optimised for the detection of low-flying airborne targets in severe clutter conditions. For a typical scenario, the clutter velocity was found to vary over its range by up to one-third of the platform velocity. A sidelobe canceller was implemented at IF in the receiver, specified to give 20-25 dB in suppression of the direct signal [33]. The receiver electronically steered array allowed the beam to be scanned $\pm$ 45° in azimuth with sum and difference beams [34].

There has been considerable theoretical interest in Bistatic Space-Time Adaptive Processing (STAP), for clutter suppression, typically using an airborne transmitter and receiver, a phased array antenna system and pulse-Doppler processing. STAP in monostatic airborne radar has been widely discussed [35, 36] and is based on the implementation of a 2D space-time filter to the received signals to increase the probability of detection of slow moving targets that fall within the system clutter bandwidth. Several works have theoretically investigated the application of STAP to a bistatic geometry [37, 38, 39, 40, 41]. The nonstationary part of the clutter degrades the STAP detection performance and the implementation of a reduced-dimension STAP with time-varying weights improves performance [42].

Bistatic airborne SAR has received a lot of interest over the years and been the subject of many experiments for clutter reduction in foliage penetration target detection. The Swedish defence research agency, FOI, has been active in the area of airborne bistatic VHF SAR and has two airborne systems: CARABAS-II, operating at 20 to 90 MHZ, and LORA, operating at 200 to 800 MHz [43]. For the experiment, CARABAS-II was used as a monotstatic airborne radar and LORA was set up as a ground based receiver. The two systems were synchronised using a GPS disciplined 10 MHz oscillator. Several experiments using this set up were completed [44, 45, 46]. It was found that the bistatic geometry gave an improvement in signal to clutter ratio of the order of 6 dB on under foliage targets for relatively small bistatic angles [47] .

2.3.4   Airborne Passive Radar Research

The limited published literature in this area mainly concerns airborne passive radar designed for air target detection. To aid in the detection of low Doppler targets and ground moving target, a robust clutter suppression approach is required and therefore methods of clutter suppression are popular research topics.

In 2006 Chao et al. [48] proposed an airborne PBR receiver using an FM broadcast transmitter for Airborne Early Warning (AEW) applications. An analysis of the SIR for the scenario was performed. The analysis assumed that the transmit antenna comprised an array, with a beampattern optimised for ground FM coverage and designed to reduce power leakage into the sky. This approach predicted an SIR in the range of -60 to -110 dB for reasonable values of bistatic RCS and target height. The analysis was for a static scenario and made no attempt to examine the signal-to-clutter ratio for the scenario.

A similar conclusion was reached by [49], on the assumption that adequate direct signal suppression is used. They go on to simulate the power-budget and the power spectrum and eigenspectrum of the interference scenario [50]. Undersirable random range sidelobe coupling of the direct path and strong clutter signals can be countered by more degrees of freedom for effective interference rejection. Additionally using directional high gain antennas, direct path clutter cancellation and an increased time-bandwidth product.

At the Warsaw University of Technology, Kulpa has developed an airborne PBR testbed, PAssive RAdar DEmonstrator (PARADE) [51], which uses FM as an illuminator of opportunity. This system has proved flexible and is based on digitising the signals as early as possible and performing filtering and downconversion digitally. The system has an 8 ele-

ment circular array antenna and beamforming is implemented digitally [52] to obtain the reference and surveillance beams. The DSI and stationary clutter contributions are filtered out using a similar adaptive filter to Howland's lattice predictor and tapped delay line. The cross-correlation is computed at the delays and Dopplers of interest and passed to a CA-CFAR algorithm. A 6 element version of the PARADE system was placed on the roof of a car [53] and Space-Time Adaptive Processing (STAP) was used to mitigate the Doppler-spread of ground clutter. The Doppler bandwidth of the clutter was wider when the receiver's antenna was looking perpendicular to the direction of motion, as expected. This system has yielded detections but is still in the early stages of development. This system has also been used in airborne trials on board a twin engine Skytruck [54, 55]. The system was installed on board the aircraft with the antennas taped to the inside of the passenger windows, under the wings. Although no definitive detections are reported, it was found that multipath interference was significantly weaker than for the car implementation.

The behaviour of the clutter for a moving transmit or receive platform is a performance limiting issue in PBR performance since slow moving and low flying targets could potentially be masked by the Doppler spread of the clutter. Moving Target Indication (MTI) techniques for clutter suppression such as DPCA and STAP are generally established methods of clutter suppression for monostatic airborne radar however the geometrical impact of the passive bistatic scenario adds another layer of complexity to the processing. The clutter mitigation problem has been approached from two directions. The Displaced Phase Centre Antenna (DPCA) technique is discussed in [56] and in [57] the technique is applied to the data collected using the previously discussed Warsaw University of Technology airborne system. The DPCA technique is found to suppress the clutter returns by 30 dB. Another approach is the Amplitude and Phase EStimation (APES) technique as explained by [58] it was used to reject ground clutter on simulated DVB-T data.

2.3.5 Literature Review Summary

There are several valuable points to be drawn about PBR from the literature review.

- DSI reduction before digitisation reduces the amount of processor intensive digtital adaptive filtering required and also increases the interference limited detection range of the system. The simpler systems of O'Hagan and Sahr have successfully used physical separation and shielding to reduce DSI. Equally orienting the surveillance antenna cross-polar to the transmitter, is a simple yet effective method of reducing

the DSI and as Coleman has shown, attracts only a small penalty in SNR for a large gain in SIR. Equally, analogue cancellation through amplitude and phase adjustments between array elements is a useful method of gaining typically 10-20 dB of cancellation. Adaptive filtering of the surveillance channel is necessary to ensure that the DSI sidelobes are not masking weak targets.

- Directly digitising the signal is the favoured approach. This mitigates any system errors in multi-channel systems due to the variability of passive components and maintains the coherency of the channels

- For the reliable operation of ground based systems, an understanding of the impact of receiver siting on the system performance is crucial. Simulation of the system performance would allow site selection. The simulation can then be verified and validated with site measurements as in reality, site access may not be possible. For an airborne system on an operational mission, this simulation would create a "smart map" which would define an envelope of operation within which the passive sensor would work as required.

- The use of a multiple element receive array allows flexibility in choice of transmitter and the adaptive introduction of nulls in the direction of interfering signals.

- Bistatic STAP techniques for clutter suppression have been theoretically devised and are typically based on an extension of established monostatic SAR theory, however their application is currently confined to simulated data. A DPCA technique for clutter suppression has been applied to real data using an airborne FM system and found to give 30 dB of clutter suppression. This requires the two antennas to be sited next to each other parallel to the direction of flight. Cooperative bistatic imaging using an airborne SAR receiver has been demonstrated at VHF frequencies but not in a passive implementation.

- For airborne PBR, DSI reduction will need to be addressed in order to operate in a noise-limited detection mode. Using highly directive antennas or physical shielding will not be appropriate on a small airborne platform therefore an analogue canceller may be required in order to suppress the DSI. This approach has been shown to give in excess of 20 dB of cancellation for a ground based, static system. For an airborne system where the receiver and target are in motion, the analogue canceller will need

to adaptively control the direction of the null to ensure good suppression. A robust simulation will determine the necessity of a canceller.

- The greater the number of elements in the receive array, the more flexibility in the beampattern for nulling interference or beamforming on to targets. A UAV or small aircraft will have limited fuselage available for antennas, especially if operating at VHF. Therefore a demonstrator using this type of platform will be limited in the number of elements that can be used.

- It is interesting to note that the target RCS has been found to vary from capture to capture for a ground based system. Equally it has been shown that the cross-polar and co-polar responses of a small aircraft are theoretically very close. It is easy to imagine the RCS variation when comparing a head on and broadside aircraft aspect. To maximise the probability of detection of any experimental data collection this suggests that careful receiver flightpath planning will be required. The trajectory of the receiver can be chosen to maximise the persistence in RCS for a given target flightpath and this will require reliable scenario modelling. Equally, the variation in RCS would lead to dropped detections, this could lead to tracking issues. Again judicious flightpath selection could help to minimise the impact of this.

- Making use of different channels from the same point would give more robust target detection and if adjacent channels can be digitised, resolution improvement techniques can be employed. With a moving receiver, the ability to switch between channels and transmitters will be important in order to reduce the impact of multipath nulls.

2.4 Summary

The crucial design equations for PBR systems have been presented along with an explanation of the various factors that need to be considered in the design stage. A brief analysis of the signals available for exploitation as illuminators of opportunity has shown that digital signals such as DAB offer superior performance in terms of resolution and ambiguity. This is at the expense of reduced coverage and availability compared to higher power FM transmissions. The literature review has shown that in practical systems, the quality of the reference signal affects the output SNR of the radar processor and that for DAB systems in particular an extra layer of processing is required to remove the contribution from single frequency networks. FM transmissions have a time-varying bandwidth and therefore

a time-varying range resolution. However, if a multi-frequency receiver is used, the illuminating signal can be dynamically chosen to ensure the system is using the best illuminator for the given propagation and modulation conditions.

A review of the pertinent literature has shown that analogue cancellation methods aid in the successful operation of PBR systems and that digital filtering is fundamental to the mitigation of DSI in the surveillance channel. The DSI environment for an airborne platform is unknown however an analogue canceller, to null the DSI in the surveillance channel, may be required. Ground based work with a static receiver, has shown a drastic variation in target RCS from capture to capture. This could potentially be minimised with a reliable modelling environment however the impact on tracking is unknown. In order to quantify the performance that might be expected for a given system, a reliable simulator is required in order to correctly design a demonstrator system.

Very little work has been reported concerning practical airborne passive radar research, making this a fertile area for new and challenging research.

Chapter 3

Airborne PBR Simulation

3.1 Introduction

The performance of ground based PBR systems is typically estimated through the application of the bistatic radar equation to the geometry. The approach taken in this work goes beyond application of the classical bistatic radar equation and looks to examine the dynamic effects associated with a moving receiver platform. By constructing a realistic and reliable simulation based on conservative estimates of system and target metrics, it is possible to obtain an indication of the likely success of an airborne trials campaign. Following on from this, if the simulation indicates that a reasonable system performance could be obtained, this can then also be used as an aid to designing a favourable experimental scenario in which the system would be likely to detect aircraft. This insight into the system performance can feed into the physical hardware design, receiver flight path planning and offline signal processing for the real demonstrator system.

3.1.1 Simulation Methodology

The aim of the simulation was to demonstrate that a physically realisable system would be able to detect airborne targets and capture ground clutter data based on realistic estimates of realisable system parameters. In order to detect an air target using an airborne passive bistatic radar, there are four key phenomena that need to be understood and these are the focus of the following analysis. Firstly, the target must be within the transmitter and receiver line-of-sight (LoS). Secondly, the target return must be detectable against the dominant receiver noise mechanism. Thirdly, the direct signal from the transmitter must not saturate the receiver's Analogue-to-Digital Converter (ADC). Finally, the target return

must be detectable against the clutter returns. These issues are discussed in the following sections of this chapter.

At the proof of concept stage, the parameters and values used were system parameters for a proposed dual channel PBR system to be used in flight experiments conducted in the south of England. The transmitter was assumed to be the Wrotham BBC FM transmitter in Kent, the receiver platform was a light aircraft and the parameters listed in Table 3.1 are assumed for the installed receiver system, transmitter and target.

It is conventional to measure airspeed in knots, distances in nautical miles and location in latitude and longitude; in this work SI units [59] will be used throughout with the corresponding conventional units in brackets where appropriate. All mapping is in OSGB36 Easting/Northings coordinates unless otherwise stated and altitude will be stated in metres not feet.

3.2 Line of Sight Limited Coverage

The matched filtering operation, described by Equation 2.23, requires a copy of the transmitted signal, which is obtained by sampling the direct signal from the transmitter. At VHF frequencies, the receiver needs to be within Line-of-Sight (LoS) of the transmitter. Equally, in order for the target to be detected, the target needs to have LoS to both the transmitter and receiver. This introduces a fundamental limitation on the deployment of an airborne passive radar system.

Using a 4/3 earth approximation and assuming a smooth earth [4], the LoS limited detection radius for the transmitter, r_T, and the receiver, r_R, in kilometres, can be approximated as Equations 3.1 and 3.2.

$$r_T = 130 \left(\sqrt{\frac{z}{1000}} + \sqrt{\frac{z_T}{1000}} \right) \tag{3.1}$$

$$r_R = 130 \left(\sqrt{\frac{z}{1000}} + \sqrt{\frac{z_R}{1000}} \right) \tag{3.2}$$

Where z, z_R and z_T are the heights of the target, receiver and transmitter above sea level in metres, respectively. The radii form circles centred on the transmitter and receiver and targets present in the overlapping circles have LoS to the transmitter and receiver.

Table 3.1: Transmitter, receiver, target and clutter parameters for modelling and simulation work

	Parameter	Symbol	Value
Transmitter	Transmitter Location		TQ595604
	Polarisation		Mixed
	ERP H Polarisation		125 kW
	ERP V Polarisation		125 kW
	Effective Modulation Bandwidth	B	20 kHz
	Centre Wavelength	λ	3 m
	Antenna Height Above Ground Level	z_T	150 m
	Antenna Height Above Sea Level		370 m
Receiver	Receiver Antenna Gain	G_R	-10 dBi
	Effective Noise Figure	F	25 dB
	Integration Time	t_{int}	1 s
	Processing Gain	G_P	53 dB
	Receiver Dynamic Range	DR	75 dB
	Baseline	L	$0 \le L \le 100km$
	Altitude Above Sea Level	z_R	$200 \le z_R \le 2000m$
	Ground Speed	v	$40 \le v \le 60ms^{-1}$
Target	Bistatic RCS	σ_B	20 dBm^2
	Altitude	z	$0 \le z \le 10km$
	Air Target Ground Speed	v	$30 \le v \le 340ms^{-1}$ (Mach 1)
Clutter	Ground Target Speed	v	$0 \le v \le 90ms^{-1}$
	Normalised Clutter Cross-Section	σ_C^0	-30 dB
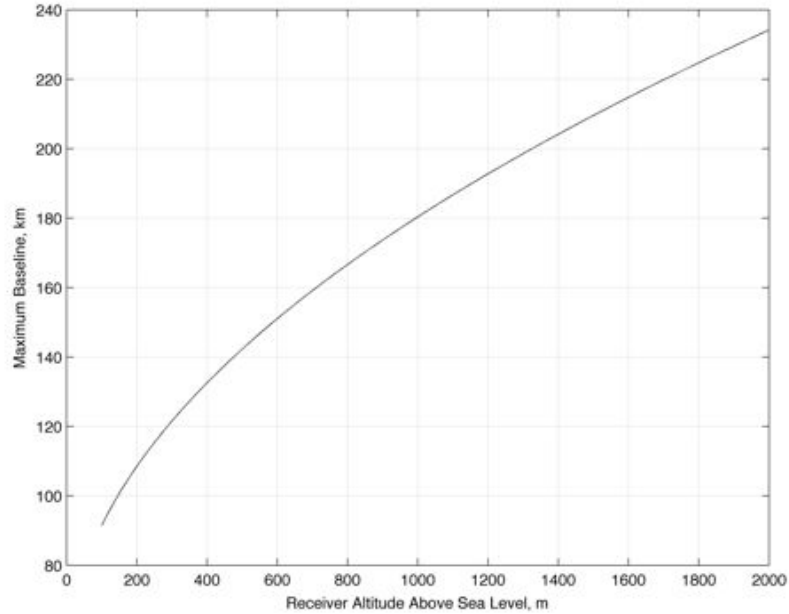
Figure 3.1: Maximum baseline variation with receiver height for a fixed transmitter height. Calculated using the 4/3 earth approximation and assuming a smooth earth.

In order to ensure that the receiver has LoS to the transmitter, the baseline must be chosen so that for a given altitude, LoS to the transmitter is maintained as described by the inequality of Equation 3.3.

$$L \leq 130 \left(\sqrt{\frac{z_R}{1000}} + \sqrt{\frac{z_T}{1000}} \right) \tag{3.3}$$

Since the antenna is approximately 370 m above sea level and the receiver is assumed to be at a height of $100 \leq z_R \leq 2000m$, the height dependent LoS limit on the baseline, is shown in Figure 3.1.

This simplified approximation suggests that provided the air platform stays above 400 m Above Sea Level (ASL) , the receiver will have the required LoS to the transmitter. Referring to Equations 3.1 and 3.2, for a fixed transmitter and receiver height, the lower the target altitude, the smaller the common coverage area formed as the intersection of the two LoS radii from the transmitter and receiver. The coverage volume will decrease as the receiver altitude decreases, therefore if ground coverage is required for low-flying aircraft for imaging, the LoS to the target and receiver will need to be taken into account. In the example in Figure 3.2, the receiver is at an altitude of 500 m and the common coverage area for a target at 0 m is shown as the common coverage area.
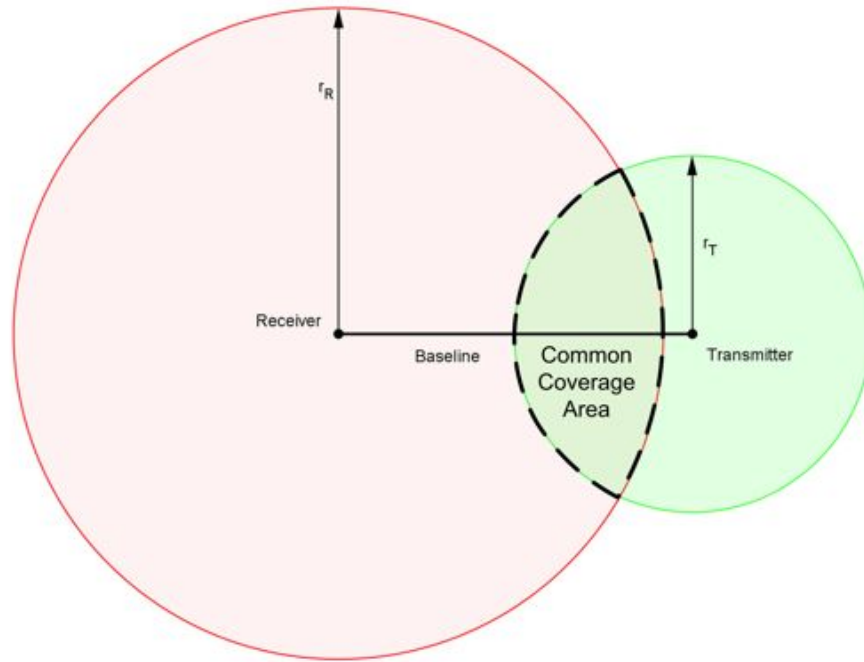
Figure 3.2: Common coverage area for the receiver at a range of 100 km from the transmitter and an altitude of 500 m. The transmitter is at 150 m and the target at 0 m.

3.3 Sensitivity

The target return must be significantly greater than the receiver thermal noise for reliable detection. One of the benefits of passive radar is the long integration times that can be employed, meaning a reduced noise bandwidth. For a 1 second coherent processing interval, the target return has to compete with the thermal noise in a 1 Hz bandwidth.

The power of the direct signal at the receiver is many orders of magnitude greater than the power reflected from the target. The receiver must have the Dynamic Range (DR) to sense both the high power DSI and the very low power target return signal. The Signal-to-Interference Ratio (SIR) quantifies the system's ability to handle the signals and this is investigated here.

The calculation of target SNR and SIR is dependent upon the transmitter radiation pattern and the multipath contribution on the transmitter-to-target and target-to-receiver path. This section describes the approaches to modelling the antenna pattern and the multipath interaction. The results are then used to examine the likely radar performance for a given scenario.

Transmitter Radiation Pattern

The FM transmitter radiation pattern is typically well defined in azimuth as it determines the terrestrial coverage for radio receivers. The elevation radiation pattern is not well documented. In order to detect air targets, the transmitter must illuminate the airspace above it therefore it is essential that there is a significant proportion of the radiated power being radiated above the horizon.

The radiation pattern for a commercially available FM transmitter array is tailored to ensure that the ground coverage is maximised and that power is not wasted above the horizon. This can be approximated as omni-directional in azimuth with a directive elevation pattern. Assuming the antenna is constructed from N half-wave dipoles in a collinear stack with the main lobe deflected by δ away from broadside, the radiation pattern can be described by Equation 3.4[60]. The elevation angle, ϕ, is measured from 0° at the horizontal to 90°, vertically upwards.

$$f_t(\phi) = \frac{\sin(\frac{\pi}{2}\sin\phi)}{\cos\phi} \frac{\sin\frac{N\psi}{2}}{N\sin\frac{\psi}{2}} \tag{3.4}$$

Where

$$\psi = \frac{2\pi d}{\lambda}\left(\sin\phi - \cos\delta\right) \tag{3.5}$$

Where d is the distance between the phase centres of the dipoles. The radiation pattern is taken to be Equation 3.6.

$$G_t(\phi) = |f_t(\phi)|^2 \tag{3.6}$$

A high power main transmitter may have up to 8 elements in the array, whilst a lower power gap-filler may have 3-4 elements. In both circumstances the mainlobe in elevation is angled at broadside.

For this simulation, the FM antenna specification and beam pattern are shown in Table 3.2 and Figure 3.3 [61]. The plot of Figure 3.3 shows that this antenna has a transmit

Table 3.2: Transmit antenna model parameters

Parameter	Symbol	Value
Number of elements	N	8
Lookdown angle	δ	0°
Element spacing	d	3 m
Centre wavelength	λ	3 m
Peak gain	G_{Tpeak}	12 dBi
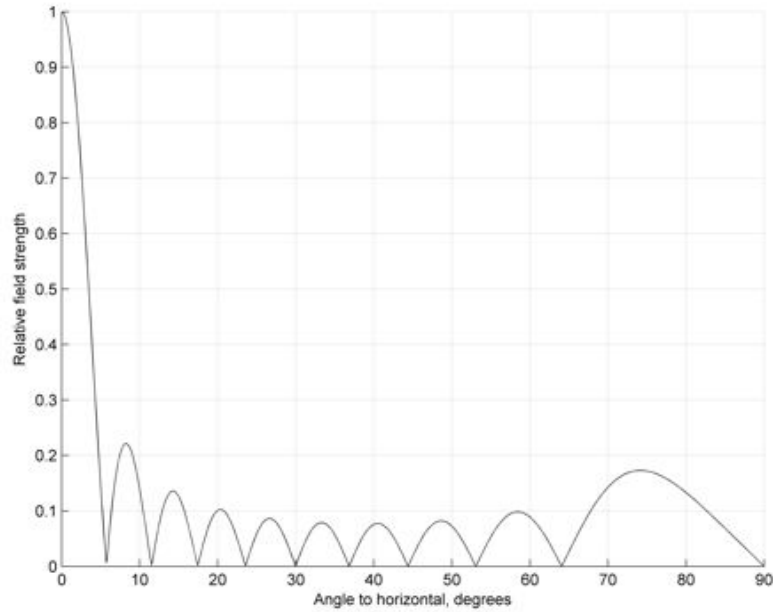
Figure 3.3: Vertical radiation pattern approximation to Wrotham FM transmitter.

beamwidth of 5° and a peak gain of 12 dBi.

Multipath

The transmitter and receiver will be operating at some altitude above the earth's surface. To begin to understand the impact of multipath on the system, it is useful to understand the effect of moving from a free-space scenario to one with a large flat conducting ground plane. The electrical property of a smooth, conducting ground plane can be expressed by a voltage reflection coefficient, ρ. For a perfectly conducting ground plane, $\rho = -1$. The effect can be simplified if it is viewed purely as a phase phenomenon where the differing path lengths between the direct and multipath modes equates to differing phases. At the receiver, the resultant phase is taken into account, this can vary from constructive summation to complete cancellation.

Referring to Figure 3.4, the indirect path length between transmitter and target, R'_T, is the path through a sidelobe of the transmit antenna to the ground plane. At a certain angle of incidence to the ground the transmit energy reflects onto the target. The equivalent paths from the target to the receive antenna is R'_R.
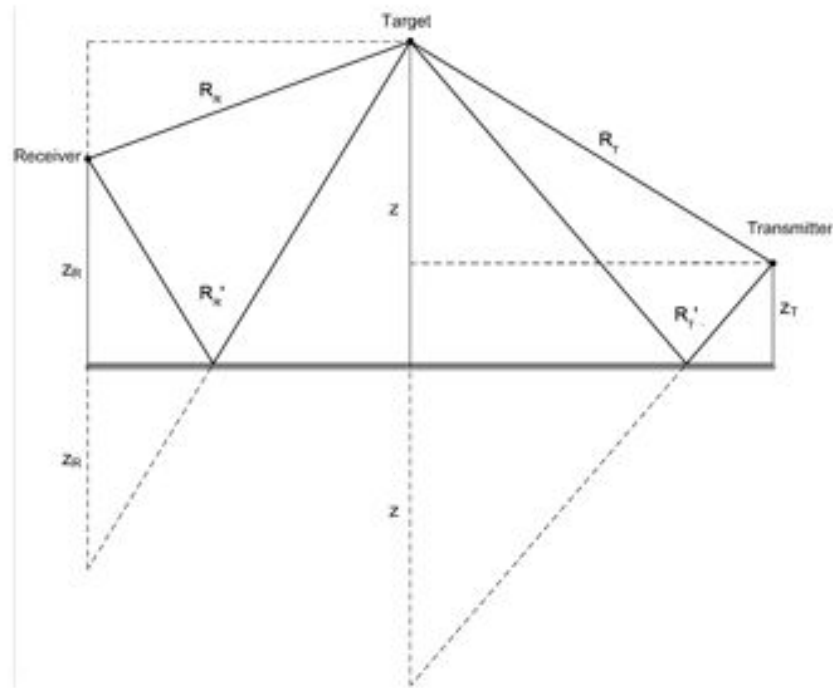
Figure 3.4: Multipath modes for a flat earth, airborne receiver and stationary transmitter. The dashed lines aid in calculation of the indirect path lengths

Four possible combinations of transmit-receive paths for the transmitted signal can now be defined:

$$1. \; D = R_T + R_R$$

$$2. \; I_1 = R_T + R'_R$$

$$3. \; I_2 = R'_T + R_R$$

$$4. \; I_3 = R'_T + R'_R$$

D, is the direct path and corresponds to the bistatic range. The extra distance travelled

by multipath modes relative to the direct modes, introduces a phase difference between the signals. An obvious conclusion to be drawn is that the use of directionality in the receive antennas, either through directive elements or an array approach, would reduce sidelobe emissions and therefore reduce the power of the interfering multipath modes. In this implementation this is not a realisable approach due to the limited space and system complexity. The pattern propagation factor, P_{pf}, models the effect of multipath between the transmitter, target and receiver. The effect can behave constructively to increase the power on target by up to 6 dB and also potentially completely cancel out the power on target. In this work the pattern propagation factor only takes into account the relative phases between the four available paths [62] between the transmitter, receiver and target and is expressed as (3.7).

$$P_{pf} = \left| 1 + \rho \frac{f_t f_r'}{F} e^{jk(I_1 - D)} + \rho \frac{f_t' f_r}{F} e^{jk(I_2 - D)} + \rho^2 \frac{f_t' f_r'}{F} e^{jk(I_3 - D)} \right|^2 \tag{3.7}$$

Where ρ is the surface voltage reflection coefficient, f_t and f_r are the transmitter and receiver voltage gain in the direction of the target respectively , f_t' and f_r' are the transmitter and receiver voltage gain in the direction of the multipath , $F = f_t f_r$ and $k = 2\pi/\lambda$. Since the relative difference in phases of the four modes is of interest, the first term of Equation 3.7 is unity representing the phase of the direct path, D. The second term is for path I_1 which involves a single multipath bounce, similar to the third term for I_2. The final term contains a ρ^2 since this mode has two reflections.

3.3.1 Simulation Process

In order to implement a flexible simulation process, the following procedure for analysis of the SNR and SIR was employed. This structured approach allowed for physical effects to be included as required.

For a static receiver and transmitter, the sensitivity varies in the three spatial dimensions. The method used for calculating the sensitivity for a given geometry is:

1. **Define transmitter location** The receiver centred coordinate system allowed sensitivity comparisons between differing geometries without a coordinate system translation

2. **Define solution space** This scalable approach allowed the solution to be calculated for a single three dimensional point, a two dimensional slice through the transmitter

and receiver plane, or for a three dimensional x-y-z volume. Equally, a target aircraft route could be specified and the system sensitivity estimated for the duration of the target flight

3. **Constants calculation** System constants that do not depend on the receiver, target or transmitter location are then calculated. For example, receiver thermal noise floor and baseline.

4. **For each point in the solution space** The routine assumes that a target of a specified bistatic RCS is placed at every point in the solution space:

   - **Geometry analysis** The transmitter and receiver path lengths and incident angles for the specific point are then calculated

   - **Transmitter radiation pattern** The incidence angles are then used to calculate the transmitter radiation pattern for the direct path and the multipath modes, using Equation 3.6

   - **Multipath analysis** The multipath analysis detailed in Section 3.3 is calculated using Equation 3.7

   - **Free space SNR** The free space SNR for the target based is calculated using the bistatic radar equation as shown in Equation 2.17

   - **Free space SIR** The free space SIR for the target and transmitter is calculated using Equation 2.20

   - **Clutter Doppler response** The clutter Doppler response is calculated using the approach outlined in Section 3.4.1

5. **Plotting options** The output is plotted either as a sensitivity of Doppler surface or as a line plot, dependent on the plotting requirements. Contours of constant SNR, SIR or Doppler are added as appropriate.

This approach was efficiently implemented in Matlab in order to provide a fast simulation time. This processing flow has been used for the production of the following SNR and SIR estimates and figures.

3.3.2 Signal-to-Noise Ratio

The simplest way to visualise the noise limited performance of the system is to examine an elevation slice through the transmitter and receiver as the receiver moves from directly

above the transmitter out to the maximum baseline of interest at 100 km. With the receiver at an altitude of 1 km moving away from the transmitter, the SNR is plotted in Figure 3.5. The background intensity plot is calculated including the effect of multipath and the black line bounds the detection region for the 15 dB SNR contour. The 15 dB SNR contour is calculated without including the effect of multipath in order to give a clearer understanding of the general system performance. 15 dB was chosen as the minimum SNR in order to allow a conservative estimate of the coverage volume.
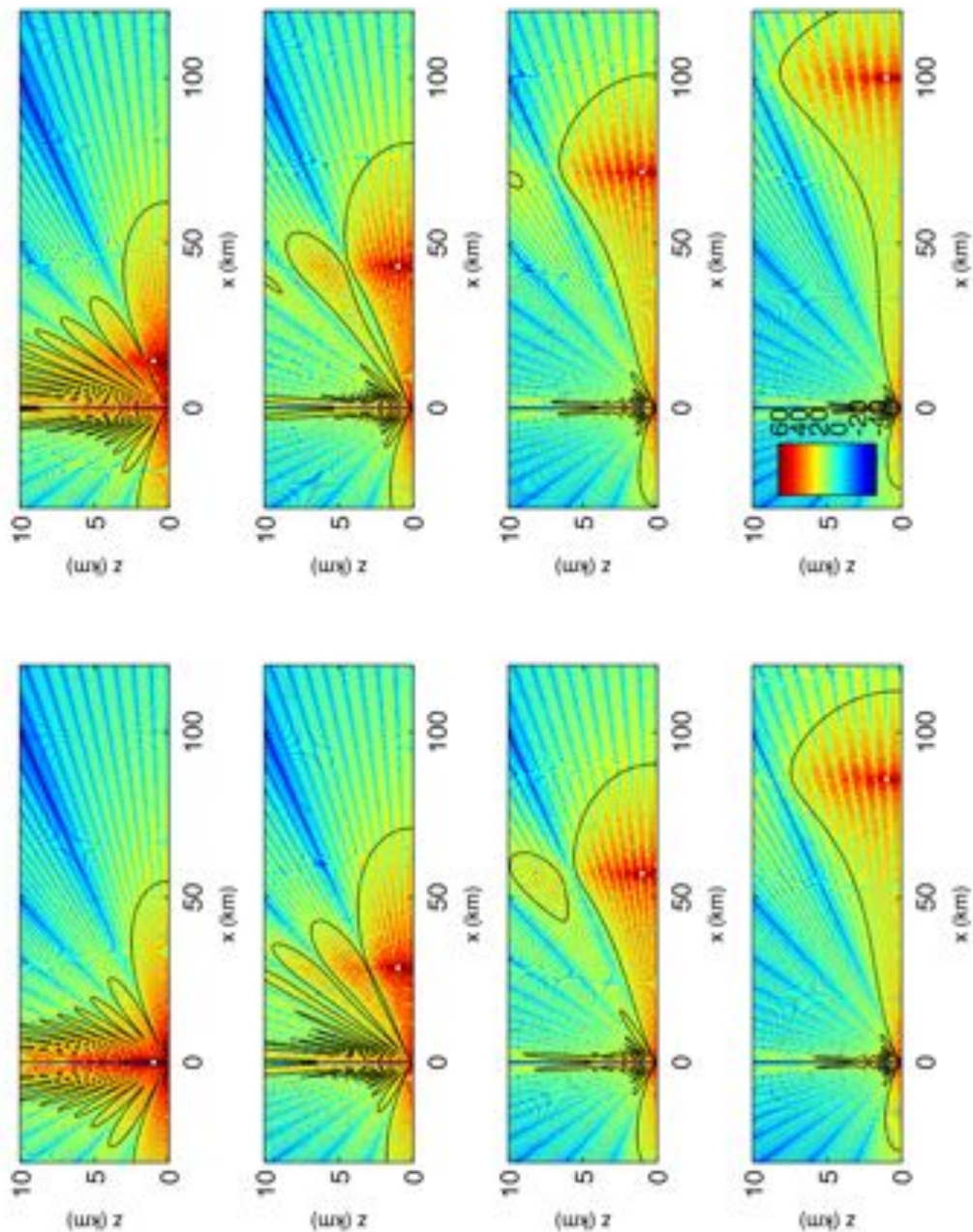
Figure 3.5: SNR for a receiver at an altitude of 1 km ASL moving away from the transmitter, out to 100 km. Receiver position indicated by a white dot. The background intensity image includes the effect of multipath whereas the black contour marks the 15 dB detection threshold, not including the multipath effect. In this model, the area within the black contour is the region where targets can be detected.

It can be seen from Figure 3.5 that with the system parameters listed in Table 3.1, that

a usable detection region is available in this geometry. For all the positions, it can be seen

that targets directly above and below the receiver are within the systems coverage. Also, along the baseline and in the vicinity of the transmitter there is low level coverage. This is an encouraging result since it suggests that for target detection against noise, there is a usable coverage area. Designing the experiment so that targets cross the baseline and fly close to the transmitter and receiver would maximise the probability of detecting the target.

3.3.3 Signal-to-Interference Ratio

For the same scenario as Section 3.3.2, the target signal to direct signal interference ratio is plotted in Figure 3.6. The background plot is the SIR including the effect of multipath and the black contour is the maximum detection contour for a minimum SIR of 75 dB. Compared to the SNR for the same scenario, it can be seen that the interference limited performance is degraded. The defining characteristic of the SIR limited detection contour is the low level coverage in the immediate vicinity of the transmitter and receiver and the coverage above the receiver. This result demonstrates that an airborne PBR system naturally offers a situational awareness capability in the immediate vicinity of the receiver and transmitter.

In order to increase the SIR limited detection volume, a stage of direct signal cancellation can be introduced, prior to digitisation, in order to increase the target SIR. This is demonstrated in Figure 3.7 where 10 dB of pre-ADC cancellation has been included. It can be seen that even with this relatively modest cancellation in the direct signal, the SIR limited coverage volume increases, approaching that of the SNR limited detection volume of Figure 3.6.

This study of the SIR limited detection volume suggests that the system detailed in Table 3.1 is capable of detecting targets in the immediate vicinity of the transmitter and receiver and with a modest amount of direct signal cancellation, capable of performing in a noise limited as opposed to interference limited mode of operation. Careful selection of the experimental flight path to ensure that targets are likely to fly close to the transmitter and receiver will ensure that the probability of detection of the target is maximised, even without any direct signal cancellation.
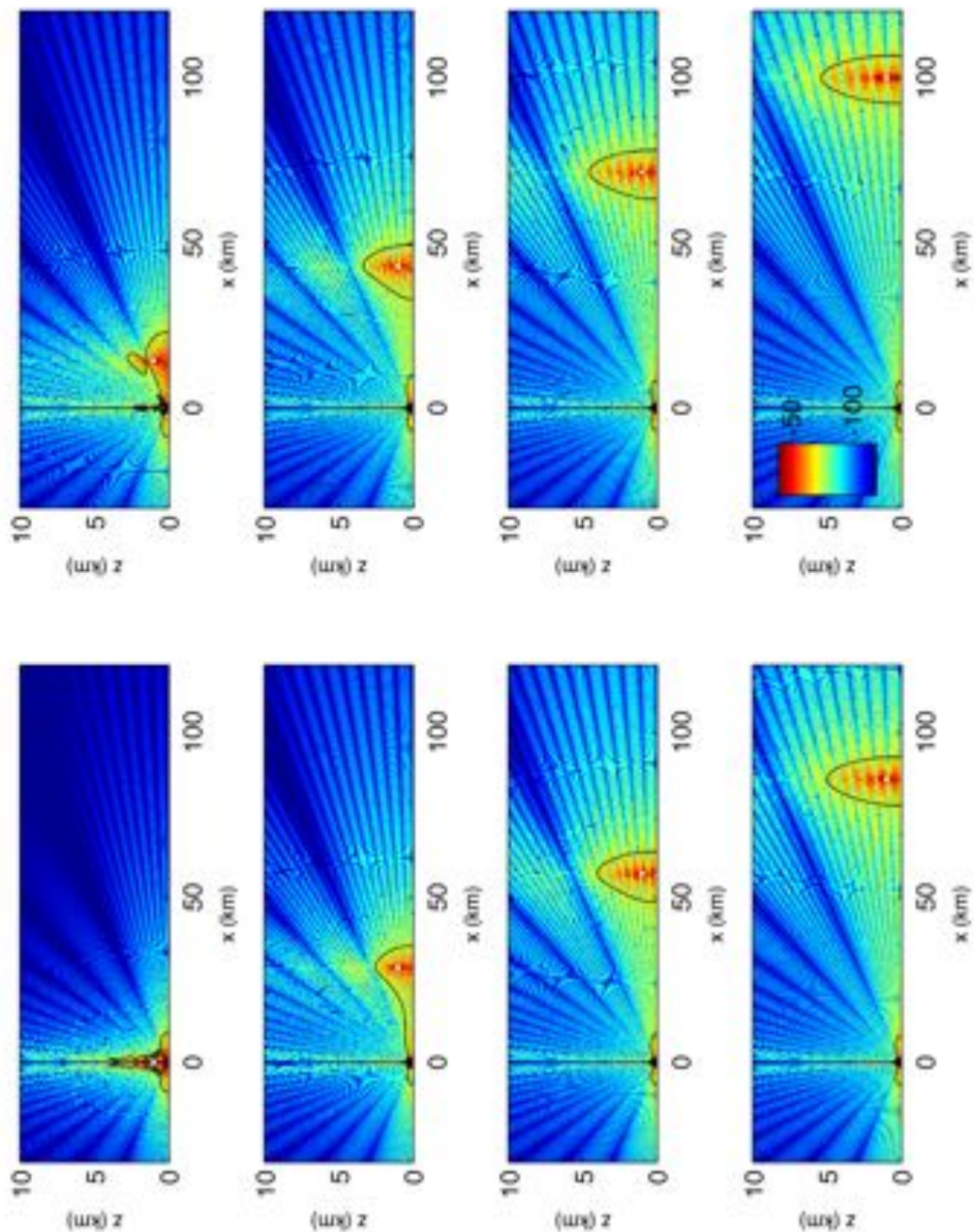
Figure 3.6: SIR for a receiver at an altitude of 1 km ASL moving away from the transmitter, out to 100 km. Receiver position indicated by a white dot. The background intensity image includes the effect of multipath whereas the black contour marks the 75 dB detection threshold, not including the multipath effect. In this model, area internal to the black contour is the region where targets can be detected
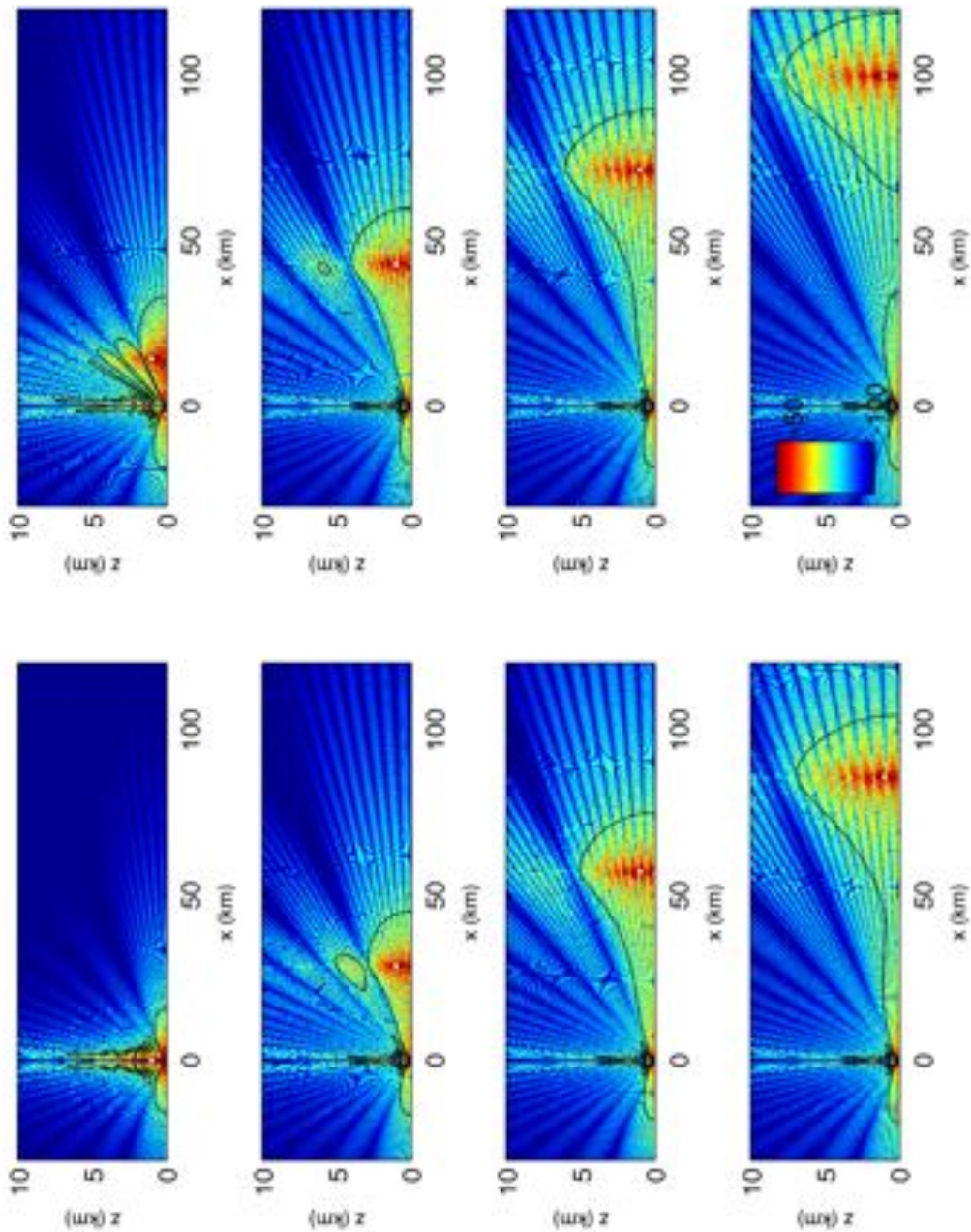
Figure 3.7: SIR for a receiver with 10 dB of direct signal cancellation at an altitude of 1 km ASL moving away from the transmitter, out to 100 km. Receiver position indicated by a white dot. The background intensity image includes the effect of multipath whereas the black contour marks the 75 dB detection threshold, not including the multipath effect. In this model, area internal to the black contour is the region where targets can be detected

3.4 Dynamic Receiver Effects

The sensitivity of the receiver against noise and direct signal has been analysed so far using the a static receiver assumption. In a static ground based system, stationary clutter will have a zero-Doppler shift and hence appear in the zero-Doppler bin out to the clutter horizon. Typically this means that the zero-Doppler bin out to the clutter horizon is digitally cancelled and, unavoidably, targets that fall in the zero-Doppler bin are cancelled too.

With a moving platform however, the stationary clutter has a relative Doppler shift due to the rate-of-change of the clutter to receiver path length owing to the receiver motion. The differences between the stationary clutter bandwidth and moving clutter bandwidth therefore need to be clearly understood. These issues are discussed in this section.

3.4.1 Clutter Doppler

In order to make the calculation of the clutter Doppler simpler, the schematic in Figure 3.8 is assumed.
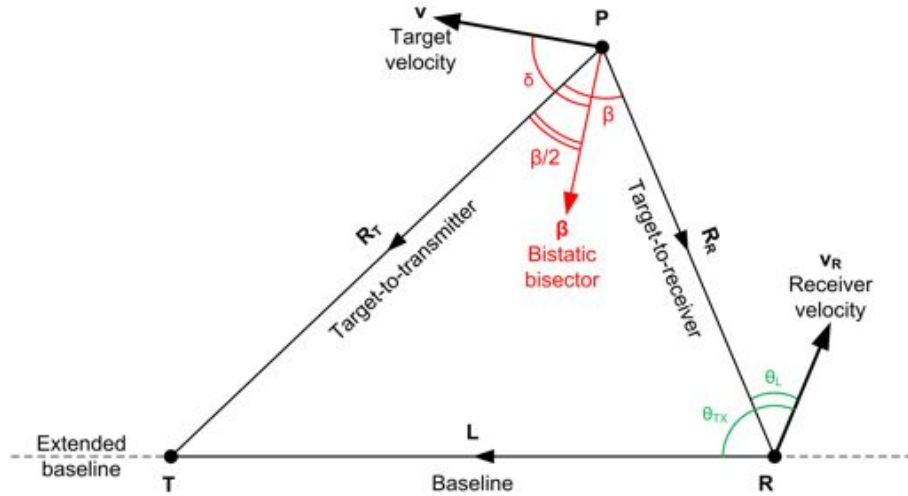
Figure 3.8: Schematic for clutter Doppler analysis

Using Equation 2.13 defined in Section 2.1.3, the clutter velocity is zero for stationary clutter therefore the relative bistatic Doppler shift is due purely to the receiver motion.

$$
\begin{aligned}
f_B' &= -\frac{1}{\lambda}\mathbf{v_R} \cdot \left(\frac{\mathbf{L}}{L} + \frac{\mathbf{R_R}}{R_R} \right) \\
&= -\frac{1}{\lambda}\mathbf{v_R} \cdot \left(\widehat{\mathbf{L}} + \widehat{\mathbf{R_R}} \right) \\
&= \frac{v_R}{\lambda} \left(\cos\theta_L - \cos\theta_{TX} \right)
\end{aligned}
\tag{3.8}
$$

Where $\widehat{\mathbf{L}}$ and $\widehat{\mathbf{R_R}}$ are unit vectors and θ_L and θ_{TX} are the angles as defined in Figure 3.8. For stationary clutter on the baseline, $\theta_L = \theta_{TX}$ therefore the relative bistatic Doppler shift is zero, irrespective of the receiver velocity. Also, for clutter in the direction of the receiver's velocity, $\theta_L = 0$ and hence for a given angle of transmitter, the clutter Doppler is maximised. While, for $\theta_L = \pi$ the minimum clutter Doppler is a minimum.

As discussed previously, the stationary clutter horizon exists out to the transmitter's radio LoS. For typical transmitter altitudes, the LoS extends over 200 km. Assuming that the receiver is operating inside this radius, the clutter will be visible at all antenna look angles.

The minimum and maximum extent of the stationary clutter Doppler, the Doppler bandwidth is described by Equation 3.9. As expected, the clutter Doppler bandwidth is directly proportional to the receiver speed.

$$\Delta f'_B = \frac{2v_R}{\lambda} \tag{3.9}$$

The variation in stationary clutter relative Doppler shift in the Cartesian plane is shown in Figure 3.9 using the process described in Section 3.3.1. where the axes have been normalised to the baseline length. The image confirms that the highest stationary clutter Doppler shift occurs in the direction of the receiver movement, the minimum Doppler shift occurs in the direction opposite to the direction of travel and clutter on the baseline has zero relative bistatic Doppler shift.
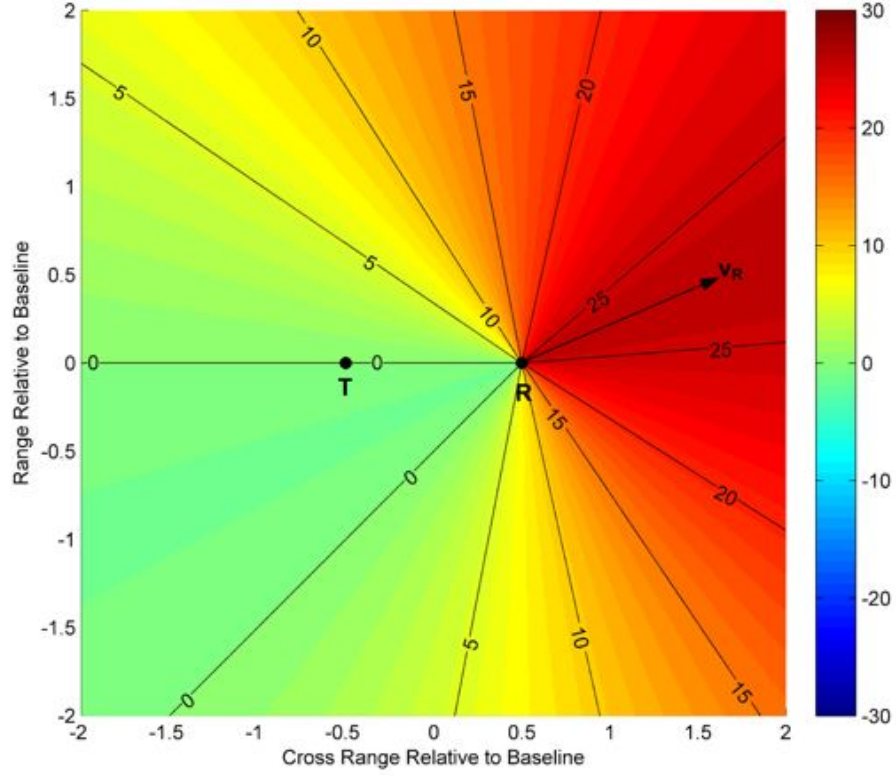
Figure 3.9: Bistatic Doppler scenario for stationary clutter. The transmitter is at [-0.5, 0] and receiver at [0.5 0] travelling at 40 ms^{-1}. The colour scale is in Hz.

The relative bistatic Doppler shift of a moving target is developed in a similar manner to the stationary clutter scenario. The transmitter-to-target-to-receiver Doppler shift, f'_B, for a moving ground target is due to the target and receiver motion. The relative bistatic Doppler shift is dependent on the target and receiver motion and position. Since only the receiver parameters are known, it is instructive to examine the worst case behaviour of f'_B as a function of the receiver velocity and direction of travel and for the largest likely surface target velocities.

$$f'_B = \frac{1}{\lambda} \left[2v \cos \delta \cos \frac{\beta}{2} + v_R \left(\cos \theta_L - \cos \theta_{TX} \right) \right] \tag{3.10}$$

The first term of Equation 3.10 describes the impact of the target's velocity on the Doppler shift. The term is maximised when the target is travelling along or in the opposite direction to the bistatic bisector when $\delta = 0, \pi$. It is minimised when the target is travelling normal to the the bistatic bisector when $\delta = \pm\pi/2$.

The Doppler bandwidth of moving clutter can be estimated by calculating the Doppler bandwidth associated with the fastest moving clutter, and as for the stationary clutter case, the worst case Doppler bandwidth can be calculated as:

$$\Delta f'_B = \frac{2}{\lambda} \left(2v + v_R \right) \tag{3.11}$$

An example of the Doppler response is shown in Figure 3.10 for a target moving along the bistatic bisector when $\delta = 0$, with a speed of 50 ms^{-1}. The receiver is moving in the direction indicated by the arrow at a speed of 40 ms^{-1}.
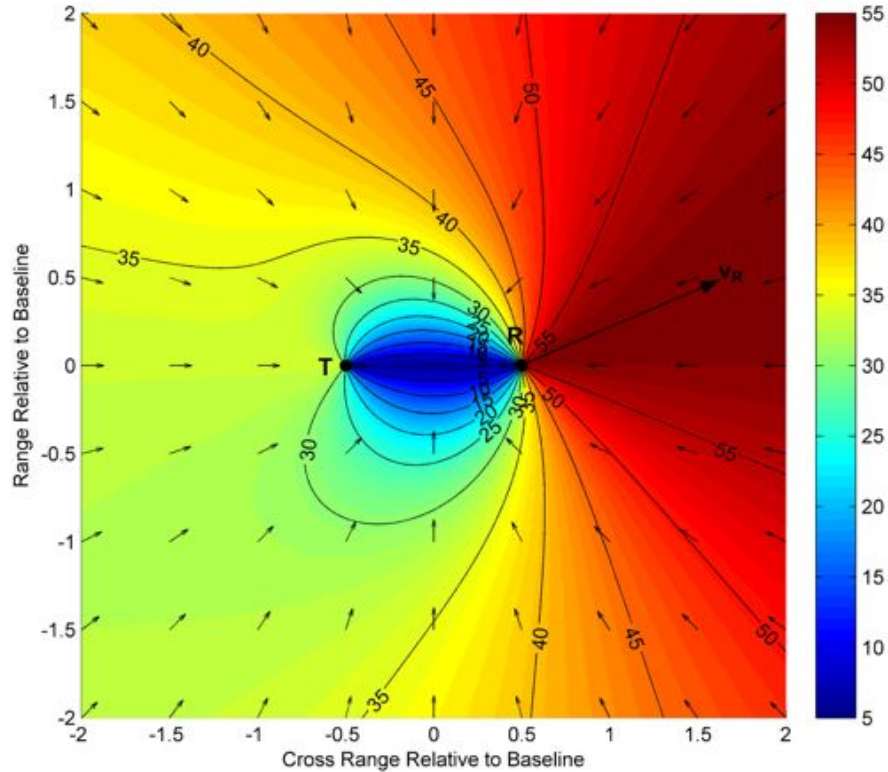
Figure 3.10: Bistatic Doppler scenario for stationary clutter. The transmitter is at [-0.5, 0] and receiver at [0.5 0] travelling at 40 ms^{-1} and at all points the clutter is moving along the bistatic bisector at 50 ms^{-1}, denoted by the arrows. The colour scale is in Hz.

As for the stationary clutter case, the maximum Doppler shift occurs in the direction of receiver travel, but in this case, the target crossing the baseline has a non-zero Doppler shift due solely to the target motion.

3.4.2 Target Doppler Shift

Calculation of the amplitude range-Doppler surface requires knowledge of the maximum target velocity. The maximum relative bistatic range of interest is determined by the receiver LoS and SNR limited detection range. The relative bistatic Doppler shift is determined by the fastest expected target to be detected. This work is concerned with the detection of civilian air targets and as shown in Table 3.1 the fastest expected target return is Mach 1. Instead of changing the extent of Doppler calculation from look to look, the Doppler limits will remain constant. The worst case target Doppler occurs when the target is on the extended baseline, $\beta = 0$, moving along the bistatic bisector towards the receiver,

as shown in the first row of Table 3.3. The largest negative Doppler shift is shown in row 2 and the zero Doppler scenario in row 3. For a target moving at Mach 1 (340 ms^{-1}) and the receiver moving at 50 ms^{-1}, the worst case Doppler limits are ± 260 Hz.

3.4.3 Bistatic Multipath Analysis

The direct signal forms the reference for the ARD calculation and hence the measured Doppler shifts are relative to the Doppler shift of the direct signal, due to the receiver motion. It is informative to understand the effect of the receiver motion on the multipath copies of the direct signal to ensure that it does not introduces excessive artifacts in the calculation of the range-Doppler surface.

A simple flat-Earth analysis of the multipath behaviour for the elevated moving platform is used to estimate the rate-of-change of the multipath and hence the relative bistatic range and Doppler of the multipath copies. The indirect path is described as $L' = M + N$ and
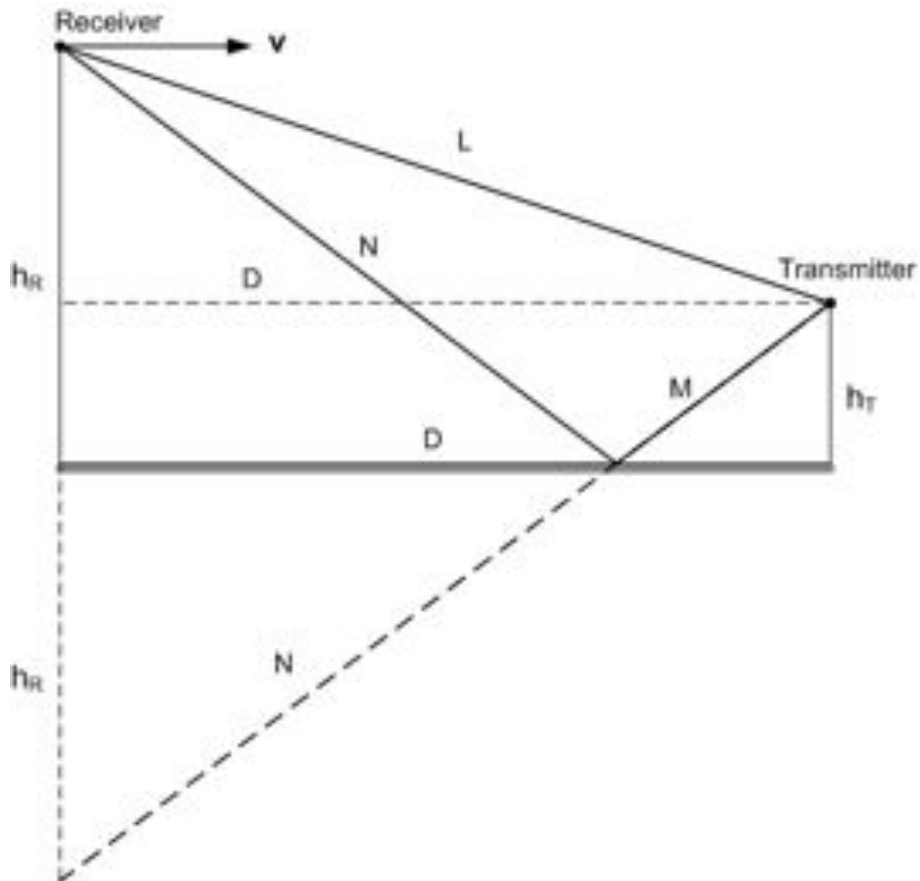
Figure 3.11: Geometry used for analysis of the multipath on the direct signal for a moving receive platform

the path difference between the direct path, ΔL is therefore

$$\Delta L = L - L' = -\frac{2h_R h_T}{D} \qquad (3.12)$$

It is instructive to examine what happens for a typical scenario with the receiver at an altitude of 1500m at a distance of 60km from the transmitter and an altitude of 400m. The difference in path length is 20m and hence the specular multipath return will be in the same range bin as the direct path signal. As the distance between the transmitter and the receiver increases the path difference decreases since $D >> h_R h_T$ and as $D \to \infty, \Delta L \to 0m$.

The relative bistatic Doppler shift of the reference signal multipath is estimated from the following simple analysis represented by the geometry shown in Figure 3.11. If the receiver has a velocity vector $\mathbf{v}$ parallel to the surface D and is heading radially towards the transmitter, the relative bistatic Doppler shift of the multipath component can be expressed:

$$f = \frac{1}{2\pi}\frac{d\Delta\phi}{dt} = -\frac{2h_R h_T v}{\lambda(D - vt)^2} \tag{3.13}$$

For a typical receiver speed of 40 ms^{-1}, the difference in Doppler shift between the direct and indirect multipath signals is of the order of a few milli-Hertz. For an integration time of 1s, the system will have a Doppler resolution of 1 Hz and hence the Doppler shifted multipath will fall into the same Doppler bin as the direct path signal.

The multipath on the reference signal and the direct path will appear in the DSI bin at zero range and zero Doppler. This means that applying the adaptive filter to the zero-Doppler bin will remove both the DSI and the DSI multipath.

3.5 Summary

A simulation has been developed based around realistic airborne passive radar system parameters. The results demonstrate that the example system would give a usable detection coverage for civilian aircraft targets. The system's sensitivity with respect to receiver noise has been investigated, Figure 3.5, and found to have baseline coverage up to 2 km altitude for baselines up to 100 km. For all receiver locations, the SNR is characterised by an altitude coverage, typically up to 5 km above the receiver. Detections operating in the thermal noise limited regime will have a very good altitude and baseline coverage. Analysis of the direct signal interference however, demonstrates that detections are likely to be in the direct signal limited regime.

For a receiver with 75 dB of dynamic range, equivalent to an ideal 12 bit ADC, it has been shown that the sensitivity of the receiver is vastly reduced when compared to the noise limited performance, Figure 3.6. As the baseline increases, the coverage reduces

until, for baselines greater than 50 km, the system allows detections in the receiver and transmitter centred regions. The result at longer baselines is a usable detection volume in the immediate vicinity of the receiver and transmitter, typically extending to 5 km in altitude and a 10 km radius in receiver to target range. The situation is improved if 10 dB of analogue cancellation of the direct signal in the surveillance channel is achieved, Figure 3.7. In this case, the SIR detection volume becomes comparable to the SNR detection volume.

The results of this initial study demonstrate a usable detection volume, even if no analogue cancellation is available. These results support the development of a demonstrator system for the detection of air targets and ground clutter data. The following specific conclusions from this analysis will feed into the hardware design stage:

- In order to achieve the SIR limited coverage estimated with a DR of 75 dB, the ADC must have a minimum of 12 bits. This will give enough DR to give the receiver a situational awareness capability and a limited coverage in the immediate vicinity of the transmitter

- Any direct signal cancellation that can be achieved will have the effect of increasing the interference coverage volume

- Due to coverage limitations, the transmitter needs to be chosen so that it is as close as possible to the air traffic approach paths being monitored. This will exploit the system's natural strengths of detection at low target altitude levels

- Doppler processing limits out to ± 260 Hz deviation relative to direct signal will allow targets with speeds up to Mach 1 to be detectable

- A CPI of at least 1 second is required in order to achieve enough integration gain for a 15 dB SNR, as shown by the SNR contours of Figure 3.5.

The following points will feed into the experimental planning phase:

- The receiver needs to stay above 200 m in order to maintain LoS with the transmitter at the maximum baseline of interest, 100 km

- The coordinates of the receiver position need to be known in order to perform offline target location processing.

Table 3.3: Scenario for minimum, maximum and zero Doppler for a moving receiver and target

Scenario		Target Direction of Travel wrt bisector, δ	Bistatic Angle, β	Look Angle, θ_L	Angle to Transmitter, θ_{TX}	Relative Bistatic Doppler Shift, f'_B (Hz)
1		0	0	0	π	$\frac{2}{\lambda}(v + v_R)$
2		π	0	π	0	$-\frac{2}{\lambda}(v + v_R)$
3		$\pi/2$	0	$\pi/2$	$\pi/2$	0

Chapter 4

Hardware Development

The collection of good quality airborne VHF data necessitates the design, construction and calibration of a portable, dual channel receiver system. The system specifications were summarised in Section 3.5 and these are used to design the receiver system in Section 4.1. The testing and calibration of the system is discussed in Section 4.2 including an examination of the gain and linearity of the completed system.

4.1 System Design

A block diagram of the receiver system, showing the main sub-systems and data flows is shown in Figure 4.1. The key parts of this system are the parallel RF to IF conversion via a superheterodyne receiver chain, the digitisation of the IF signal and the control and storage of the sampled data via a control laptop. The subsequent offline processing and data analysis is fully described in Chapters 5 and 6. This section uses the diagram of Figure 4.1 as a basis to explain the design methodology and performance of the system, starting with the ADC.

4.1.1 ADC

The choice of ADC was inevitably a compromise between performance and cost. From an ease of implementation perspective, the simplest approach would be to bandpass sample the entire FM spectrum, from 88 to 108 MHz. This is an attractive approach for four reasons. Firstly, directly digitising the 20 MHz spectrum means that all the FM signals from all the FM transmitters in the receiver's LoS are synchronously captured. This would allow location processing to be able to locate a target by examining the intersection of bistatic range ellipses from multiple transmitter-receiver pairs. Secondly, it gives the system
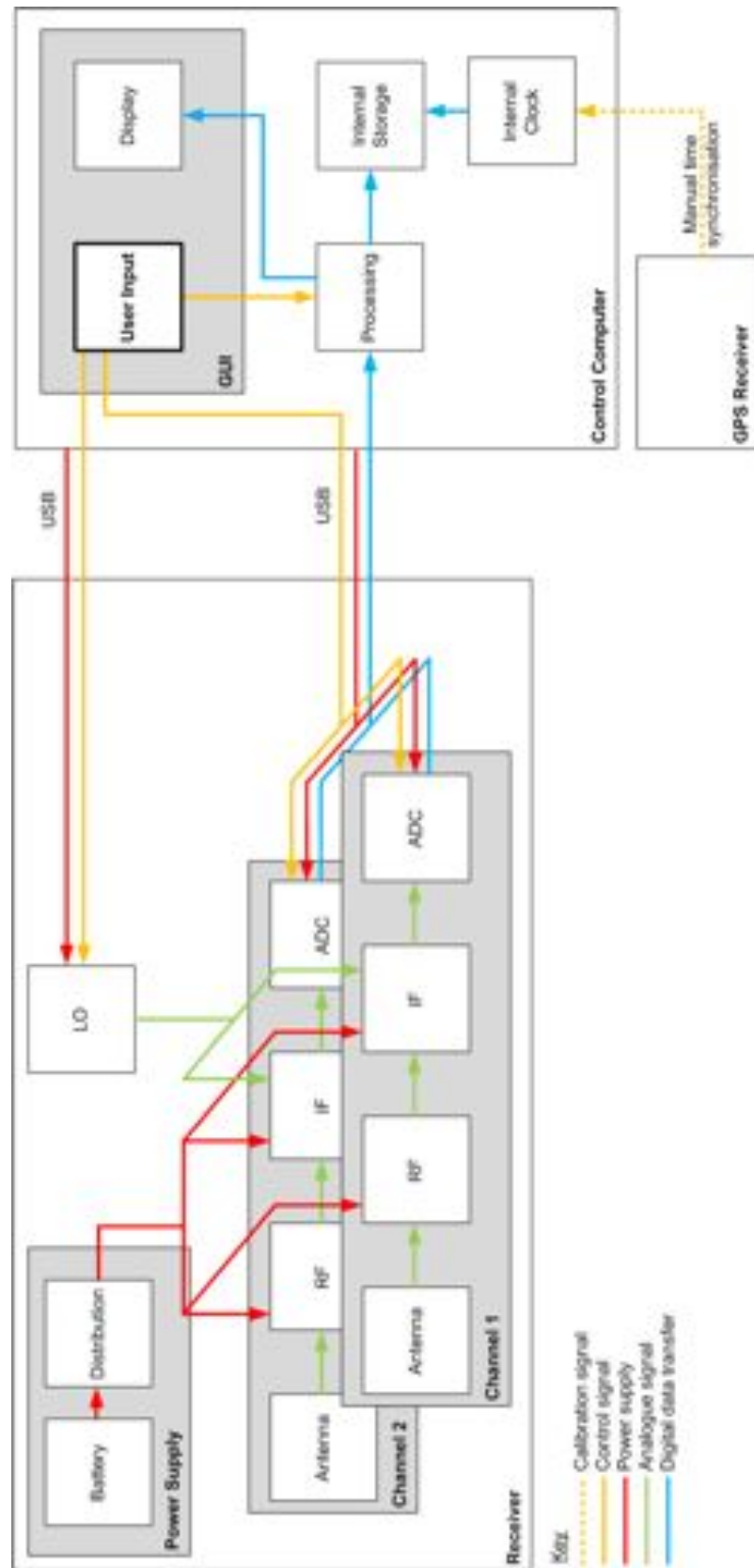
Figure 4.1: Receiver system block diagram

redundancy as the effect of multipath nulls, which occur as the receiver moves, means that a different channel on a different wavelength can be used for detection processing. Thirdly, it would allow all the channels to be rated in terms of instantaneous bandwidth and power. If

a channel from a favourable transmitter has a reduced bandwidth during the capture time, another channel with a larger instantaneous bandwidth from the same transmitter can be selected to compensate. Finally, the absence of a down conversion stage prior to digitising means that the system is simpler and the channels are more likely to maintain coherence. Additionally, fusing multiple channels together from the same transmitter linearly increases the bandwidth of the illuminating signal and increases the range resolution.

Digitising the full 20 MHz, however means that a lot of data is produced for each look. For example, a 1 second capture at 56 MHz and 16 bits is 112 MB/s. The maximum data rate of a USB 2.0 link is 60 MB/s and therefore each second of capture requires at least 2 seconds to download transfer to the computer and the system would need to have enough on board buffer to store the capture. Also, each individual FM channel in the 20 MHz spectrum would require separate offline filtering and downconversion in order to be of use for passive processing.

An ADC capable of capturing the FM spectrum whilst being powered and controlled by USB 2.0 was not available for this work. A less flexible but more realistic approach is to capture a single channel at a time and dynamically select the station based on the modulation content and switch transmitters in order to allow a multilateration approach. A revised system was designed based around the PicoScope 4224 USB Oscilloscope system[1] detailed in Table 4.1. Digitising a single channel at a time dictated that a further level of

Table 4.1: PicoScope 4224 parameters [63]

Parameter	Value
Number of channels	2 BNC inputs
Analogue Bandwidth	20 MHz
Voltage Ranges	± 50 mV to ± 100 V
Vertical Resolution	12 bits
Input Coupling	AC or DC
Input Impedance	1 MΩ || 22 pF
Full Scale Input Voltage	± 1 V
Maximum Sampling Rate	80 MS/s
Buffer Size	16 MS/channel
Power Supply	5 V @ 500 mA from USB port
Dimensions	200 mm $\times$ 140 mm $\times$ 38 mm
Weight	500 g

simulation and station management prior to use was required in order to ensure that the correct channel from the correct transmitter was chosen in order to confidently select the most appropriate transmitter.

---

[1]`http://www.picotech.com/picoscope4000-specifications.html`

This project is perfectly suited to a Software Defined Radio (SDR) approach however at the time this work was undertaken, the Universal Software Radio Peripheral (USRP) was still in its development stage and not proven, hence it was not available for the rapid deployment required for this project. The next iteration of this work would use the latest USRP as its flexible hardware and software architecture would make it suitable for a multi-band receiver system.

4.1.2 Analogue Receive Chain

The analogue receiver chain consists of the antenna, filtering and downconversion of the RF signal to a suitable IF prior to digitisation.

Antennas

The portable nature of the system meant that the antennas had to be internal and free standing to the aircraft's fuselage, fixed internally to the passenger windows. This ruled out the use of directional and hence physically large antennas and a telescopic whip antenna of the type commonly found on portable domestic FM receivers was used. A quarter wavelength monopole at 100 MHz would be 0.75 m long, which is still too large for the confined cabin space. This meant that the antenna would not be an efficient radiator and hence its installed gain would be considerably less than its free-space gain.

An assumed gain of -10 dBi was used for the remainder of the calculations. This value is revised through estimating the installed antenna gain in Chapter 7.

RF Filter

The FM band select filters are commercial FM bandpass receiver filters. The magnitude and phase of the S_{21} as measured in a 50 Ω system is shown in Figure 4.2 for both filters. The measurements show that the filters are well matched and have a typical passband loss of the order of 1.7 dB.

Amplification

In order to avoid introducing an Automatic Gain Control (AGC) subsystem to the front end, the level of amplification in the receiver was set for a worst case scenario. This gave a minimum operating separation from the transmitter in order to avoid saturation. To compensate for the decreasing signal as the receiver moves away from the receiver,
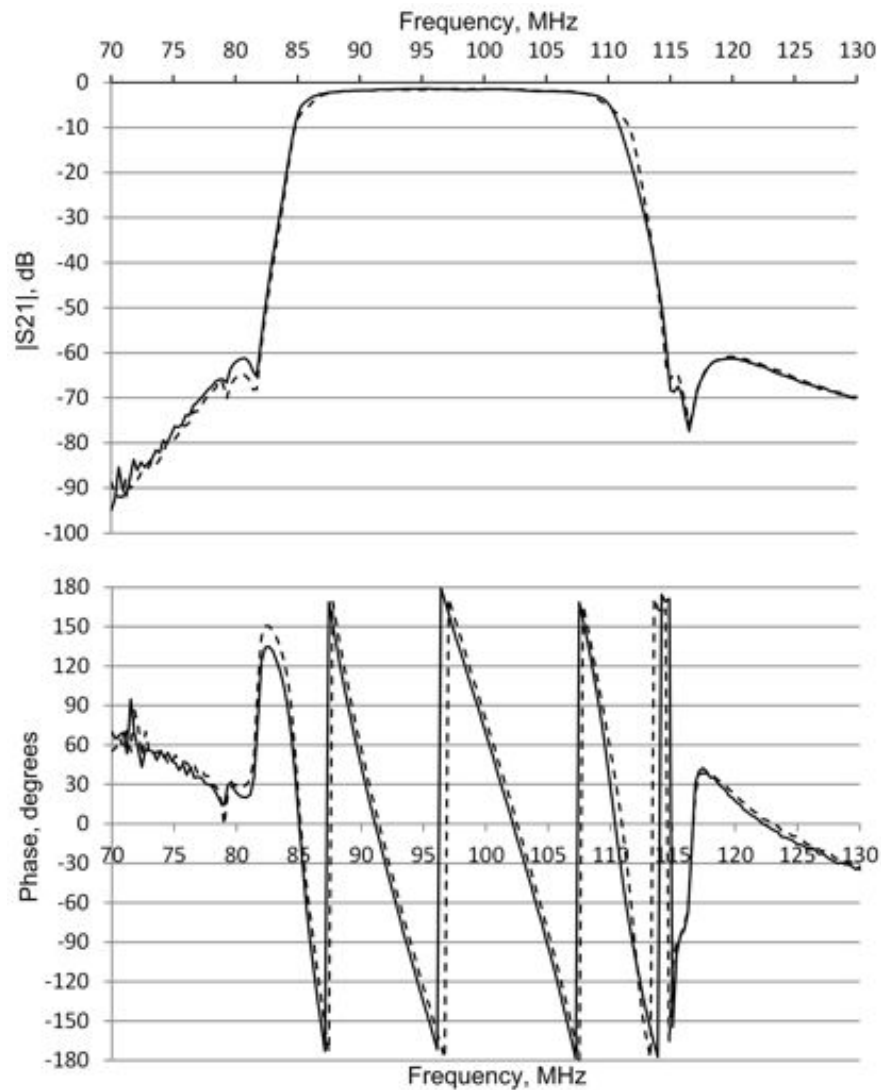
Figure 4.2: Magnitude and phase of S_{21} for the surveillance (solid line) and reference (dashed line) FM band filters

the ADC input voltage range was adjusted to ensure that the Received Signal Strength Indicator (RSSI) displayed a peak power 5 to 10 dB lower than 0 dBFS, where dBFS is dB relative to full scale input to the ADC.

The free space received power versus baseline for a -10 dBi antenna is plotted in Figure 4.3 based on theoretical received signal levels. A change in the gain of the receive antenna is reflected by a corresponding vertical shift of the curve.

Connectorised low-noise Minicircuits components were used for the system construction since it allowed the adjustment of the gain by either introducing attenuation or swapping the amplifier for a different gain model.
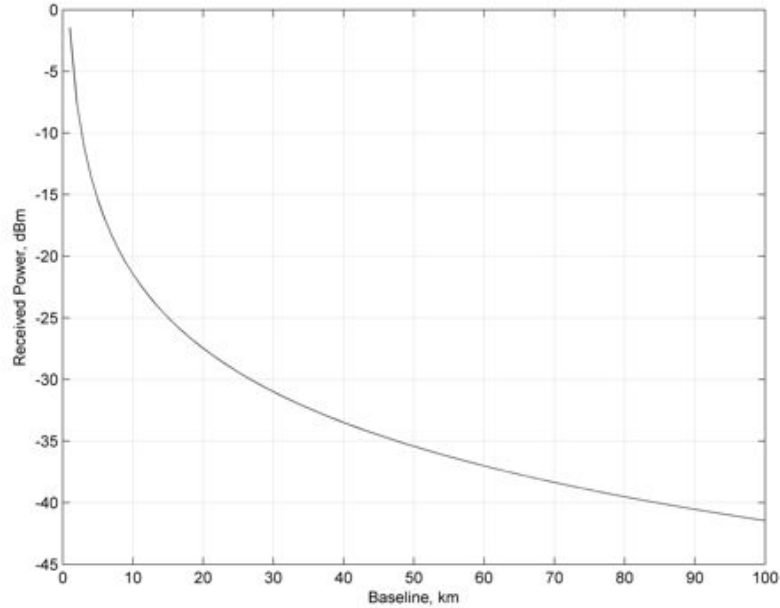
Figure 4.3: Theoretical free-space received power for Wrotham transmitter and a -10 dBi receive antenna

Local Oscillator

A USB controlled oscillator [64] was selected as the LO for this work. The module was constructed and mounted in a die cast metal box, the circuit board is shown in Figure 4.4. The stability of the oscillator was measured over 35 minutes after a 20 minute warm up, using a spectrum analyser. Over the 35 minute observation period, the oscillator was found to vary by 10 Hz, equivalent to 0.005 Hz/s drift and more than stable enough for this purpose.

The oscillator was powered and controlled via the control laptop's USB. The supplied control program allowed the adjustment of the oscillator frequency. A script allowed the frequency to be set via a LabView interface and hence the selection of the frequency was done by the computer, dependent on the operator's requirements. Low side frequency mixing was used to achieve the desired IF frequency, 10.7 MHz, to align with the IF filter's passband, therefore the LO frequency was chosen as shown in Equation 4.1. Where f_{RF} is the centre frequency of the station of interest and f_{IF} is the 10.7 MHz IF frequency.

$$f_{LO} = f_{RF} - f_{IF} \tag{4.1}$$
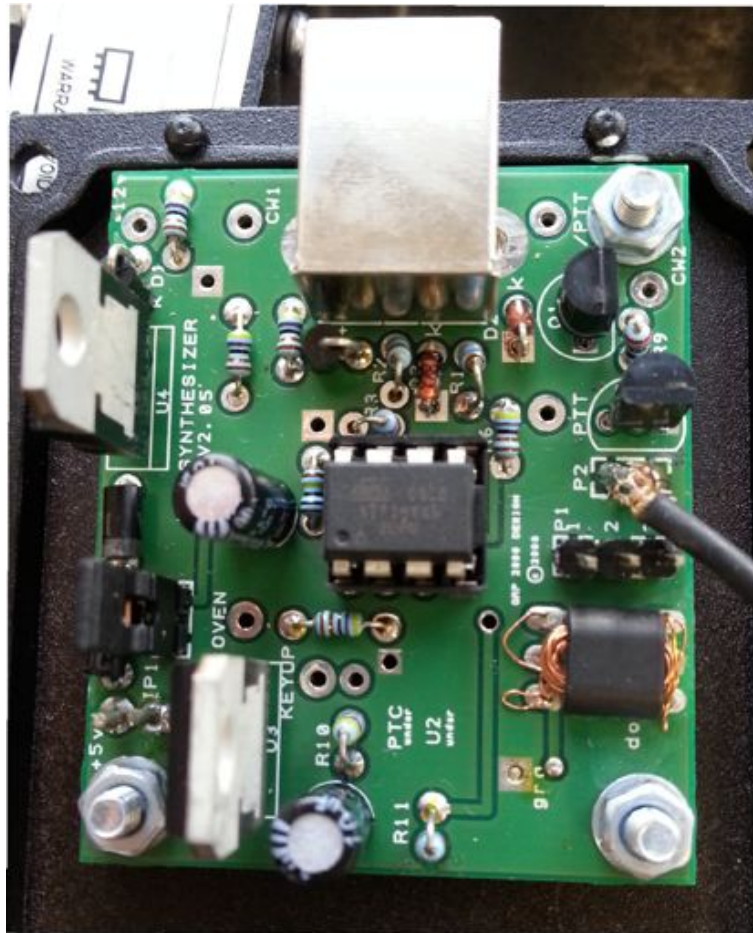
Figure 4.4: USB controlled oscillator

Channel Selection Filter

The channel selection filters or IF filters, are ceramic filters with a nominal centre frequency of 10.7 MHz and 3 dB bandwidth of 150 kHz. They have an inherent insertion loss of 4.5 dB however their input and output impedance is 330 Ω. The magnitude and phase of the filter response for the reference and surveillance channel filters, as measured in a 50 Ω system are shown in Figure 4.5. In the pass band the difference in magnitude is no more than 2 dB and the difference in phase is no more than 20°. The passband loss of the filter is high at 10 dB, however 6 dB of this is a result of the mismatch loss associated with working in a 50 Ω system.

4.1.3   Sampling Frequency

The choice of sampling frequency is dependent on the passband bandwidth of the channel select filter. The FM spectrum between 88 and 108 MHz, is densely packed typically with 300 kHz between FM carriers and each channel having a maximum bandwidth of 200 kHz. With the channel of interest downconverted to 10.7 MHz, it is important to make full use of
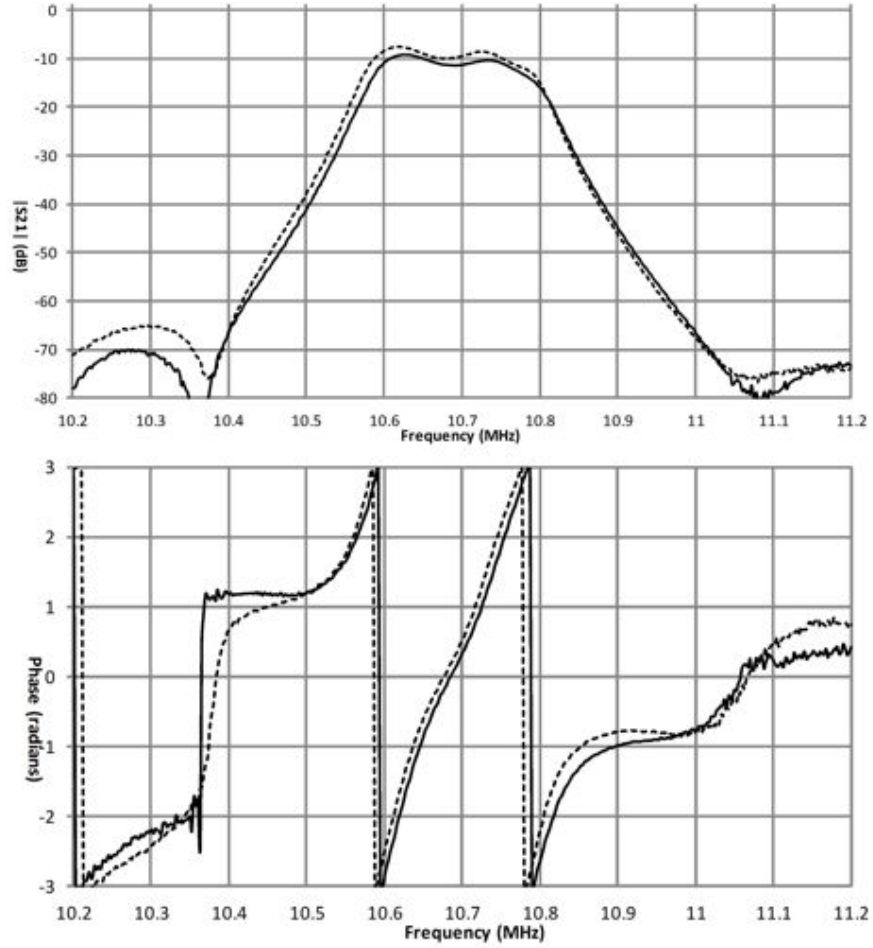
Figure 4.5: Magnitude and phase response of reference (dashed line) and surveillance (solid line) IF filters, measured in a 50 Ω system

the IF filter skirts to reduce adjacent channel signal power. With reference to Figure 4.5, a channel at 11.1 MHz and 10.4 MHz will still have components in the IF filter passband, at least 60 dB below the desired signal power. In order to prevent these components aliasing into the channel of interest, the sampling frequency must be high enough to make use of the full filter roll-off, effectively introducing a guard band either side of the signal of interest. Post-processing can then be used to further isolate the 10.7 MHz baseband channel.

For the band confined to the interval $[f_L, f_U]$ the allowable bandpass sampling frequencies fall into the range described by Equation 4.2 [65].

$$\frac{2f_U}{B} \leq f_S \leq \frac{2f_L}{n-1} \tag{4.2}$$

Where n exists in the range of integers given by Equation 4.3.

$$1 \leq n \leq \lfloor \frac{f_U}{B} \rfloor \tag{4.3}$$

Where $\lfloor \cdot \rfloor$ represents the largest integer, or floor, of $\frac{f_U}{B}$. In this case, with reference to Figure 4.5, the lower limit is taken as 10.2 MHz and the upper limit as 11.2 MHz. For an upper limit of 11.2 MHz and a hence a bandwidth, B, of 1 MHz, the integer n varies between $1 \leq n \leq 11$. The allowable range of sampling frequencies with increasing integer n is shown in Figure 4.6 by the blue lines. The allowable discrete selection of ADC sampling frequencies are shown as black horizontal lines. The sampling frequency needs to be as low as possible in order to reduce the data rate however it needs to be large enough to capture the entirety of the IF signal bandwidth and maximise the roll-off introduced by the filter skirts. The sampling frequency also needs to be one of the discrete allowable sampling frequencies of the PicoScope ADC. The sampling frequency of 2.86 MHz was
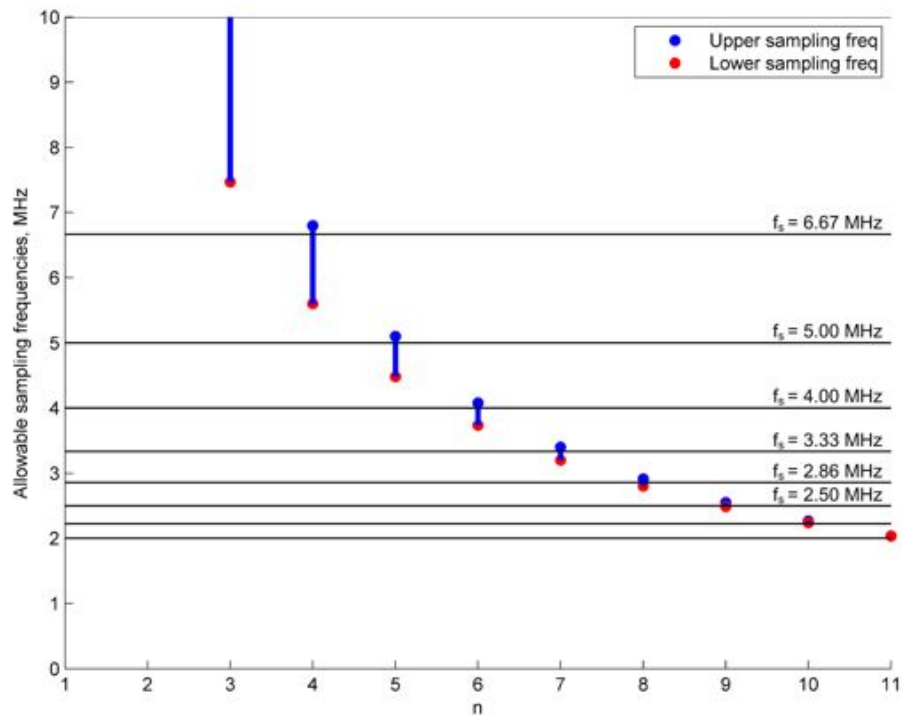
Figure 4.6: Sampling frequency selection

chosen as a compromise between data rate and filter roll-off. A schematic of the sampled spectrum compared to the IF spectrum is shown in Figure 4.7. The IF channel lies in an even Nyquist zone, therefore the sampled spectrum will be spectrally reversed, sitting at f_{ss} in the picture, and this will need to accounted for in the subsequent processing.

4.1.4 Power Requirements

As shown in Figure 4.1, the LO and ADC are powered by the laptop via the USB. To ensure that the system was capable of operation for two hours, the five amplifiers must be powered by a battery since the LO and ADC were drawing all the available power from the
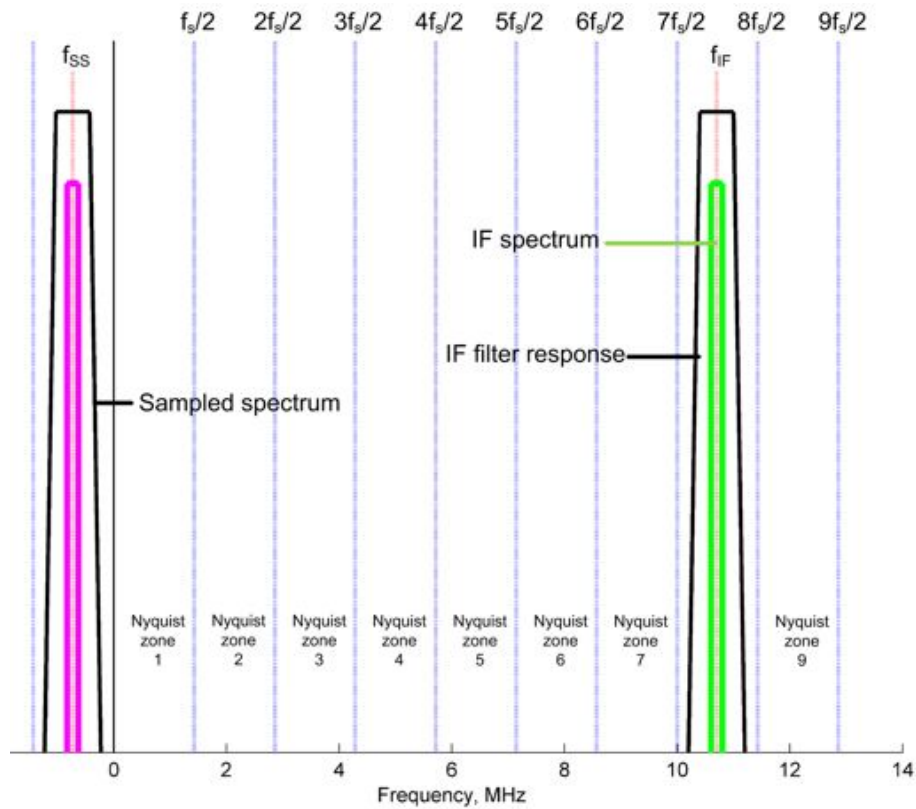
Figure 4.7: Frequency spectrum before and after sampling

laptop via the USB interface. Each amplifier typically draws 60 mA at 12 V therefore a 12 V 600 mAh battery was required. Rechargable batteries were selected and charged prior to the experiment, one acting as a primary and the second acting as a spare.

4.1.5 Theoretical Receiver Gain and Noise Figure

The cascaded gain and noise figure of the receiver chain was calculated from the component datasheets. A block diagram of the receiver front-end, along with the nominal gain and noise figure values, is shown in Figure 4.8. The calculation of the cascaded gain and noise figure is shown in Table 4.2. The nominal channel gain is 27 dB and the noise figure is 6.5 dB. These were later compared to the measured values.

4.1.6 Operating Modes

The system has three operating modes:

- **Manual** The transmitter and ADC input voltage range is selected manually through the GUI based on the RSSI feedback. This mode is used to manually characterise the available illuminators, the signals with good modulation and RSSI were noted down for use in the single and dual data collection modes.
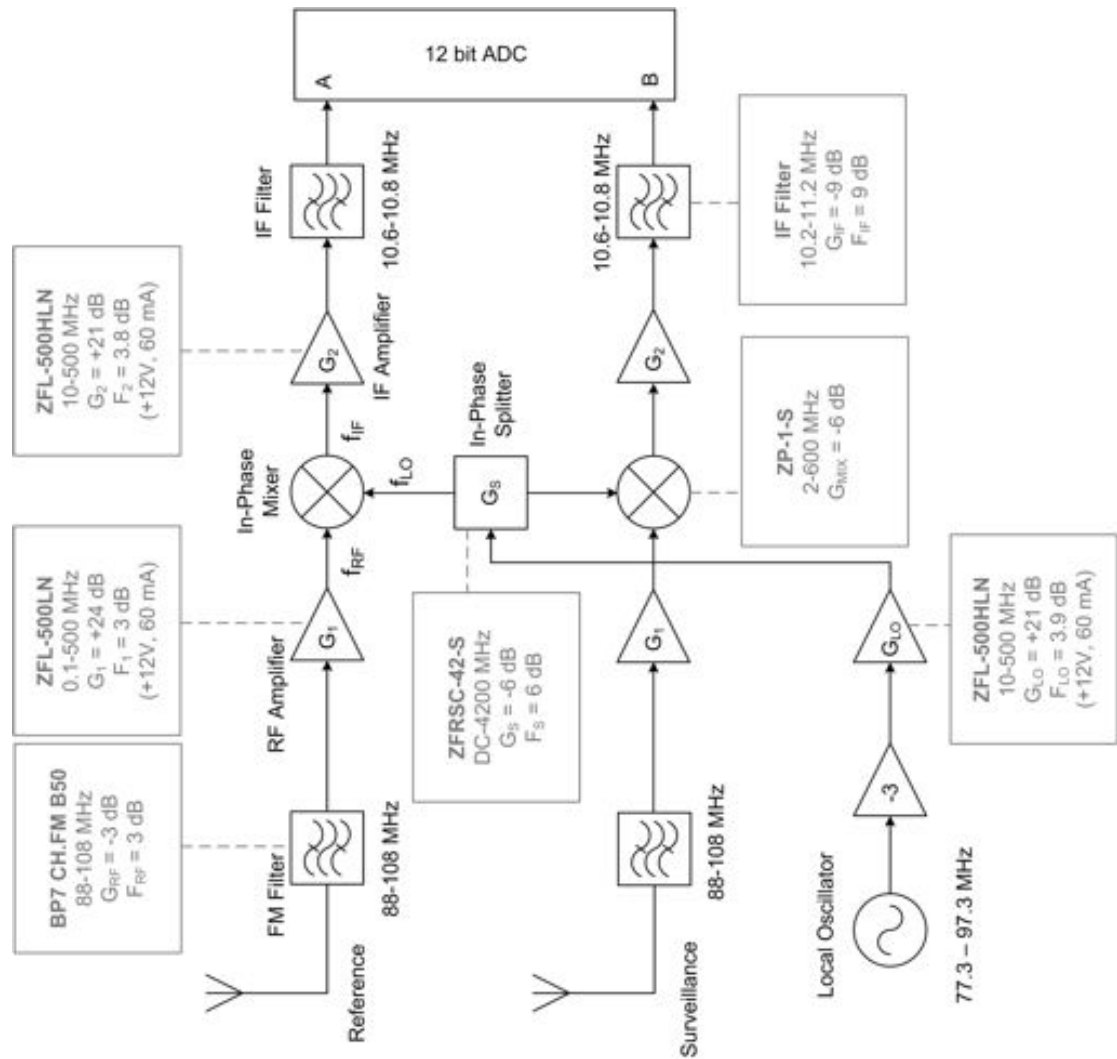
Figure 4.8: Block diagram of the dual channel receiver system with system component details

- **Single Transmitter** In this mode, the illuminator is manually selected as one of the four BBC radio stations transmitted from Wrotham transmitter. The modelling work had identified this transmitter as the most reliable illuminator for the experimental scenario.

- **Dual Transmitter** The receiver sequentially switches between two transmitters. The aim of this mode was to successively form two transmitter-receiver pairs and allowing detections to be cross-referenced to allow target localisation beyond the bistatic range and Doppler through multilateration processing. The transmitters available for the second illuminator in this mode, the BBC stations from Oxford, Crystal Palace and Guildford are selectable.

In all three of these modes, the capture time is manually selected and is determined by the data collection mode: 1s for RSSI analysis, 2s for target detection or 3s for clutter

analysis. The LabView GUI, shown in Figure 4.9, is used to control the receiver and select the receiver operating mode.
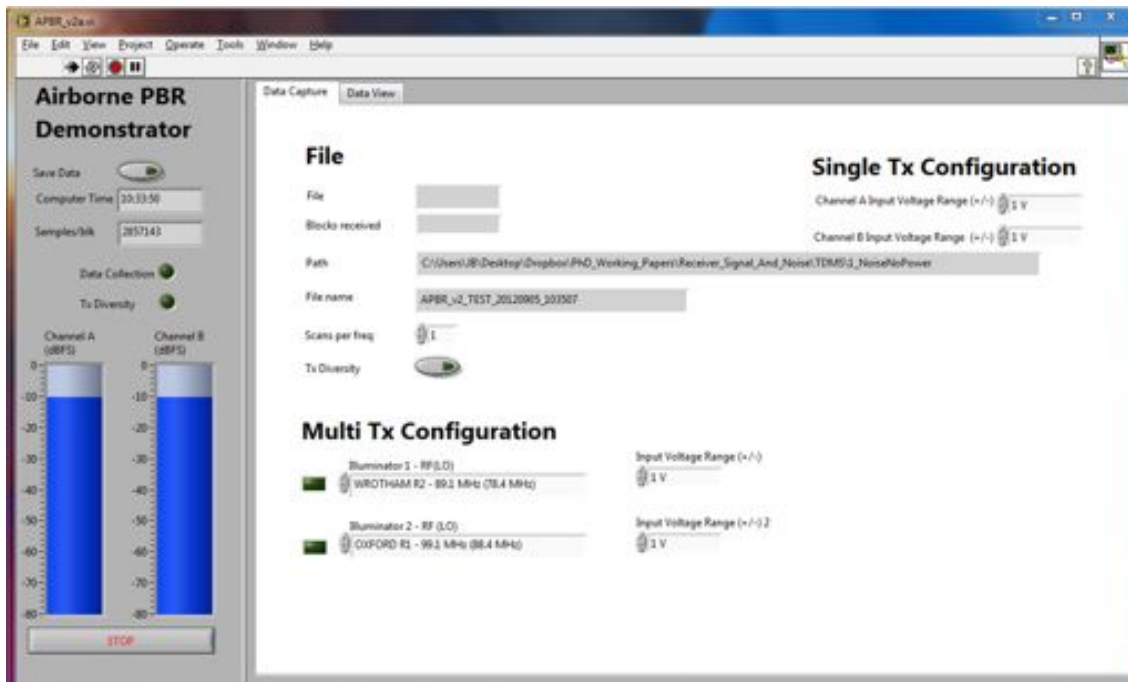
Figure 4.9: LabView control software running on the control laptop

4.2 Receiver Characterisation

4.2.1 Receiver Linearity

The 1 dB compression point and output 3rd order intercept point for the RF frontend were measured in the laboratory. The extrapolation of the output 1 dB compression point and small-signal gain for both channels is shown in Figure 4.10. The gain of channel 1 is 31.5 dB and the gain of channel 2 is 30 dB. The gain misimatch between the channels can be attributed to the differing pass-band losses of the FM and IF filters. The output 1 dB compression point is a measure of the maximum output power of the receiver and it is important that output power is kept below the 1 dB compression point to ensure that the receiver circuitry does not saturate and go into a non-linear regime. The input power therefore needs to be below -30 dBm to ensure that the receiver is in its linear region. With reference to the free-space received power calculated in Figure 4.3, this maximum input power to the receiver equates to a minimum operating range of 30 km, for a -10 dBi antenna, and hence the experimental flight path will be chosen to ensure that this is assured.

A two-tone test was performed using a tone at 98.79 MHz and 98.81 MHz. The level of
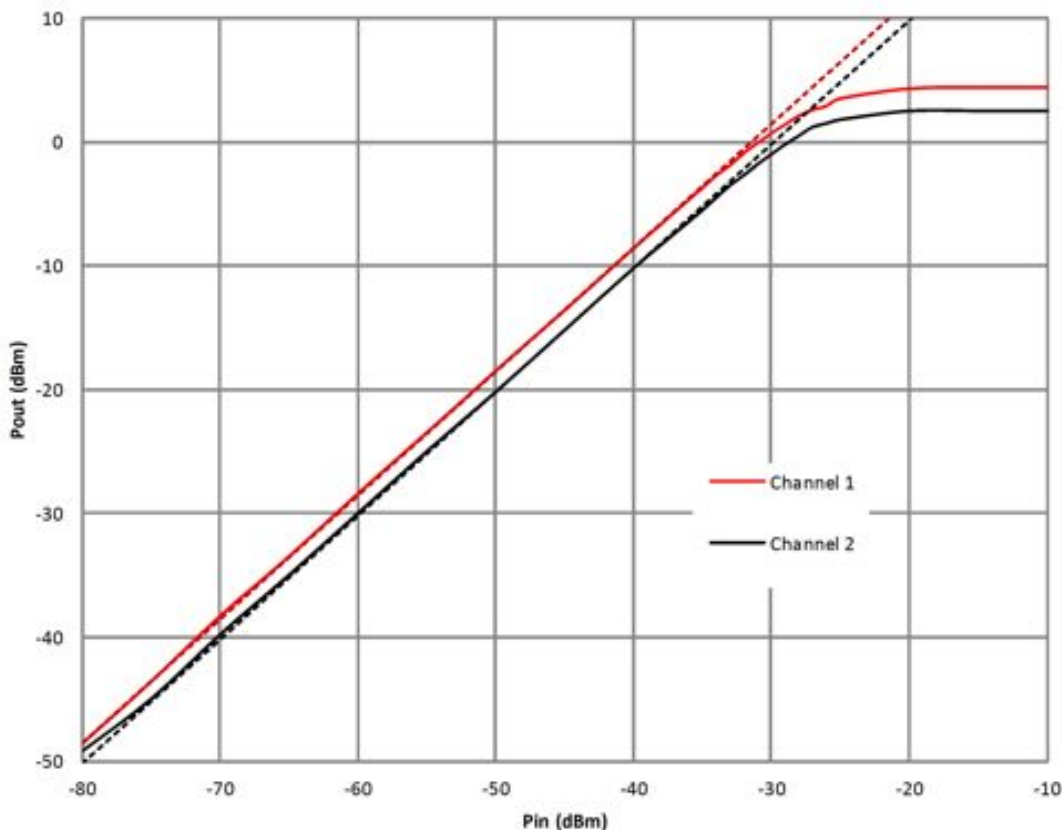
Figure 4.10: 1 dB compression point measurements

the third order intermodulation products at $2f_1 - f_2$ and $2f_2 - f_1$, 98.77 MHz and 98.83 MHz respectively, were measured with increasing input power, from -50 dBm to -35 dBm. The output third order intercept point for channel 1 is shown by the intersection of the extrapolated lines of Figure 4.11. This shows that when the input power of the signal is at -21 dBm, the level of the third order intermodulation products will be at the same level as the fundamental frequencies, due to the non-linearity of the receiver. Although this is a theoretical number, since the receiver would be in compression before this point, it serves to show that in the intended operating range the receiver will be operating in the linear regime. In summary, the channel gain, output 1 dB compression point and the output third order intercept point for both channels are shown in Table 4.3.

4.2.2 Absolute Signal Levels

The full-scale input power of the ADC in the ±1 V range is +5 dBm. To confirm this a tone test was completed where an input tone of -40 dBm at 98.8 Mhz was applied to both channels. This is 15 dB below the full scale input power and the ADC registered an average power of -15 dB relative to the full scale power, or -15 dBFS, as expected. The full-scale
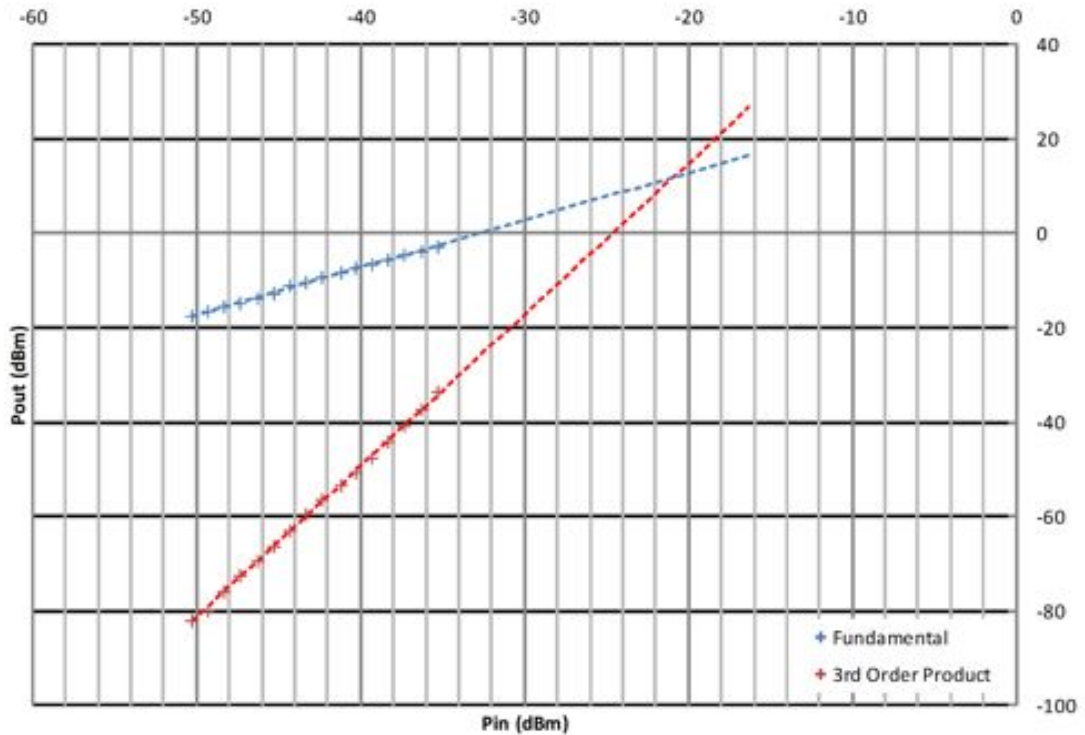
Figure 4.11: Third order intercept point extrapolation for the reference channel

input powers for the other input voltage selection modes are shown in Table 4.4

The system was installed at UCL and the 98.8 MHz FM channel from Wrotham transmitter 37 km away used for a direct signal capture. Radio 1 was used for this experiment since it provides the best modulation bandwidth and hence range resolution. This is at the expense of having a lower ERP than Radio 2. The free-space path loss for this scenario is 104 dB and the transmitter is transmitting a slant polarised signal at 125 kW (81 dBm) and the receive antenna has a peak gain of 8 dBi with a free-space front to back ratio of 16 dB. In this setup, the surveillance antenna is horizontally polarised and the backlobe of the antenna is pointing toward the transmitter giving a notional gain of -8 dBi on the direct signal. The free-space received signal in the surveillance channel assuming negligible cable loss at the input to the receiver is therefore -34 dBm. This was measured as -49 dBm at the input to the receiver.

The reference channel uses a vertically polarised halfwave dipole with a theoretical gain of 2.15 dBi and omnidirectional in azimuth radiation pattern, this gives a theoretical received power of -24 dBm at the input to the receiver. This was measured as -44 dBm. The difference between the theoretical and actual received signal level is due to the transmitter being on the opposite side of the UCL engineering building to the transmitter. This has previously been shown to give at least 10 to 15 dB in shielding in direct signal [66].

The installed performance of the dipole and Yagi antennas are not known however the initial results demonstrated that the RF front-end and ADC was working as designed. In the airborne scenario, the antennas will have LoS to the transmitter therefore this would be confirmed as part of the flight trials.

4.2.3 System Noise

The noise figure of the 50 Ω downconversion stage not including the 330 Ω channel select filter, was measured using a Noise Figure Meter. The results for both channels are shown in Figure 4.12. The ADC SNR was estimated by injecting a 10.7 MHz tone at -1 dBFS
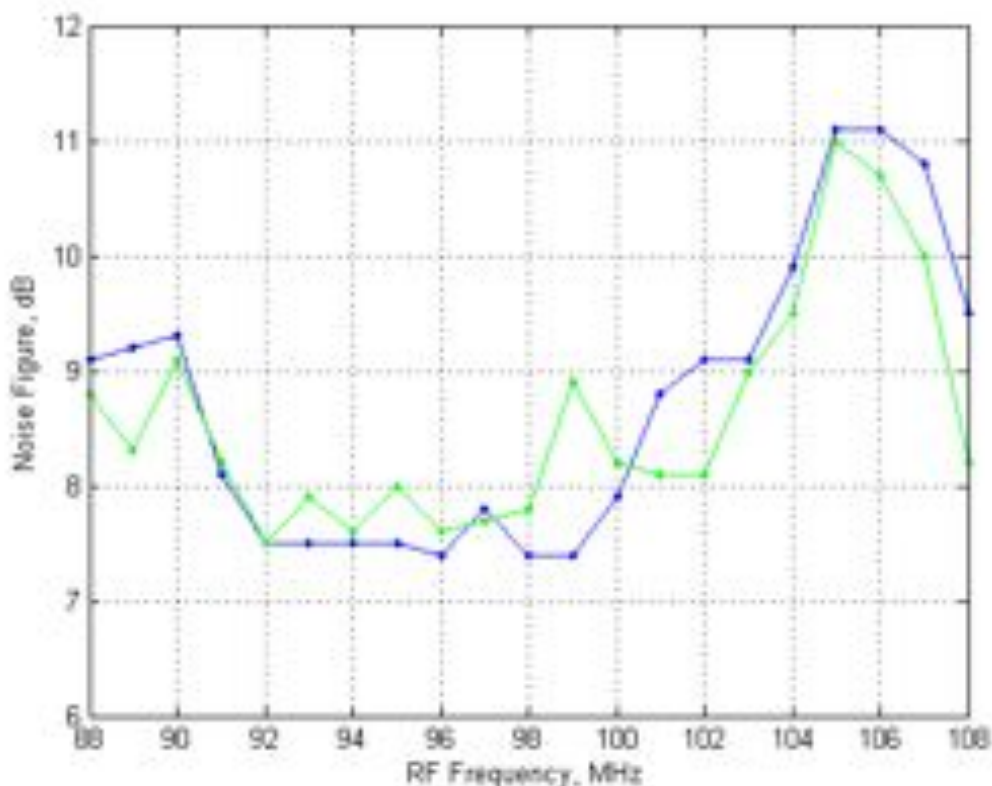
Figure 4.12: Pre-IF filter noise figure measurement

and integrating the noise away from the tone over half the sampling frequency. The SNR was measured as 72 dB, which is close to the ideal value of 74 dB for the 12 bit ADC. The overall system noise figure, including the high-gain 50 Ω frontend, the 330 Ω channel select filter and the ADC is shown in Figure 4.13. The theoretical noise performance of the RF hardware is low however the dominating noise in this system is the quantisation noise of the ADC. The mid-band noise figure is 22 dB and as shown in the simulation work, it is low enough to provide a usable noise limited coverage.
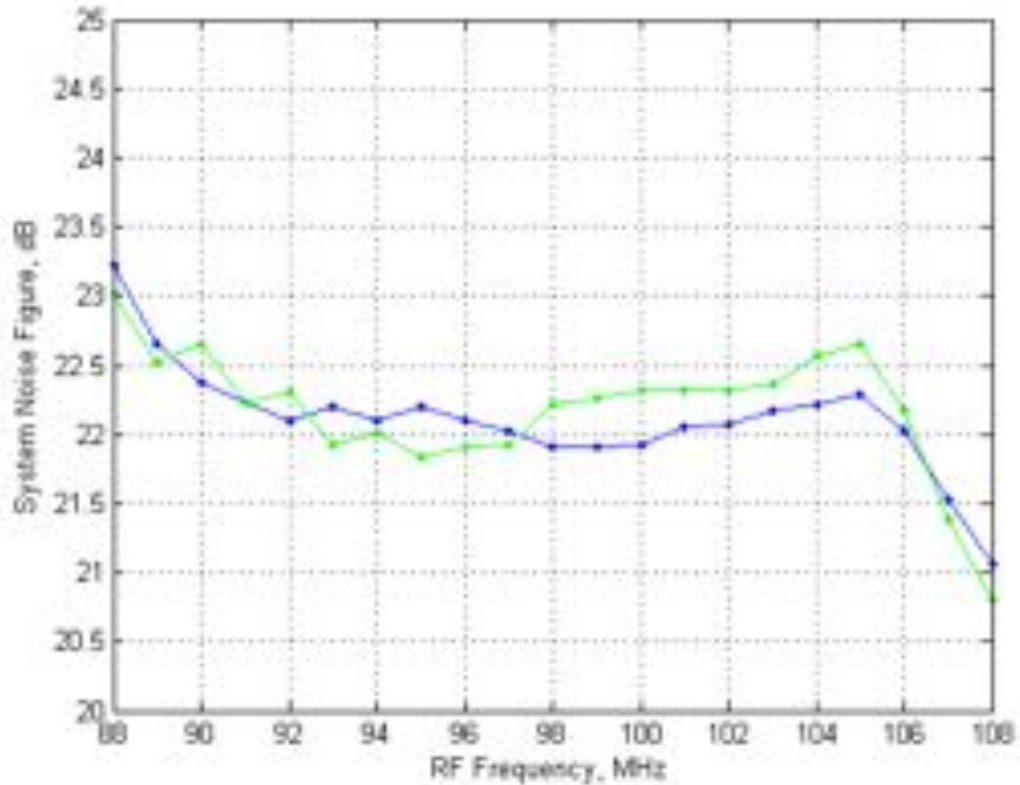
Figure 4.13: System noise figure measurement

4.3 Summary

The design, construction and testing of the receiver system has been described. The system design will allow the digitisation of a single FM channel. For 2D localisation experiments, the system can be commanded to switch between two transmitters. Measurements have shown that the receiver has a linear response over the intended operating range of RF frequencies and intended input powers. The system noise performance over the intended operating range has been characterised and found to be at an acceptable level. There is a minimum baseline requirement to ensure that the receiver is not saturated. This will allow the flight path to be chosen to ensure that the receiver does not go into compression.

The finished product is pictured in Figure 4.14 and the boxed system in Figures 4.15 and 4.16.

Figure 4.14: Completed receiver - under the lid

Figure 4.15: Completed receiver ready for experimental data collection - front interface

Table 4.2: Theoretical receiver noise figure and gain calculation

Per channel		Antenna	FM Filter	RF Amp	Mixer	IF Amp	IF Filter
Input Power	dBm	-	-20.0	-23.0	1.0	-5.0	15.5
Component Data							
Gain	dBm	-	-3.0	24.0	-6.0	20.5	-9.0
Output IP3	dBm	-	-	14.0	-	30.0	-
Noise Figure	dB	-	3.0	3.0	6.0	3.8	9.0
Max Input Power	dBm	-	-	-17.0	-6.0	-5.5	-
P_{OUT} at 1 dB Compression Point	dBm	-	-	8.0	1.0	16.0	-
Linear Data							
Gain	linear	-	0.5	251.2	0.3	112.2	0.1
Noise Factor	linear	-	2.0	2.0	4.0	2.4	7.9
Linear Cascaded Gain							
Gain Product	linear	-	0.5	125.9	31.6	3548.1	446.7
Cascaded Noise Figure							
Noise Factor	linear	-	2.0	4.0	4.0	4.0	4.1
Cascaded Gain and Noise Figure							
Gain	dB	-	-3.0	21.0	15.0	35.5	26.5
Noise Figure	dB	-	3.0	6.0	6.0	6.1	6.1
Output Power	dBm	-20.0	-23.0	1.0	-5.0	15.5	6.5
RMS Output Voltage	V_{rms}	-	-	-	-	-	0.6

Table 4.3: Measured channel parameters summary

Channel	Gain	OP1dB	OIP3
1	31.5 dB	0 dBm	12 dBm
2	30.0 dB	-1 dBm	10 dBm

Table 4.4: Full-scale input power variation with input voltage range assuming a 30 dB channel gain

Identifier	Full-scale input voltage to ADC	Max frontend i/p power	Max ADC i/p power
2	± 50 mV$_{pk-pk}$	-49 dBm	-19 dBm
3	± 100 mV$_{pk-pk}$	-45 dBm	-15 dBm
4	± 200 mV$_{pk-pk}$	-39 dBm	-9 dBm
5	± 500 mV$_{pk-pk}$	-31 dBm	-1 dBm
6	± 1 V$_{pk-pk}$	-25 dBm	+5 dBm

Figure 4.16: Completed receiver ready for experimental data collection - rear aspect

Chapter 5

Airborne Experiments

5.1   Introduction

To demonstrate the proof of concept of airborne passive radar, it was crucial that the probability of detection of commercial air targets was maximised. This chapter describes the experimental scenario used to obtain air target detections. The airborne platform was based at Shoreham airport on the south coast of the UK therefore the experimental operational area had to be within a short flight of the airport. This chapter discusses the platform, its operating parameters, the available FM illuminators and the potential air targets. The two airborne experiments carried out are then documented and the initial processing described. Whilst collecting airborne target data there will inevitably also be a large amount of clutter data recorded. The clutter data will be discussed in more detail in subsequent chapters.

5.2   Experimental Scenario

5.2.1   The Airborne Platform

The airborne platform available for the experimental campaign was based at Shoreham airport on the south coast of England. It was well placed for experimental data collection in the densely populated airspace to the south of London. The Piper Archer PA 28-181 [67] is a four-seat light aircraft, it is shown flying in Figure 5.1 and for reference, the dimensions of the aircraft are shown in Figure 5.2.   An air chart showing the general operational area is shown in Figure 5.3. It depicts Shoreham Airport, the restricted airspace around Gatwick airport and the three navigation beacons which were used as reference points

Figure 5.1: PA 28-181 G-BMIW airborne.
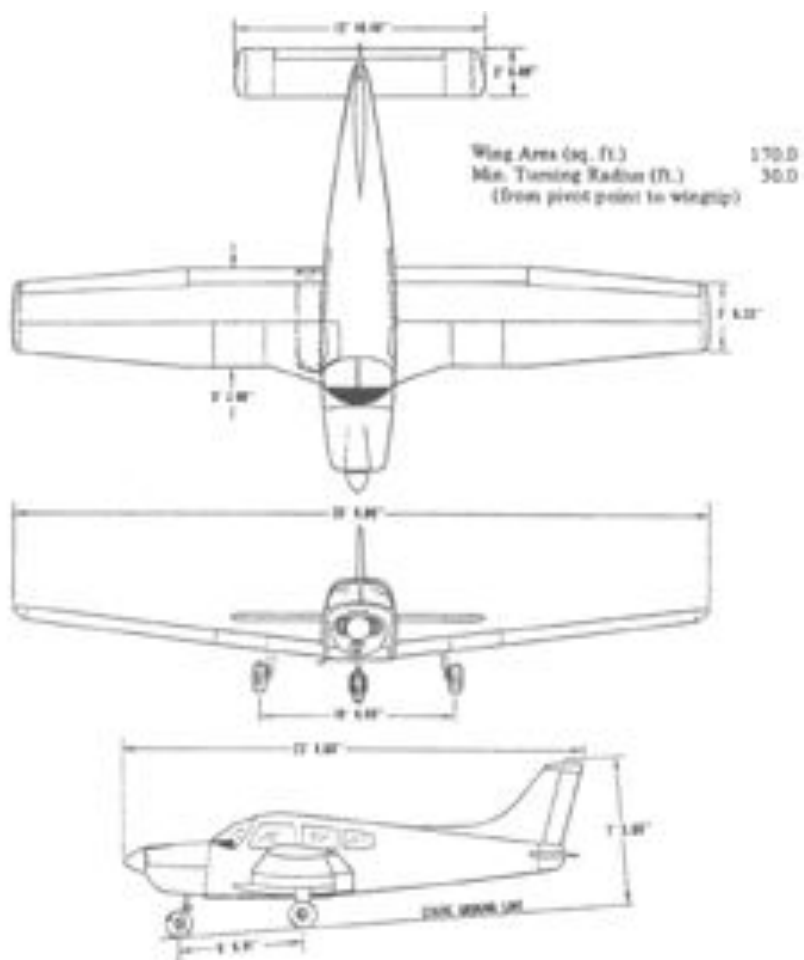
Figure 5.2: Airborne platform dimensions, taken from [67]
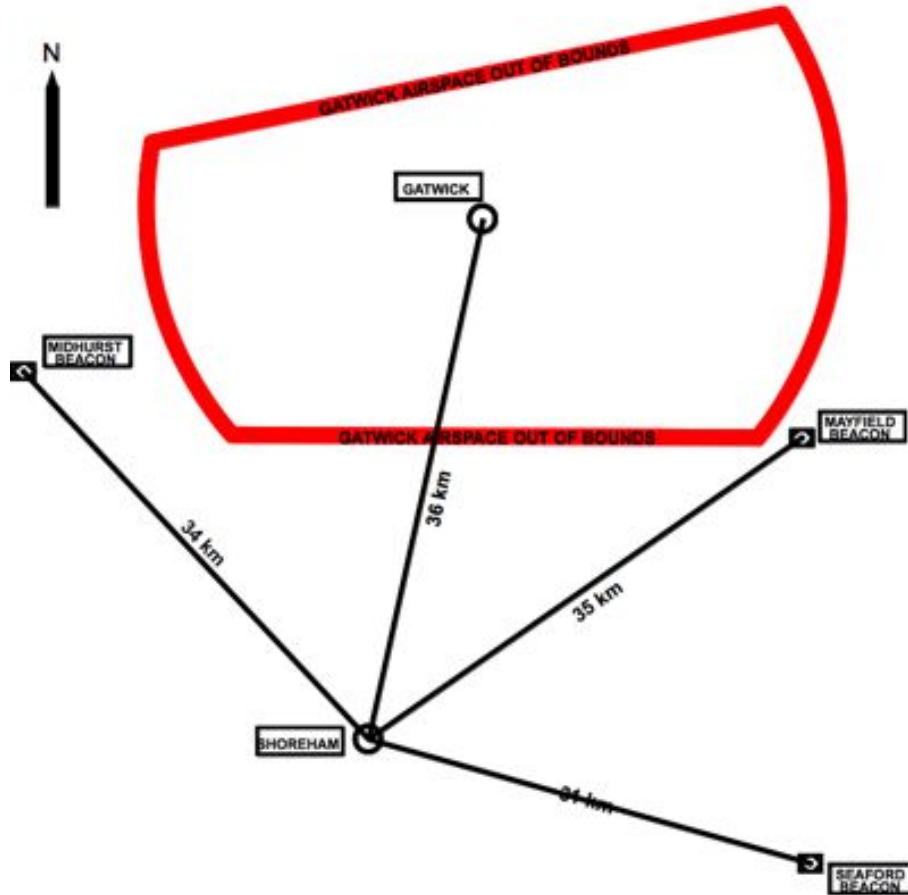
Figure 5.3: Relative air chart of intended operating area. The receiver aircraft is based at Shoreham Airport.

for construction of the experimental flight path. The distance measurements give the approximate ground distance between Shoreham Airport and Gatwick Airport, Midhurst Beacon, Mayfield Beacon and Seaford Beacon. With the receiver travelling at 100 knots (50m/s) the distances roughly represent 10 minutes of flying time.

To comply with certificate of airworthiness requirements, the receiver antennas had to be placed inside the aircraft and could not be attached to the chassis. The size of the window aperture had an impact on the receive antenna dimensions. The dimensions of the passenger window, situated over the wing, constrict the length of a horizontally polarised rod antenna to 550mm and a vertically polarised rod antenna to 350mm. For an FM signal with a wavelength of 3m, the antenna is limited in length from 0.12λ to 0.18λ, it is expected therefore that the receive antenna efficiency will be low. As part of the first airborne experiment the antenna gain was estimated. Unlike the platform used for Kulpa's airborne collection campaign [55], the wings are below the fuselage, the landing gear does not retract and the propeller has two blades. An early hypothesis stated that

Table 5.1: PA 28-181 operating parameters

Parameter	Typical	Maximum
Cruising Speed	115 knots	125 knots
Altitude	3,000 feet	14,000 feet

the operation of the passive receiver above the aircraft's wings would give some shielding from the surface clutter returns. The typical and maximum operating parameters for the PA 28-181 are shown in Table 5.1.

5.2.2   FM Illuminators

Having defined the airspace of interest in Section 5.2.1, the location and nature of the FM illuminators were identified. There is a high density of FM illuminators in the south of England, with high power national transmitters providing BBC access and smaller gap-filler transmitters around London transmitting both national BBC content and local commercial radio stations. The national BBC FM transmitters are tabulated in Table 5.2 and the lower power local BBC FM transmitters are tabulated in Table **??**. The numerous independent radio stations, such as Classic FM, are typically broadcast from co-located transmitters however they have not been considered here. In the following analysis, the higher power national BBC transmissions will be exploited.   The location of the transmitters are mapped out in Figure 5.4. The background of this image is a Digital Elevation Map of the south coast region. As expected it is seen that the main high power transmitters are placed on high ground and the gap-fillers are in the areas that are out of LOS of the high power transmitters.

The range-resolution of the processed data, is dependent in part on the modulating bandwidth of the transmitted signal and hence the bandwidth of the information being broadcast. Previous work has shown the bandwidth of FM broadcasts to vary between 10 kHz for speech, to 80 kHz for reggae, [21]. It is interesting to note that for speech, the silence in pauses in speech give the minimum bandwidth and hence a loss of resolution. It is prudent therefore to select stations transmitting pop music such as BBC Radio 1 and 2.

5.2.3   Air Targets

In the UK, the position and heading of aircraft is monitored and, in certain designated airspaces, dictated by the National Air Traffic Service (NATS) or air traffic controllers. The operators have access to conventional air traffic control radar and Secondary Surveillance

Table 5.2: BBC National Transmitter parameters. Frequency in MHz. Information taken from [68, 69]

	Transmitter	Radio 1	Radio 2	Radio 3	Radio 4	Pol	Max ERP
1	**Oxford**	99.1	89.5	91.7	93.9	M	46kW
2	Basingstoke	99.7	90.1	92.3	94.5	V	200W
3	Blunsdon	98.6	89	91.2	93.4	V	200W
4	Cirencester Town	97.7	88.1	90.3	92.5	V	10W
5	Marlborough	99.7	90.1	92.3	94.5	V	100W
6	Membury	98.4	88.9	91.1	93.3	V	125W
7	Newbury	97.8	88.2	90.4	92.6	V	100W
8	**Rowridge**	98.2	88.5	90.7	92.9	M	250kW
9	Salisbury	99.4	89.8	92	94.2	V	20W
10	Ventnor	99	89.4	91.7	93.8	M	48W
11	Weymouth	99.6	90	92.2	94.4	V	130W
12	**Manningtree**	97.7	88.1	90.3	92.5	M	5kW
13	**Wrotham**	-	89.1	91.3	93.5	M	250kW
14	**Wrotham**	98.8	-	-	-	M	125kW
15	Bexhill	99.2	88.2	92.2	94.6	V	100W
16	Brighton (Whitehawk Hill)	99.7	90.1	92.3	94.5	M	600W
17	Caterham	99.3	89.7	91.9	94.1	V	15W
18	Crystal Palace	98.5	88.8	91	93.2	V	4kW
19	Folkestone	98.3	88.4	90.6	93.1	V	100W
20	Guildford	97.7	88.1	90.3	92.5	M	3kW
21	Hastings	97.7	89.6	91.8	94.2	M	500W
22	Hemdean (Reading)	99.4	89.8	92	94.2	V	1kW
23	High Wycombe	99.6	90	92.2	94.4	M	50W
24	Kenley	98	88.4	90.6	92.8	V	25W
25	Mickleham	99.3	89.7	91.9	94.1	V	25W
26	Newhaven	99.3	89.7	91.9	94.1	M	100W
27	**Swingate**	99.5	90	92.4	94.4	M	11kW

	BBC London	BBC Surrey	BBC Sussex	BBC Kent	BBC Essex	BBC Berkshire	Radio Solent	Pol	Max ERP
1	Crystal Palace	94.90	-	-	-	-	-	M	4kW
2	Guildford	-	104.60	-	-	-	-	M	3kW
3	Reigate	-	104.00	-	-	-	-	M	3.8kW
4	Brighton (Whitehawk Hill)	-	-	95.30	-	-	-	M	1.2kW
5	Chichester (Burton Down)	-	-	104.80	-	-	-	V	2kW
6	Heathfield	-	-	104.50	-	-	-	M	10kW
7	Horsham	-	-	95.10	-	-	-	M	40W
8	Newhaven	-	-	95.00	-	-	-	M	100W
9	Folkestone	-	-	-	97.60	-	-	V	100W
10	Swingate	-	-	-	104.20	-	-	M	10kW
11	Wrotham	-	-	-	96.70	-	-	M	8.7kW
12	Great Braxted	-	-	-	-	103.50	-	M	12kW
13	South Benfleet	-	-	-	-	95.30	-	M	1.2kW
14	Hannington	-	-	-	-	-	104.10	M	3kW
15	Henley	-	-	-	-	-	94.60	M	250W
16	Reading (Fountain House)	-	-	-	-	-	104.40	M	1kW
17	Windsor	-	-	-	-	-	95.40	V	500W
1	Rowridge	-	-	-	-	-	-	96.10	M	10kW
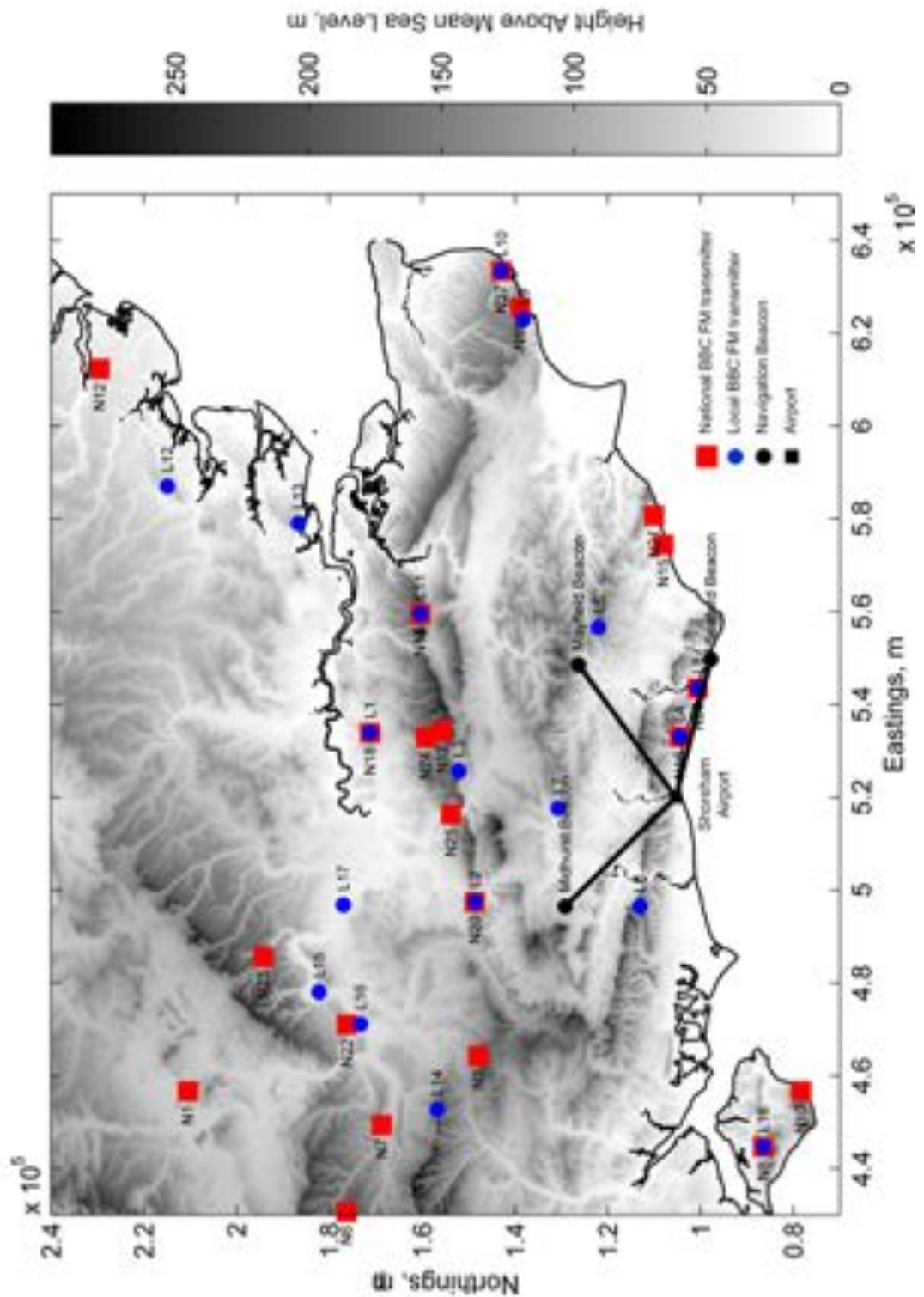
Figure 5.4: Map of local and national BBC FM transmitters. The navigation beacons and Shoreham airport have been added to give the scale. The background image is a digital elevation map of the UK, in metres above mean sea level.

Radar (SSR) to locate aircraft throughout the UK. Mode-S/ADS-B SSR transponders aboard aircraft send regular location and velocity updates to the receiving ground stations, along with a unique aircraft identifier. These location updates are unencrypted so can be intercepted using a commercial Mode-S/ADS-B receiver. To understand the air picture in the experimental scenario therefore, a USB powered Mode-S/ADS-B receiver[1] was used to collect air truth information. The Kinetics Avionics SBS-1 system logs the updates from all aircraft in the receiving antenna's field of view and 120 mins of data was collected, shown in the Cartesian plane in Figure 5.5a and as an altitude profile in Figure 5.5b.

The dense nature of the airspace means that a diverse range of target scenarios are encompassed, from low altitude low speed aircraft during take-off and landing, low to medium level target manouvering during holding patterns and high altitude high speed targets transiting through the airspace. The following specific metrics have been ascertained from the data:

- **Typical ascent/descent rate** A visual inspection of Figure 5.5b shows that the ascent and descent rates for these commercial aircraft remain uniform as neighbouring altitude profiles are parallel to each other. Analysis of a reduced sample set shows a typical rate-of-climb and rate-of-descent of between 5 and 10 m/s (900 to 1800 feet/minute).

- **Number of take-offs/landings per hour** The Mode S/ADS-B receiver loses line of sight to aircraft landing at Heathrow once the aircraft's altitude drops below around 500 m. Over the two hour period, Gatwick airport had a throughput (an aircraft taking off or landing) of 38 aircraft an hour and Heathrow double that as it has two runways.

- **Altitude distribution** In Figure 5.6b it can be seen that there is a high altitude region (9,000 m to 12,000 m) where aircraft tend to stay at fixed flight levels, an intermediate zone (4,000 m to 9,000 m) through which aircraft ascend or descend, and a low altitude zone where aircraft either enter a holding pattern or manoeuvre for approach or following departure. The distribution of aircraft altitudes is shown in Figure 5.6.

- **Aircraft speed** The distribution of aircraft air speed is shown in Figure 5.7. To prevent range-walk during a CPI, the integration time needs to be chosen so that the

---

[1]http://www.kinetic-avionics.com/sbs-1.php
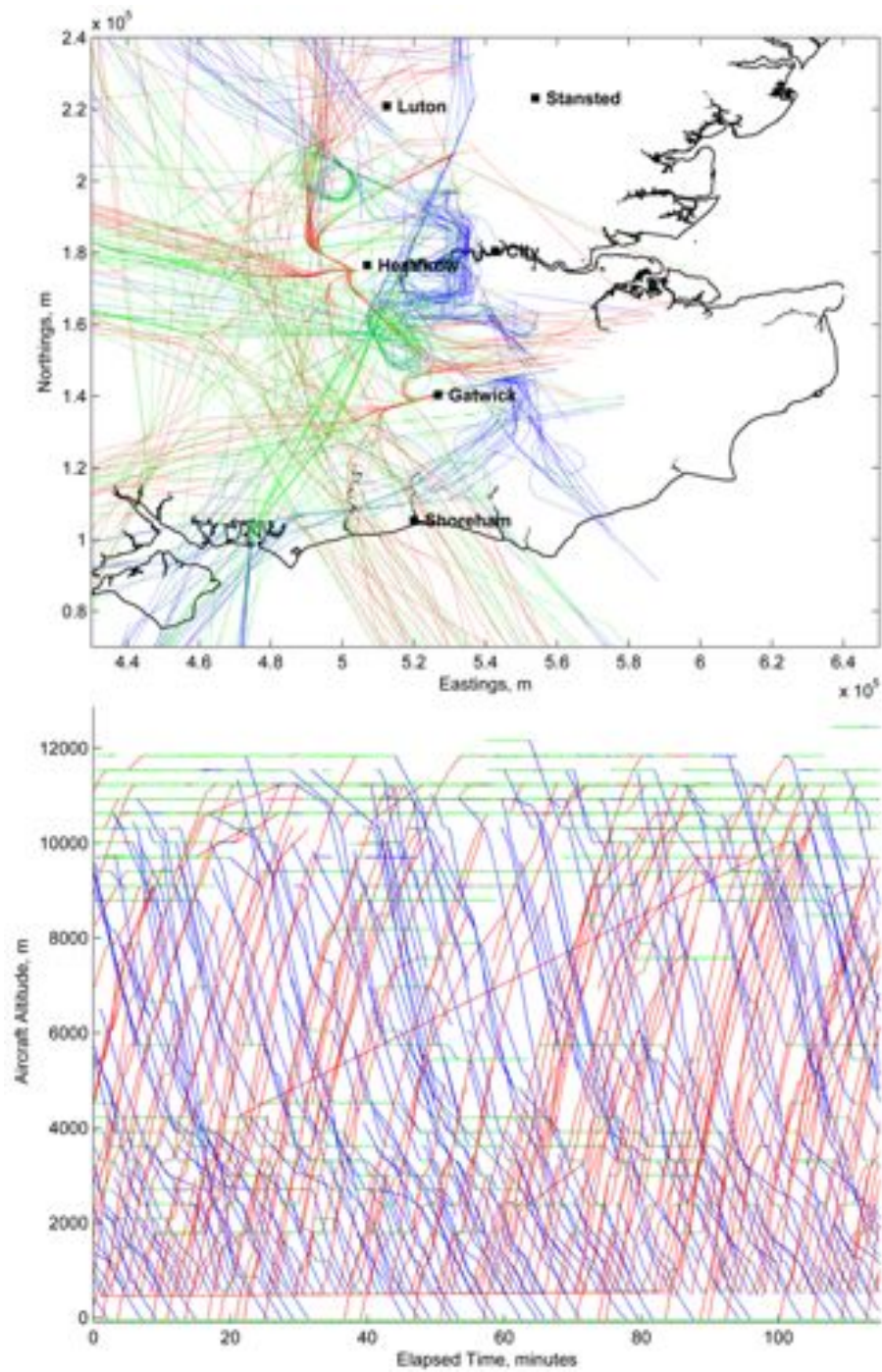
Figure 5.5: 2 hours of air truth recorded near Gatwick Airport with the updates shown in a) Cartesian plane and b) altitude profile. Red lines indicate ascent, green lines indicate level flight and blues lines indicate descent.
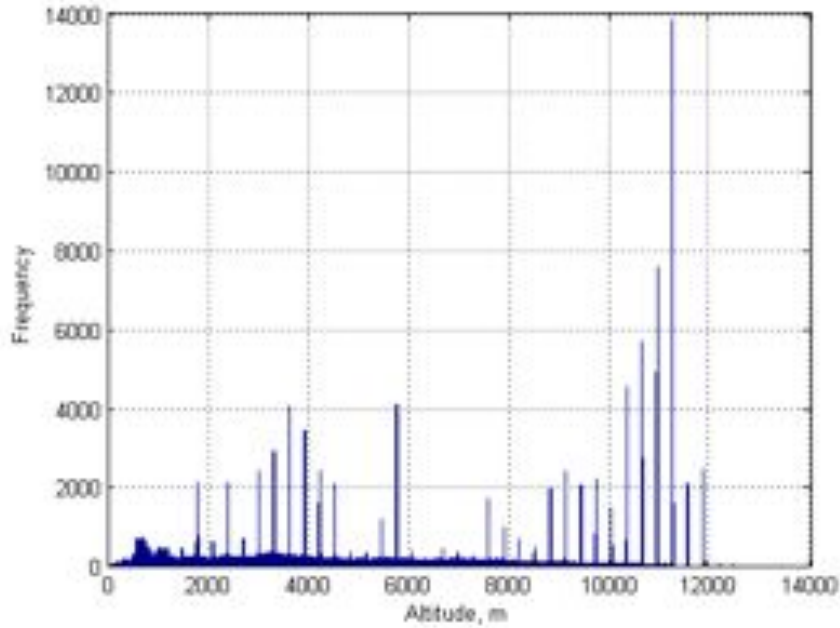
Figure 5.6: Distribution of aircraft altitudes from recorded air truth data.

resultant receiver-to-target range does not change more than half a range bin during the CPI. The maximum airspeed of the aircraft is around 300 m/s. Worst case the target and receiver will be moving directly towards each other or directly away from each other. With the receiver moving at its maximum speed of 60 m/s and the target at 300 m/s, and assuming a best-case range resolution of 1.5 km, then the maximum CPI is 2 s. An integration time of 2 s should ensure that the target can be considered to be stationary throughout the CPI.

- **Aircraft acceleration** The aircraft radial acceleration will determine the maximum integration time that can be used. The longer the integration time, the higher the target SNR. If however there is a relative radial acceleration between the receiver and the target, the Doppler response may span more than one bin. This Doppler-walk is analogous to the range walk in the time domain. Using Equation 2.18, an integration time of 1 s would give a Doppler resolution of 1 Hz and a maximum target radial acceleration of 1.5 ms^{-2} . The acceleration characteristics of most aircraft would mean that their responses would be substantially contained within a 1 Hz Doppler bin.

Although this is only a sample of aircraft air truth, it is taken to be representative of the typical air activity one might encounter.
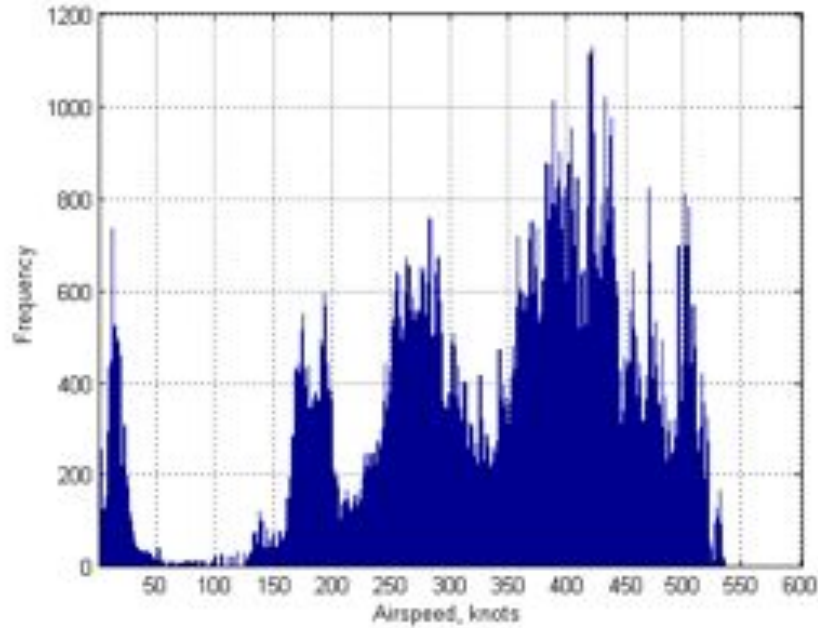
Figure 5.7: Distribution of aircraft airspeed from recorded air truth data.

5.3 Experiments

The hardware described in the previous chapter was subjected to several confirmatory ground based tests prior to the airborne experimental campaign. This section details the two airborne experiments that took place using this system. The experimental set up and flightpaths are described along with any other pertinent information.

5.3.1 Airborne Experiment 1

The first experimental data collection was conducted on the morning of 18th March 2010. The collection was split into two parts: ground-based and airborne. The ground-based collection was to ensure that the receiver operated without interfering with any of the aircraft's systems. Equally it was important to ensure that the aircraft's Mode-S/ADS-B beacon and VHF communication systems did not interfere with the demonstrator system. The receiver was installed in the aircraft and initially, with the engine off, the system was tested. The installation of the antennas is shown in Figure 5.8. Once content that the system was working as desired, the engine was started and the tests repeated. Again, no unforeseen effects were noted therefore the experiment could progress to the airborne data collection.

The aircraft took off from Shoreham airport and proceeded towards Mayfield Beacon. A handheld GPS receiver was used to log the flight path, shown in Figure 5.9. The reception

Figure 5.8: System installation in the PA 28-181.
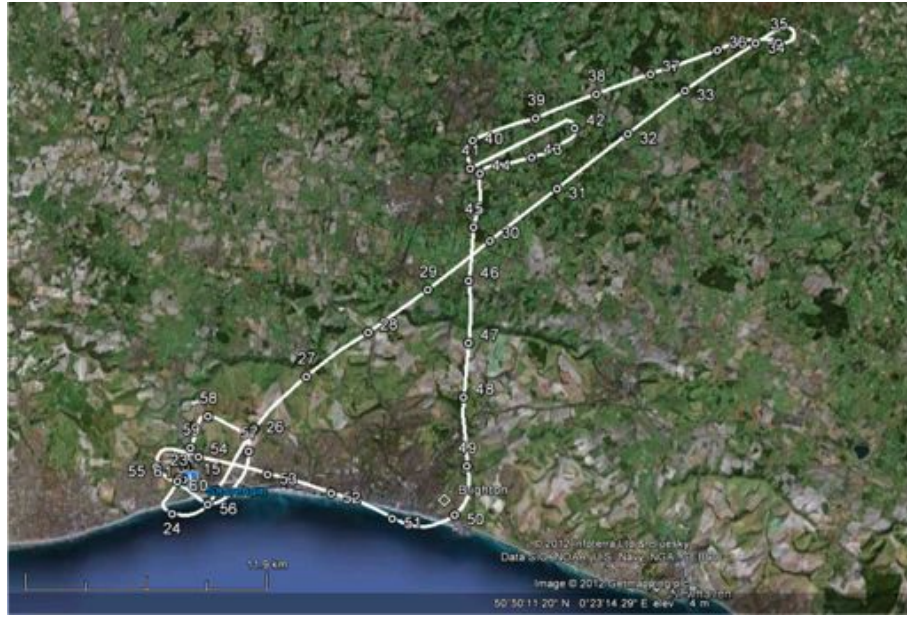
Figure 5.9: Flightpath for the first airborne experiment. The elapsed time, in minutes, is shown every minute of the flight.

of the GPS signal was found to be adequate however the track was lost momentarily during a turning manoeuvre. The blue crosses on the receiver flight path denote the estimated position of the aircraft at the start of a data capture. The position of the aircraft is estimated using linear interpolation, since the GPS updates every 8 to 13 s compared to a data capture every 2 s. The heading, altitude and speed of the receiver during the flight are shown in Figure 3.

Two channels were used from the Wrotham transmitter, Radio 1 at 98.8 MHz and Radio 2 at 89.1 MHz. Radio 1 was the preferred station since the modulation bandwidth is generally larger, leading to improved range resolution, however the received power tended to be lower than for Radio 2. During the flight the system made 589 captures at varying intervals, producing 10 GB of data.

Figure 5.10: Flightpath for the second airborne experiment. The elapsed time, in minutes, is shown every minute of the flight.

5.3.2 Airborne Experiment 2

The aim of the second airborne experiment was to integrate a series of platform manoeuvres including high altitude flight and rate one and two turns and to match the target detections to the air truth by comparing them to the data collected concurrently by the Mode-S/ADS-B receiver. The second airborne experiment was performed on the morning of 20th July 2010 and the flightpath as recorded by the GPS, is shown in Figure 5.10. The system was installed in the way as for the first experiment. Key parts from the experimental log are tabulated in Table 5.3. The integration time was increased to 3 s to give improved performance for the clutter analysis work.

5.4 Initial Processing

Prior to analysing the data for targets and clutter, a standard downconversion and filtering procedure was applied. This offline processing, outlined in Figure 5.11, consists of normalising the raw ADC output to the full scale voltage value, filtering and then mixing down to baseband. The baseband signal is then low pass filtered and downsampled to 200 kHz.

The reference and surveillance 200 kHz baseband signals are then ready for target and clutter processing.

Table 5.3: Summary of key parts from the second experimental log.

Ref	Start File	Stop File	Comments	Illuminator 1	Illuminator 2	Integration Time, s
1	1	20	Take off and left turn	Manual	-	2
2	21	56	Intersection to Mayfield on 260° radial	Wrotham R2	Varying	2
3	57	78	Rate 1 turn to right at Mayfield beacon	Wrotham R2	Oxford R2	2
4	79	82	Sharp right turn back on to 260° radial	Wrotham R2	Varying	2
5	91	99	Loss of GPS signal,generally heading towards Mayfield	Manual	-	2
6	100	134	To intersection on bearing of 260°	Manual	Varying	2
7	135	148	460° turn to left	Manual	-	2
8	149	182	Ascent to 5000 feet	Manual	-	2
9	184	191	Descent	Manual	-	2
10	195	206	Left turn	Manual	-	3
11	207	230	Descent prior to landing	Manual	-	3
12	231	237	Landing	Manual	-	3
13	1a	7a	Taxiing	Manual	-	3
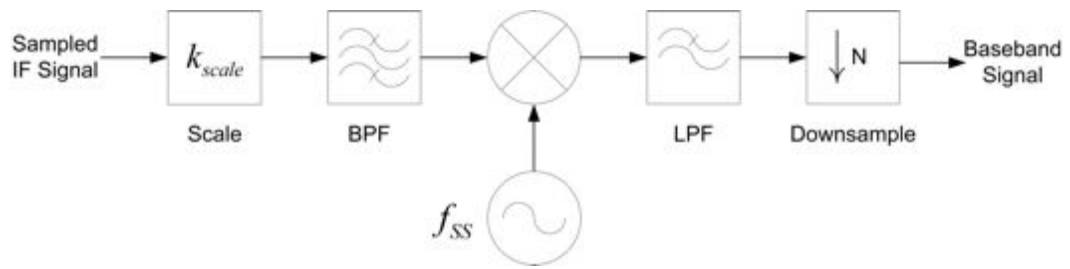
Figure 5.11: Matlab offline processing block diagram

5.5 Summary and Conclusion

This chapter has described the experimental scenario and equipment used to obtain air target and clutter data using a passive FM system. The airborne platform, FM illuminators and target environment in the vicinity of Shoreham airport have been described and discussed. Analysis of air traffic movements within the surveillance area fed into the design of the flight paths in order to maximise the probability of detection of air targets during the experimental data collection flights.

The analysis of the air target behaviour has shown that an integration time of 1 s is a good compromise between achieving a high Doppler resolution and preventing target range and Doppler walk within the integration period.

The two airborne experiments were described and the initial offline processing discussed. Having collected the high quality experimental data, the analysis of air target and clutter is discussed in Chapters 6 and 7 respectively.

Chapter 6

Aircraft Detection

6.1 Introduction

In the previous chapters, a simulation of the airborne scenario has been developed and used to inform the design of the RF receiver hardware. An analysis of the airborne scenario identified favourable experimental flight paths and the experiments were flown using a geometry that would give the highest probability of air target detection.

This chapter details the processing and analysis of the experimentally collected data in three evolutions: firstly, a static ground based scenario is used to confirm the correct RF and software processing parameters. Secondly, a flight experiment is used to confirm that the system operates in isolation from the host aircraft's navigation and safety critical systems and to ensure the signal levels are as expected. Finally, a second flight experiment is flown which builds on the lessons learned from the first two experiments in order to successfully achieve the aim of detecting airborne commercial airliners using an airborne passive bistatic radar system.

In order to streamline the narrative, the chapter begins with an explanation of the processing scheme employed, which is common to all the flights following experimental trials. The results of the processing from the three experiments are then discussed and the chapter concludes with a summary of the air target detection analysis.

6.2 Target Detection Processing

The basic flow of processing for target detection is shown in Figure 6.1 and each part is now developed and explained in sequence. In order to be able to detect targets, the direct signal power in the surveillance channel has to be reduced in order to remove the impact
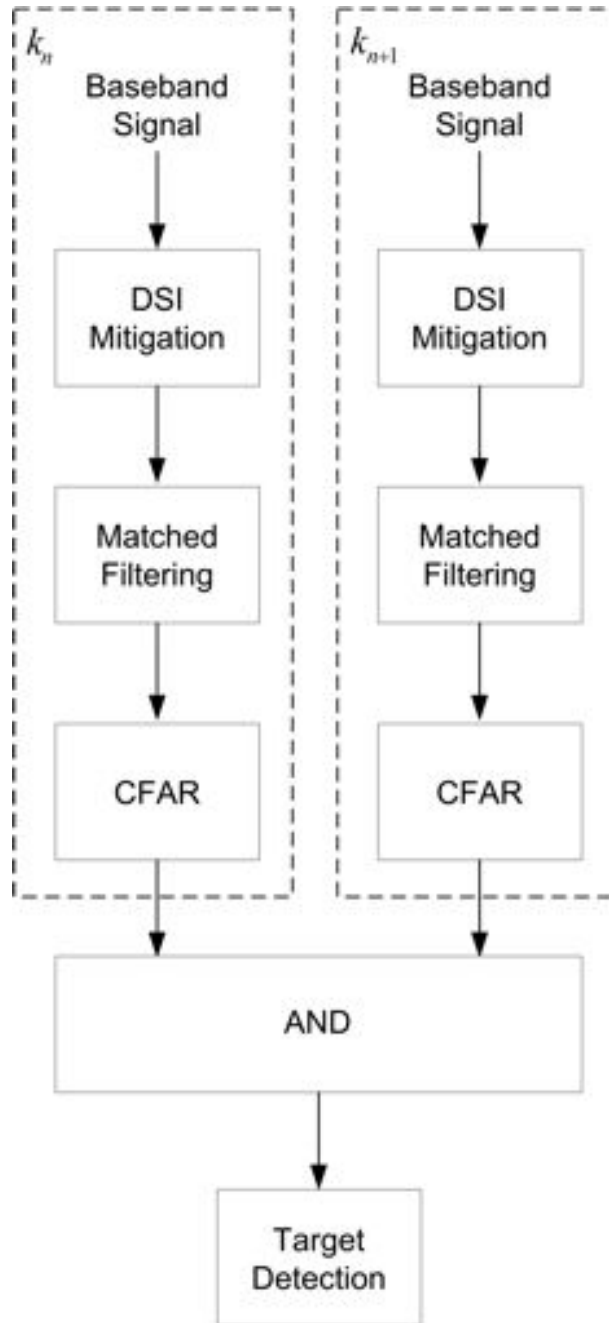
Figure 6.1: Target detection processing overview. In sequential pairs, two 1 second looks are processed and the output correlated. The output of the correlated pairs are declared as detections.

of the correlation sidelobes of the direct signal, on the low SNR targets. The SNR is then maximised by using a matched filtering approach as described in Chapter 2. A CFAR processor is then used to detect a target within a look. Looks are then correlated in pairs in order to give a 2/2 detection logic and achieve a useful probability of detection.

As outlined in the previous chapter, during the flight, the receiver was commanded to tune to the first transmitter, capture 2 seconds of continuous data, then tune to the second transmitter and capturing a further 2 seconds of data. This was repeated every 15 seconds with the data being saved to laptop disc between captures. The location and velocity information of the receiver, necessary for the processing, was logged using a handheld GPS receiver. The ADS-B/Mode-S receiver and laptop clock were manually synchronised with the GPS time from the handheld receiver.

6.2.1 Baseband Signal

The following processing assumes a perfect copy of the reference signal. In many applications it is possible to tap off a copy of the transmitted signal from the source, or for digital signals, reconstruct the original signal with a very low bit error rate. For FM PBR systems, the transmitted signal is not known and can not be tapped off from the source. The reference signal at the receiver will contain multipath and this will affect the level of the cancellation available from the DSI mitigation stage and also introduce sidelobe noise in the ARD surface.

Blind adaptive equalisation techniques such as the Constant Modulus Algorithm (CMA) may be used to reduce the impact of multipath propagation on the reference channel prior to DSI cancellation and matched filtering. It is not investigated further in this work as it is an established technique and for best performance, requires multiple receive elements to perform Space-Time CMA (ST-CMA) on a multiple channel receive system. A thorough analysis for the static case is presented in [71, 72, 73] and is not discussed further in this work.

Since there is no equalisation applied to the reference signal from the demonstrator system the noise floor of the range-Doppler surface will be increased and therefore the SNR of targets that are detected will be reduced.

6.2.2 DSI Mitigation

The Extensive Cancellation Algorithm [17, 74] was used to cancel the DSI in the surveillance channel using the reference channel signal. This algorithm has been extensively applied in the literature and in the ground based FM demonstrator at UCL [74] and has been shown to be a robust and effective method of reducing the DSI on the surveillance channel. CLEAN based algorithms [75] are also a popular approach to DSI cancellation however they will not be discussed in this work.

The adaptive filter removes the zero-Doppler component of the direct signal interference (DSI). For a moving platform the clutter is no longer in the zero-Doppler bin, however the DSI and the multipath of the DSI are in the zero-Doppler bin and their level is many orders of magnitude larger than the clutter. This approach is valid therefore since the DSI has to be removed prior to attempting any further processing. The ECA gave on average a very useful 25 dB of cancellation of the DSI. This was adequate for the bistatic geometries employed and for the dynamic range of the receivers. A demonstration of the performance of the DSI filter is given in Figure **??**. The filter has cancelled the first 50 km of bistatic range in the zero-Doppler dimension and reduced the overall impact of the direct signal sidelobes.
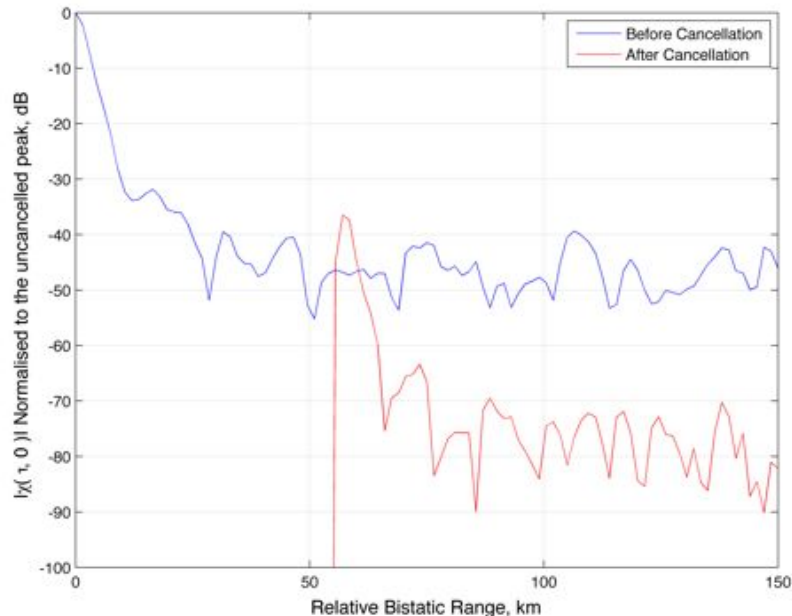

Figure 6.2: An example of the Direct Signal Interference suppression adaptive filter before and after application on an FM waveform.

6.2.3 Matched Filtering

The Doppler shifted return from a target is a function of the sum of the target's velocity and the receiver's velocity, resolved along the bisector of the angle between the transmit and receive signal paths (the so-called bistatic bisector). For the Doppler seen after the matched filter, the Doppler due to the motion of the receiver towards the transmitter will be subtracted from this value. For the fastest targets, the range of Doppler shifts lies between ± 250 Hz of the direct signal Doppler shift. Simulation has shown that a relative bistatic range of up to 150 km will maximise the utility of the system in terms of the spatial extent of the available targets in this London airport centred scenario.

With the baseband sampling frequency set to 200 kHz, a range bin equates to 5 μs and hence a differential range of 1.5 km relative to the baseline length. In order to evaluate the range response over the interval of $0 \leq R_B \leq 150km$, $N_\tau = 101$. Additionally in order to achieve a 1 Hz Doppler resolution, the entire 1 s of contiguous samples are required and hence the number of frequency bins is $N_f = 501$. Since $N_f > N_\tau$ a correlation based approach in the frequency domain requires less computation than a direct FFT based approach [72].

In order to maximise the SNR of the target detections, a correlation FFT approach was used. The correlation FFT approach is the optimal approach in terms of maximising the time-bandwidth product however it is also the most computationally expensive in terms of implementation. This approach uses the full integration time to achieve a fine Doppler resolution of 1 Hz. As discussed in [72], the correlation FFT implementation calculates the absolute squared value of the cross-correlation, $\chi[l, m]$, for a given range, l, and Doppler, m, as described by Equation 6.1.

$$\chi[l, m] = |\sum_{n=0}^{N-1} s_m[n] \cdot s_{ref}^*[n - l]|^2 \tag{6.1}$$

Where s_{ref} is the reference channel and s_m is described by Equation 6.2.

$$s_m[n] = s_{surv} e^{-j2\pi mn/N} \tag{6.2}$$

Where the symbols are described in the following list:

- N total number of time samples corresponding to the integration time, typically $N = \tau_{int} f_s = 200,000$

- m is the Doppler bin of interest in the range $-f_B \leq m \leq f_B$ in N_f steps

- n time sample number, existing in the range $0 \leq n \leq N - 1$

- l is the delay of interest corresponding to the differential range of interest in the range $0 \leq l \leq N_\tau$

By carrying out the cross-correlation in the frequency domain, the DFT of $s_m[n]$, $S_m[k]$, is simply obtained through a circular shift of the samples of $S_{surv}[k]$ therefore the DFT's of the reference and surveillance are only required to be calculated once at the start of the calculation and only an inverse DFT is required for each frequency bin. This algorithm is optimised by parallelising the calculation over the Doppler dimension. Using Matlab and a multi-core processor, the Matlab Parallel Processing Toolbox was used to process the Amplitude Range Doppler (ARD) surface, Equation 6.1, using two cores and hence the overall computation time was reduced to less than 10 seconds for a full range-Doppler surface calculation.

6.2.4   CFAR

A 2D Cell-Average Constant False Alarm Rate (CA-CFAR) detection routine was applied to give a constant number of false alarms over all the frames. The diagram in Figure 6.3 shows the construction of the CFAR window incorporating guard cells around the cell under test. The cell under test is surrounded by N_{fG} guard cells in Doppler bins and N_{RG} guard cells in range. The averaging cells extend from the guard cells to N_{fA} and N_{RA} in Doppler and range cells respectively. The training window, $S[R_B, f_B]$ is the mean average of the surrounding cell values not including the cell under test or the guard cells, as shown in Equation 6.3.

$$S[R_B, f_B] = \frac{\sum_{l=R_B-N_{RA}}^{R_B+N_{RA}} \sum_{m=f_B-N_{fA}}^{f_B+N_{fA}} \chi[l,m] - \sum_{l=R_B-N_{RG}}^{R_B+N_{RG}} \sum_{m=f_B-N_{fG}}^{f_B+N_{fG}} \chi[l,m]}{N_{RA}N_{fA} - N_{RG}B_{fG}} \quad (6.3)$$

The constant false alarm rate processing is conducted by comparing the cell under test to the averaged surrounding cells, with a threshold multiplier, α, as shown in Equation 6.4. The value of α was iteratively set on a frame-by-frame basis to ensure that there were a constant number of false alarms per frame.

$$\chi[R_B, f_B] \geq \alpha S[R_B, f_B] \quad (6.4)$$
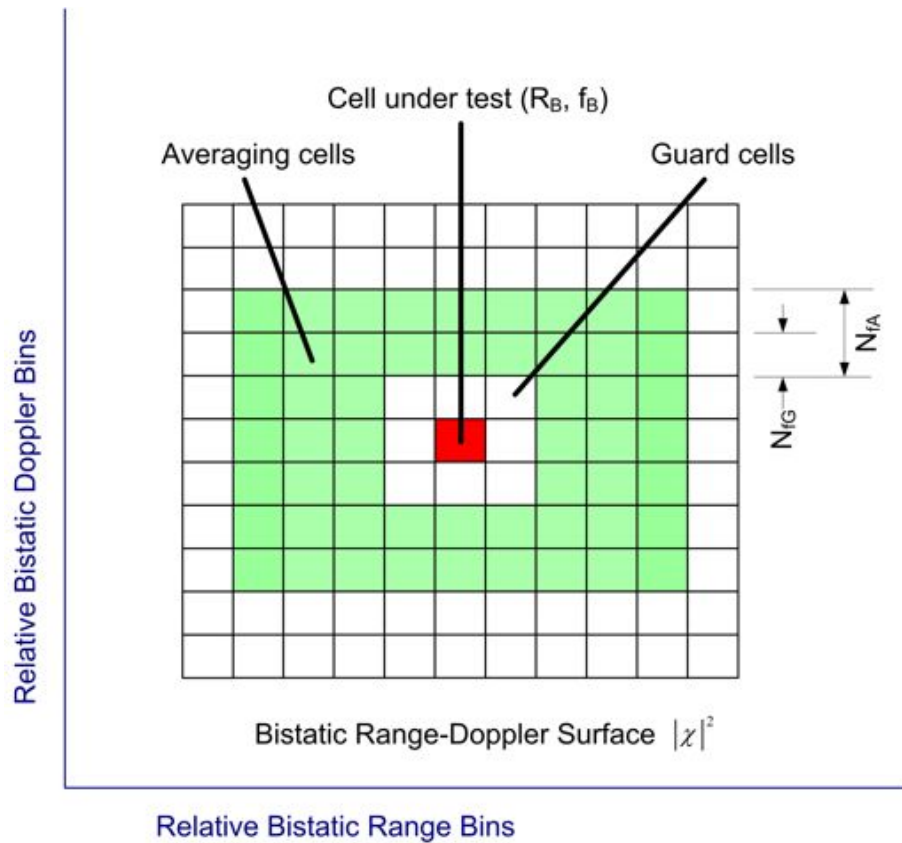
Figure 6.3: CFAR training window (green cells) construction for a given cell under test (red cell) with guard cells in range and Doppler.

The CFAR detection routine was applied to each frame to give a constant number of false alarms over all the frames with neighboring frames from the same transmitter being correlated in pairs, and responses present at the same range and Doppler in both sub-frames were declared as targets. The false alarm rate was set empirically set to the square root of the number of cells in the range-Doppler map.

6.2.5   Target Detection

A 2/2 detection logic was employed to reduce the P_{FA}. With a false alarm rate of 225 per frame, the probability of a pair of false alarms due to noise correlating on separate looks in any one cell is thus only 1.98 x 10^{-5} which is 225 times better than the probability of false alarm when using a single frame.

On the assumption that the majority of the alarms in a frame are due to noise and are therefore uncorrelated, the average rate of false alarms due to noise should be no more than one per frame. If a significant proportion of the detections at the frame level are due to targets or clutter, the false alarm rate due to noise will be lower as a result.

6.3 Experimental Results

In order to ensure that the limited amount of time spent on airborne trials were maximised, a staged approach to data collection was employed. Having ensured that the RF system was working as designed, a ground based static collection was performed. This had two aims: firstly, demonstrating that the system was indeed capable of detecting air targets and secondly to fine-tune the control software and offline data processing techniques to ensure that the flight trials would yield usable data. Once the static performance of the system was confirmed, the two airborne experiments were performed, building on the lessons learned from the previous experiments to incrementally improve the performance and useful output of the system.

6.3.1 Static Receiver Experiments

The aim of this experiment was to confirm that the hardware and the processing worked as intended. The data collected would also allow the detection scheme to be benchmarked and optimised, prior to the introduction of a moving receive platform. To simulate the manner in which the system would be installed in the aircraft, the receiver was installed on the 11th floor of the UCL Engineering building with the rod reference and surveillance antennas attached to the windows.

The demonstrator was tuned to BBC Radio 2 from Wrotham Transmitter and the reference and surveillance signals were captured in 1 second looks and saved to the laptop's hard drive. Additionally to the data acquisition, the Mode-S/ADS-B receiver recorded the air activity.

The looks were processed as detailed in Section 6.2. An example ARD surface, after direct signal cancellation, is shown in Figure 6.5. This is the raw information which is used by the target detection script and this example is a fair representation of a typical ARD surface with targets present for a static receiver. The low values at zero Doppler extending out to 75 km in range is the part that has has been removed by the direct signal suppression filter. As a consequence of this removal, two strong targets away from the origin are present, at 20 km and 50 km. With the system operating in central London, there is a large amount of man-made interference local to the receiver site and typically this manifests in the ARD surface as responses that extend over all Doppler frequencies out to a bistatic range of 20 km. This is a common feature of the all the captures and is clearly present in the 2/2 detection output of Figure 6.6.
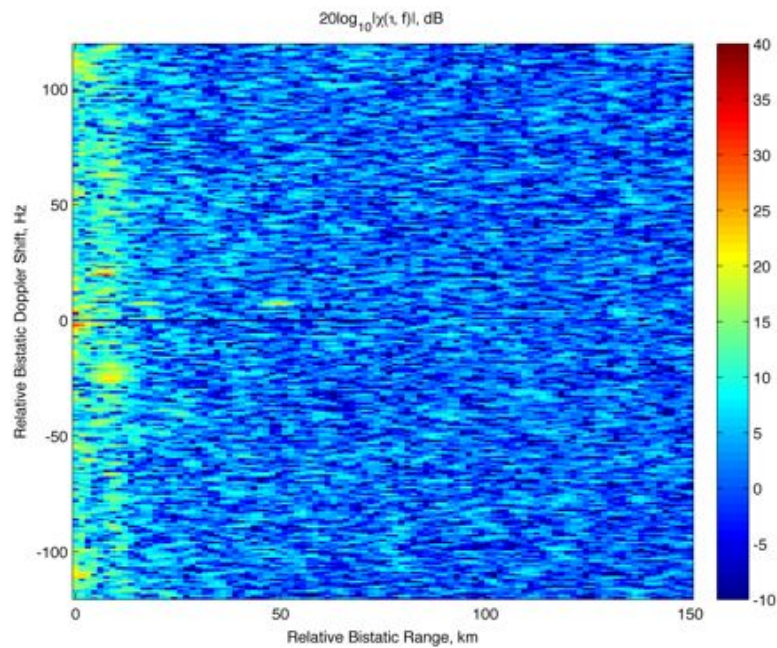
Figure 6.4: Example 1 second ARD surface after direct signal cancellation
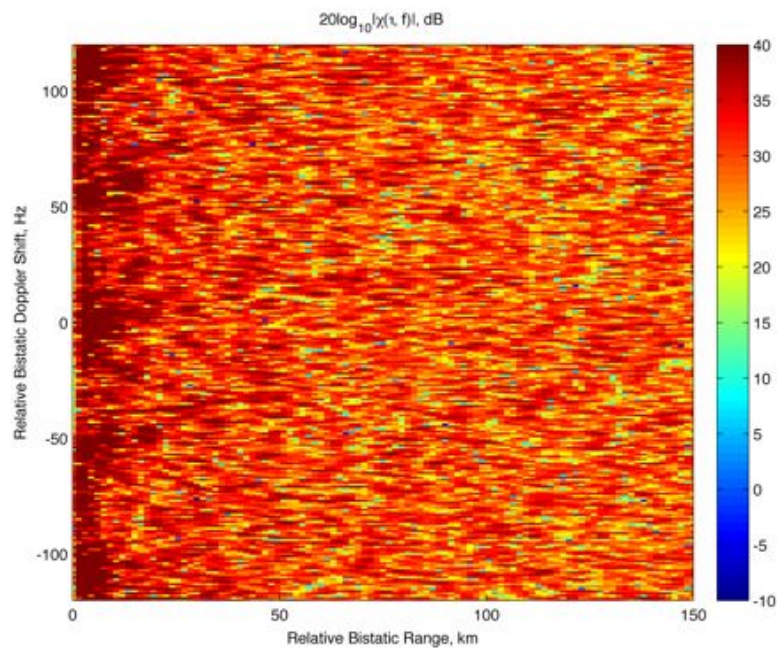
Figure 6.5: Example 1 second ARD surface after direct signal cancellation

The ARD for each capture is then processed by the detection script and the cumulative output of the 2/2 detection logic for all 22 looks is shown in Figure 6.6. Figure 6.6 shows the local interference which typically correlates over several looks. To reduce the impact of this, only targets with a bistatic range greater than 20 km will be considered for further processing. To aid in the analysis of the performance of the system, the target detections are compared with the air truth data in Figure 6.7. The first plot shows the air truth overlaid
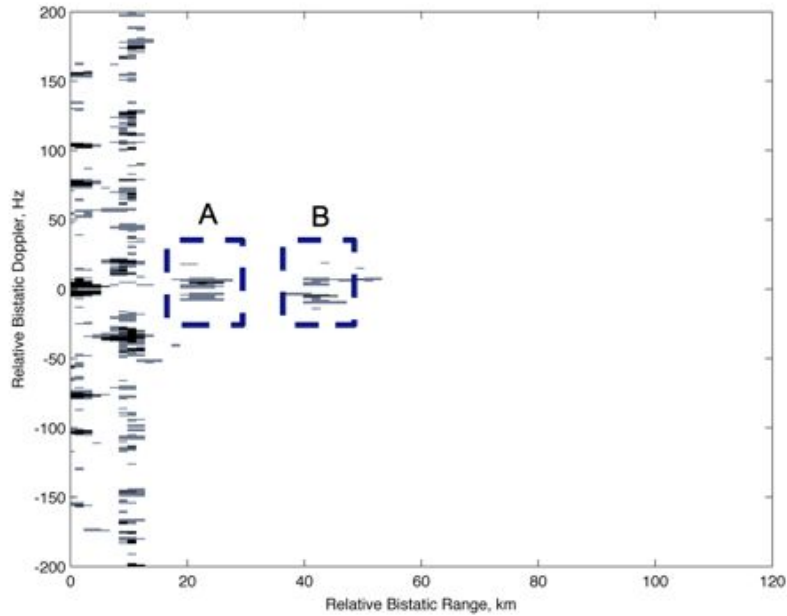
Figure 6.6: Cumulative detection surface for 22 looks of the static receiver system. The build up of responses A and B over time identifies them as likely moving targets.

on to the ARD in the bistatic plane. Here it can be seen that there is high correlation between targets A and B, and the system detections. In the second figure, the air truth has been plotted in the Cartesian plane along with the transmitter (red dot), receiver (blue dot) and contours of constant bistatic range at 10 km intervals (black ellipses centred on the transmitter and receiver). In both plots the green tracks are the targets that have been detected and the black stars show the most recent update and hence the direction of travel of the target aircraft.

To further support the likelihood that the targets have been detected, the RCS of the targets can be estimated from the SNR of the target in the ARD surface. Target A (at 20 km) has a mean SNR of 30 dB and Target B has a mean SNR of 20 dB, this equates to a bistatic RCS of 19 dB and 17 dB respectively. These values agree with the typically assumed values of the bistatic RCS for a Boeing 747 type commercial passenger aircraft. The location of the targets in this situation puts them outside of the forward scatter region, where their RCS would have been subject to forward scatter enhancement effects.

The successful operation of the receiver in this static scenario proved the correct operation of the demonstrator system and allowed the fine-tuning of the software processing routines. This allowed the airborne experiments to be performed in the knowledge that the system was operating as intended.
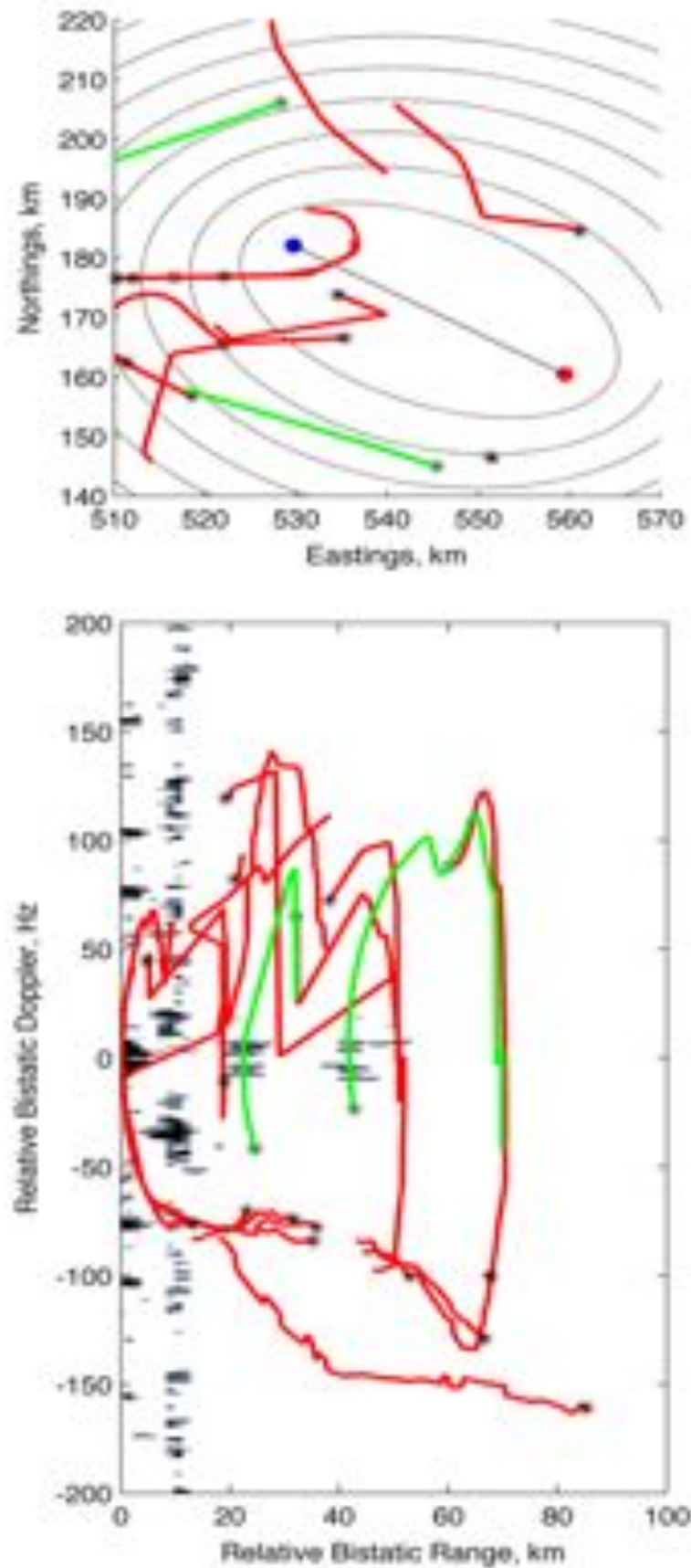
Figure 6.7: Cumulative detection surface for stationary receiver with the air truth overlaid in the bistatic range-Doppler plane and the Cartesian plane.

6.3.2 First Flight Experiments

The data was collected as described in Section 5.3.1 and processed in the same manner as the ground experiments.

A typical range-Doppler detection plot is shown in Figure 6.8. This plot shows the aggregated results over thirty seconds, along with the regions where stationary and moving ground clutter can exist. The extent of the stationary and moving ground clutter is dependent on the direction of travel of the receiver with respect to the transmitter and also on the receiver and target velocity. The maximum speed of a moving ground target was assumed to be 200 mph, corresponding to a high speed train. In the ground clutter regions, potential target detections are indistinguishable from stationary and moving ground clutter. In this
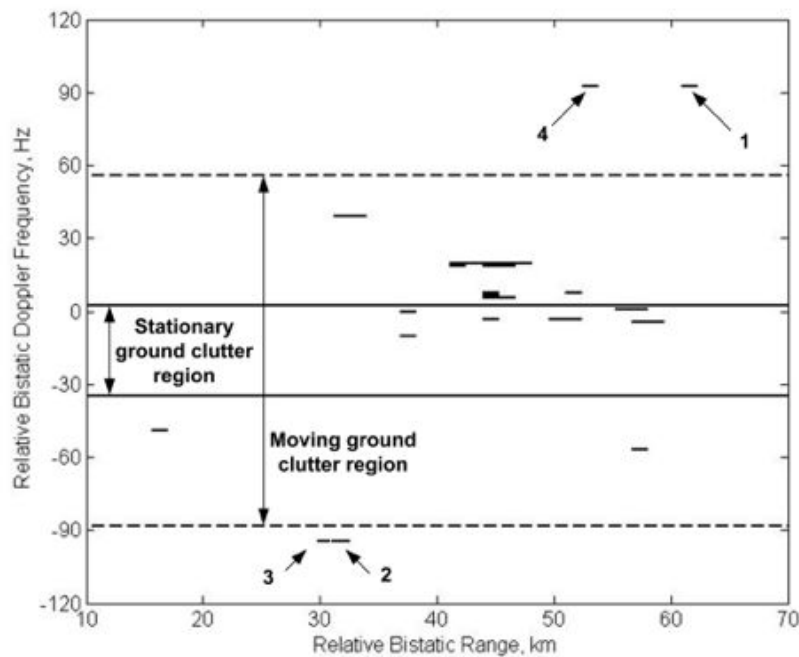
Figure 6.8: Aggregated detections for the first airborne experiment with the extent of the stationary ground clutter (solid black line) and moving ground clutter (dashed black line) indicated for reference.

preliminary experiment ground truth was not available and only one transmitter was used, so location of the returns by trilateration was not possible. In order to demonstrate that we had indeed detected air targets, after the CFAR and 2/2 detection processing, two further stages were employed as follows.

1. **Elimination of ground targets and clutter** The lines of constant Doppler in Figure 6.8 show the extreme limits of the Doppler shift for stationary clutter and for moving ground targets at any position on the ground. Detections outside this region

are therefore not due to targets or clutter on the ground. The apparent Doppler shift of the ground clutter is proportional to the receiver velocity resolved along the bistatic bisector. For stationary ground clutter the highest relative Doppler shift occurs for a clutter patch in the direction of travel of the receiver. The most negative Doppler shift occurs for clutter in the opposite direction to the receiver's direction of travel. Clutter close to the bistatic baseline has a Doppler shift of approximately zero. The experimental installation of the equipment in the aircraft meant that the antennas were placed above the wing. This may have partially shielded them from ground returns and hence have improved the signal-to-clutter ratio.

2. **Correlation with known flight paths** ADS-B/Mode-S data gathered over several days confirmed the flight paths around the region being surveyed. The density of air traffic over Southern England means that large aircraft are confined to well-defined flight paths and a relatively narrow range of speeds. This means that if the position of the target in Cartesian space is postulated then the direction of flight can be estimated , from the true air speed, which is estimated from the narrow range mandated by Air Traffic Control, and the measured Doppler shift.

Figure 6.9 therefore shows the air routes and the ellipses giving the possible positions for each of the four targets indicated in Figure 6.8. Since the platform speed, location and heading were known, the relative bistatic Doppler frequency of the target was used to calculate the component of the target's velocity that is projected onto the bistatic bisector. By assuming a typical airspeed for the target aircraft, the direction of the target's velocity vector can then be estimated. The detection contours for detected targets were plotted in the bistatic plane along with the estimated target direction of travel at all points on the constant bistatic range ellipse. At points around the ellipse the target track, as estimated from the true speed and the Doppler shift, is shown as an arrow. It can be seen that in all four cases the estimated track matches the direction of a known air route where it intersects the ellipse of possible target positions. Although we have already shown that the targets cannot be due to clutter or ground targets and are very unlikely to be due to noise, this second test confirms that they are behaving as we would expect controlled air traffic in the region to behave. The data provides further confirmation of our hypothesis in that the pairs of detections (1,4) and (2,3) can each be seen to correspond to two detections of the same aircraft at different times, a behaviour which would also be extremely unlikely if the detections were not due to air targets.
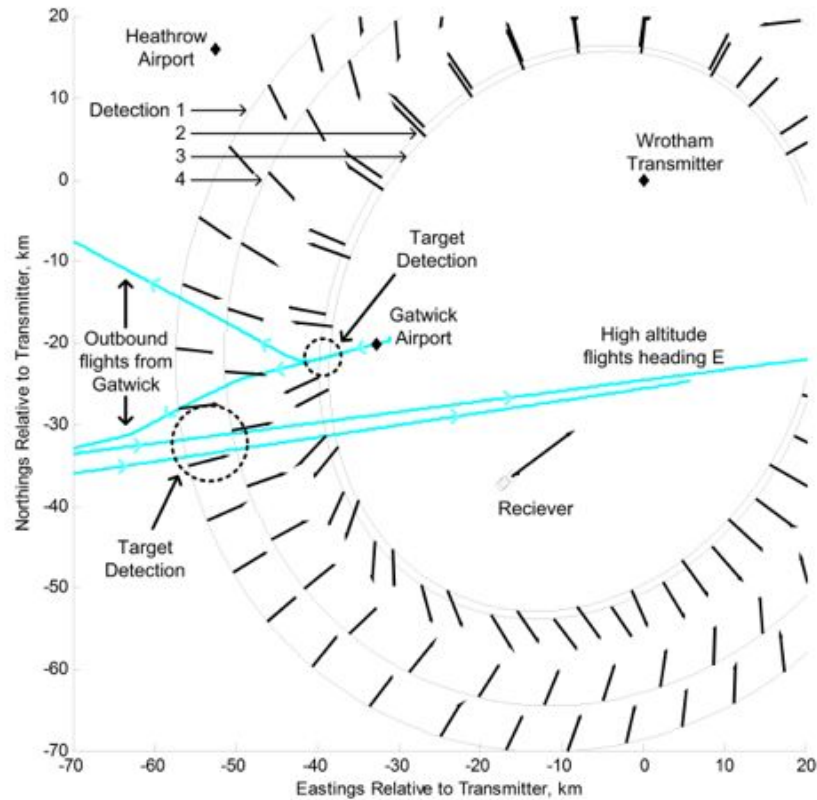
Figure 6.9: Each detection in Figure 6.8 is plotted as an ellipse of constant bistatic range. Possible target tracks, in blue, consistent with their bistatic Doppler shift and true speed, shown as arrows around ellipses. Dashed circles show regions in which it is highly likely that aircraft have been detected.

The first air experiment has confirmed that the system could operate on the host aircraft without interfering or affecting the on board safety critical systems and has confirmed that the received signal levels were as expected. Logical analysis and assumptions have demonstrated that it is highly likely that the system has detected multiple targets.

6.3.3   Second Flight Experiment

The second set of experiments were conducted in July 2010 as described in 5.3.2. In these experiments the airborne data was recorded, along with the air truth as logged by an ADS/Mode-S receiver situated on a balcony at the Thales site near Gatwick airport. The primary aim of this experiment was to demonstrate that target detections did indeed match the aircraft positions.

An example of the raw detections for BBC Radio 2 from Wrotham and Oxford transmitters are shown in Figure 6.10 and Figure 6.11 respectively. These detections are the output of the CFAR and detection logic and were captured over the same time period. The receiver was sequentially tuned to the Wrotham and Oxford transmitters throughout

the experiment in order to ensure that the dynamic range of the receiver was maximised and also to increase the composite detection volume available.   These detections were
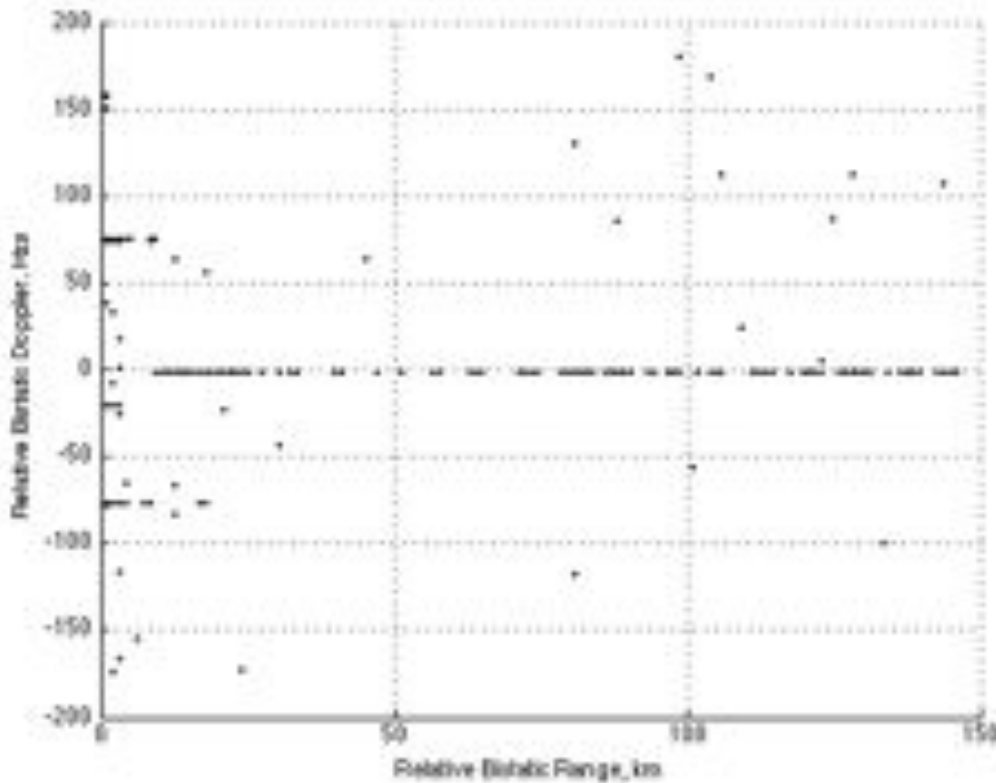
Figure 6.10: Raw detections from Wrotham transmitter

collected over 7 mins whilst the receiver was in straight and level flight, shortly after take off. The Wrotham transmitter has a lot of detections at zero-Doppler, these could be due to surface clutter or to tangential air targets. A comparison with the clutter bandwidth and air truth, allows the origins of the detection to be identified. An example of this comparison and clutter analysis is shown in Figure 6.12, obtained using the Oxford transmitter. The relative bistatic range and Doppler of two consecutive sets of detections are plotted as discrete points in the relative bistatic range-Doppler plane, the first in grey and the second, 15 seconds later, in black. To aid the comparison of the system detections with actual aircraft, 30 seconds of air target tracks recorded during the experiment are overlaid with a triangle and aircraft identification number representing the most recent update and direction of travel. Finally, the limits of Doppler shifted stationary and mobile ground clutter are shown as solid and dashed lines respectively. Four detections (A to D) have been highlighted for further discussion. The discrete points in range-Doppler space represent the center of the resolution cell which, depending on the bistatic angle, at best extends to ± 1 Hz and ± 5 km of the discrete detection point.
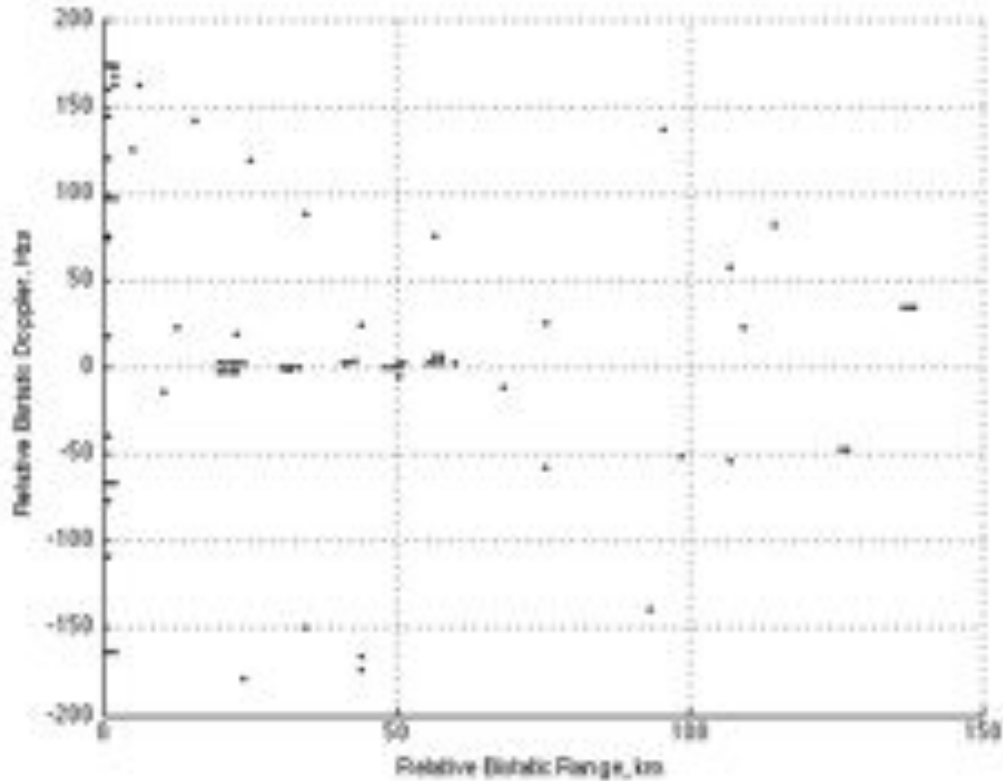
Figure 6.11: Raw detections from Oxford transmitter

The first point of note is that detections A and B clearly show that the system has detected two aircraft: detection A is of aircraft number 11 which is flight SHT17Q at an altitude of 15,500 ft and detection B is of aircraft number 33 which is flight EZY4BS, a large commercial passenger aircraft, at an altitude of 24,300 ft. The flights were identified from the air truth data.

The two detections highlighted by C demonstrate the consecutive detection of aircraft number 27 where the second detection, in black, is made 15 seconds after the first detection, in grey. Aircraft 27 is flight RYR8UJ at an altitude of 26,700 ft. In the case of D, the system has reported several detections in the zero relative bistatic Doppler bin at varying ranges. There are three aircraft that present zero Doppler which lie in the range of interest, however there is no way to determine whether the detections are of the aircraft or from the range sidelobes of the insufficiently cancelled DSI. Altering the receiver course in subsequent looks would change the relative Doppler shifts and geometry, bringing those targets out of the zero-Doppler bin and reducing the interference from the range sidelobes. Detection D also demonstrates an interesting situation since several aircraft present with bistatic ranges and Doppler shifts of the order of the system resolution, and are therefore indistinguishable from each other. In this instance, detection D could represent a detection from one, all three,
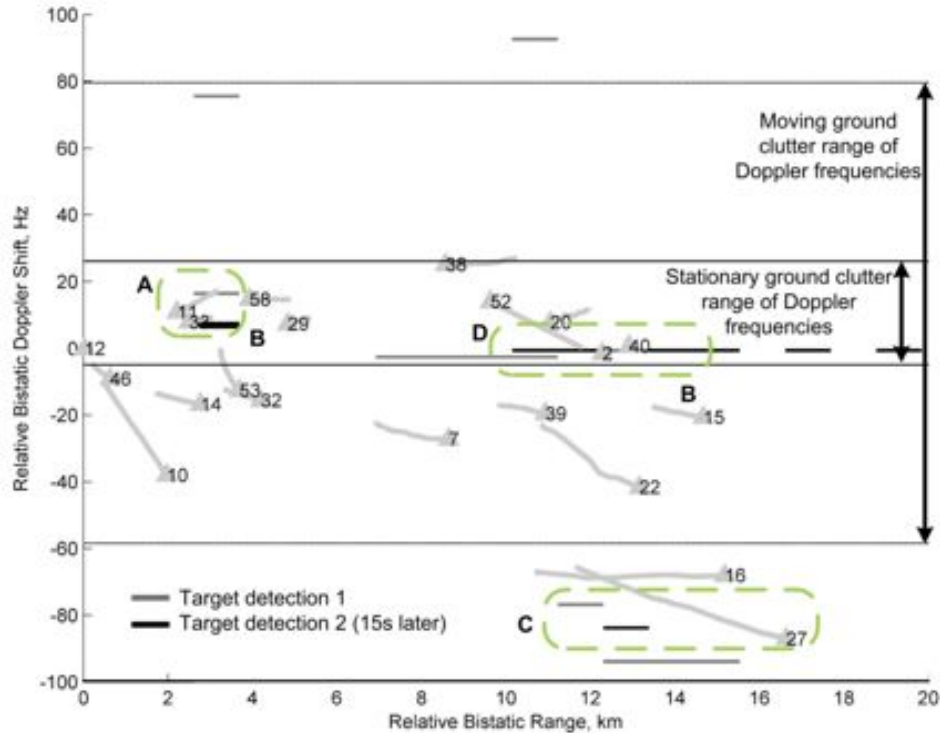
Figure 6.12: Example of target detection (grey bars followed by black bars 15 seconds later) and air truth (grey line with a triangle and target identification number on the most recent update) comparison in the bistatic plane. A and B represent two detections of two separate aircraft, C demonstrates the consecutive detection of the same target 15 seconds apart. D demonstrates the inability of the system to resolve multiple targets in a cell and the effect of insufficient DSI suppression.

or most likely, a combination of aircraft. The relatively poor modulation bandwidth and hence range resolution of FM signals, does not allow the aircraft to be uniquely resolved. The problems of multiple aircraft in a resolution cell and of targets being lost in clutter could be solved in a practical system by the combination of the spatially diversity obtained from the multiple transmitters and by using a tracker, to observe the evolution of the aircraft positions over time and follow them through the clutter. A comparison of the detections with the aircraft locations shows that there are several aircraft that have not been detected. For passive techniques in general to be incorporated into a credible sensor system, the operator needs to be able to accurately understand and predict the performance of the system in order to maximise the probability of detection of aircraft in a defined surveillance area.

6.4 Summary and Conclusions

An airborne PBR demonstrator has been designed, built and after a static ground test, deployed on two experimental flights. For the first flight experiment, clear high velocity responses away from the stationary and moving clutter horizon were identified. Analysis has shown that many of these responses match the established flight paths inbound and outbound of aircraft to and from London's Heathrow and Gatwick airports as well as high altitude targets. Detailed examination of example responses confirms, for the first time, aircraft detections from an airborne PBR platform. This result establishes the viability of airborne PBR systems for air target detection. In the second flight experiment the system detections were compared against air truth data captured simultaneously. The results show a high correlation between the detections and the air truth, demonstrating for the first time the detection of an airborne target using an airborne FM passive bistatic radar system [1, 2].

The analysis of data collected during the airborne experiments has demonstrated airborne passive radar operation, using commercial FM radio signals as illuminators of opportunity. The results have highlighted several practical techniques for improving the system performance: using multiple perspectives, optimal illuminator modulation bandwidth and multiple looks over time.

Having more than one spatial perspective on the target would have a two-fold impact on the system's performance. Firstly, the position of the target can be resolved to a more practically sized resolution cell. Secondly, having more than one transmitter would help resolve multiple targets that present as a single detection for the single transmitter case. The multi-perspective information can be achieved by using more than one spatially diverse transmitter to detect the target and by adaptively varying the path of the aircraft carrying the receiver. The latter option is only applicable to an airborne or mobile passive radar.

As discussed, the FM signals are favorable for passive bistatic radar operation due to their high transmit power and coverage, however a modulation bandwidth of tens of kHz gives a poor range resolution. Although a bistatic tracking stage has not been implemented here, it is clear that any practical implementation of the system would rely on a robust tracking filter and the fusing of multi-perspective scans in both the geometrical and frequency domains.

Chapter 7

Ground Clutter Analysis

7.1 Introduction

The mobility of an airborne platform allows the receiver to be vectored to give any desired air-to-air detection coverage and also introduces the possibility of performing ground imaging and Moving Target Indication (MTI) processing. In order to investigate the performance and limitations of an airborne PBR imaging system, the extensive data collected during the second airborne experiment was used to gain an insight into the behaviour and estimated values of bistatic clutter for an FM airborne bistatic radar system.

In this work the motion of the receiver is exploited to image the stationary ground clutter present in the experimentally collected data and a rudimentary image of the surface clutter is demonstrated. The coarse image is then used to estimate the bistatic clutter RCS. The chapter begins with a description of the processing approach to creating the surface image and the method of calculating the surface reflectivity values. The second half of the chapter looks at the results and details the conclusions that can be drawn. Neither the formation of a surface image or estimation of bistatic VHF clutter has been previously demonstrated in the open literature.

7.2 Doppler Beam Sharpening

The movement of the receive platform during the Coherent Processing Interval (CPI) gives a physical boundary to the surface area of the clutter patch. In this section, the Doppler Beam Sharpening technique is explained and demonstrated on the experimental data. During the second airborne experiment, a collection was performed with a CPI of 3 seconds, with the data being continuously sampled for the CPI before being transferred to the laptop to be

saved for offline processing. The downloading to laptop typically took 12 seconds giving a revisit rate of 4 times a minute.

7.2.1 Geometry

For a static PBR receiver, the bistatic range to the clutter patch is constant therefore the stationary clutter presents a zero-Doppler. When the receiver is moving, the clutter-to-receiver path length has a rate of change proportional to the receiver velocity and the stationary clutter is observed to have a Doppler shift. The way in which Doppler can be used to estimate bearing is modelled by assuming that the range from the transmitter to the clutter within a given range cell, R_T in Figure 7.1, remains constant over the coherent processing interval, meaning that the range walk of the clutter can be ignored. With refer-
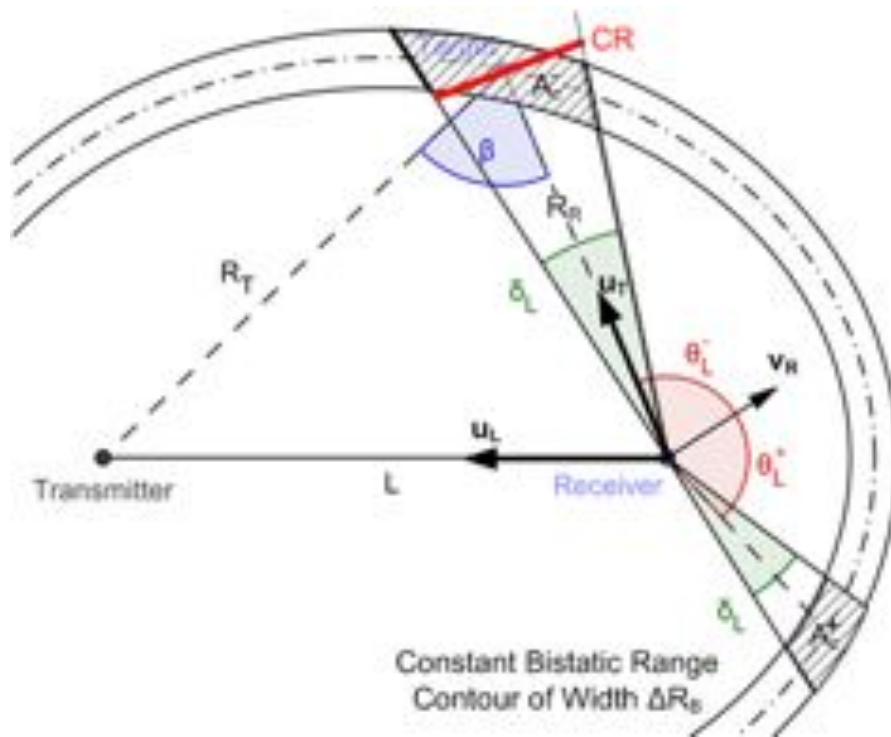
Figure 7.1: Geometry for Doppler beam sharpening derivation. The cross-range resolution, CR, is approximated as the product of the processed beamwidth, δ_L and the range from the receiver to the clutter patch, R_R.

ence to Figure 7.1, the following (three-dimensional) vectors and variables are introduced with bold symbols denoting vectors:

- $\mathbf{v_R}$ is the receiver's velocity vector

- $\mathbf{u_T}$ is the unit vector from the receiver to the centre of the target clutter cell

- $\mathbf{u_L}$ is the unit vector from the receiver to the transmitter

- R_T and R_R are the receiver-to-target and transmitter-to-target distances respectively

- L is the baseline length

- β is the bistatic angle

- δ_L is the cross-range beam width

- θ_L^+ and θ_L^- are the positive and negative look angle with respect to $\mathbf{v_R}$

- A_C^+ and A_C^- are the positive and negative clutter cell areas respectively

- ΔR_B is the bistatic range resolution

- CR is the cross-range resolution cell width at the centre of the cell

7.2.2 Bistatic Stationary Clutter

The bistatic range, R_B, is explicitly defined as in Equation 7.1.

$$R_B = R_T + R_R - L \tag{7.1}$$

This is the apparent range obtained by correlating the reference and surveillance signals in the matched filtering process of Section 6.2.3. Since it is assumed that the ground clutter is stationary, R_T is constant and therefore the rate of change of the transmitter-to-target distance is zero. The bistatic range rate is therefore defined as Equation 7.2.

$$\frac{dR_B}{dt} = \frac{dR_R}{dt} - \frac{dL}{dt} \tag{7.2}$$

The rate of change of receiver-to-target distance is the projection of the receiver's velocity vector on to the target unit vector, $\mathbf{u_T}$. Similarly, the rate of change of the baseline length is the projection of the receiver's velocity vector on to the transmitter unit vector, $\mathbf{u_L}$, as shown in Equation 7.3.

$$\frac{dR_B}{dt} = \mathbf{v_R} \cdot \mathbf{u_T} - \mathbf{v_R} \cdot \mathbf{u_L} \tag{7.3}$$

The bistatic clutter Doppler shift, f_B, therefore is calculated as Equation 7.4.

$$f_B = \frac{1}{\lambda} \left(|\mathbf{v_R}| \cos \theta_\mathbf{L} - \mathbf{v_R} \cdot \mathbf{u_L} \right) \tag{7.4}$$

Regardless of geometry, the Doppler shift of the stationary clutter is maximum in the direction of receiver travel, $\theta_L = 0°$, minimum in the opposite direction to the direction of

travel, $\theta_L = \pm 180°$, and zero in the direction of the transmitter, along the baseline. In this application, the Doppler shift of the clutter is known and the look angle corresponding to a measured Doppler shift is the quantity of interest.

Explicitly, the stationary clutter can only exist within a defined range of relative bistatic Doppler shifts, $f_{B_{MIN}} \leq f_B \leq f_{B_{MAX}}$ as defined by Equation 7.5 and Equation 7.6. Responses at Doppler frequencies outside of this range can not be due to stationary ground clutter however any motion in the ground clutter, such as vehicles or the internal motion of vegetation, may be included in this range. In order to isolate the stationary ground clutter, the clutter processing is performed on the ARD surface at Doppler frequencies within the stationary clutter Doppler limits of Equation 7.7.

$$f_{B_{MIN}} = -\frac{|\mathbf{v_R}|}{\lambda} \left(1 + \cos \theta_{TX}\right) \tag{7.5}$$

$$f_{B_{MAX}} = \frac{|\mathbf{v_R}|}{\lambda} \left(1 - \cos \theta_{TX}\right) \tag{7.6}$$

$$f_{B_{MIN}} \leq f_B \leq f_{B_{MAX}} \tag{7.7}$$

For a given θ_{TX}, the stationary clutter bandwidth, or the difference between the minimum and maximum Doppler shift, is $2|\mathbf{v_R}|/\lambda$. The faster the aircraft is travelling, the larger the Doppler bandwidth of the stationary ground clutter, however for the maximum speed of the receiver in this work, the Doppler bandwidth is of the order of 40 Hz.

The plot of Figure 7.2 shows an example of the starting product. This has been calculated as for the target detection case. The stationary clutter bandwidth associated for the receiver flight path are shown as dashed lines. The data within this bandwidth will be used to form the stationary clutter image.

7.2.3 Cartesian Projection of Stationary Clutter

The look angle, θ_L, for a given Doppler shift, f_B, is given by Equation 7.8, which has two solutions as shown in Figure 7.1 by θ_L^+ and θ_L^-. For an observed Doppler shift, the corresponding look angle is ambiguous and hence two clutter patches exist, A_C^+ and A_C^-, as shown in Figure 7.1.

$$\theta_L = \pm \cos^{-1} \left(\frac{1}{|\mathbf{v_R}|} \left(\lambda f_B + \mathbf{v_R} \cdot \mathbf{u_L}\right) \right) \tag{7.8}$$

A CPI of 3 seconds corresponds to a Doppler frequency resolution of 0.33 Hz and therefore the Doppler spread over a clutter patch will be 0.33 Hz, limiting the physical extent of
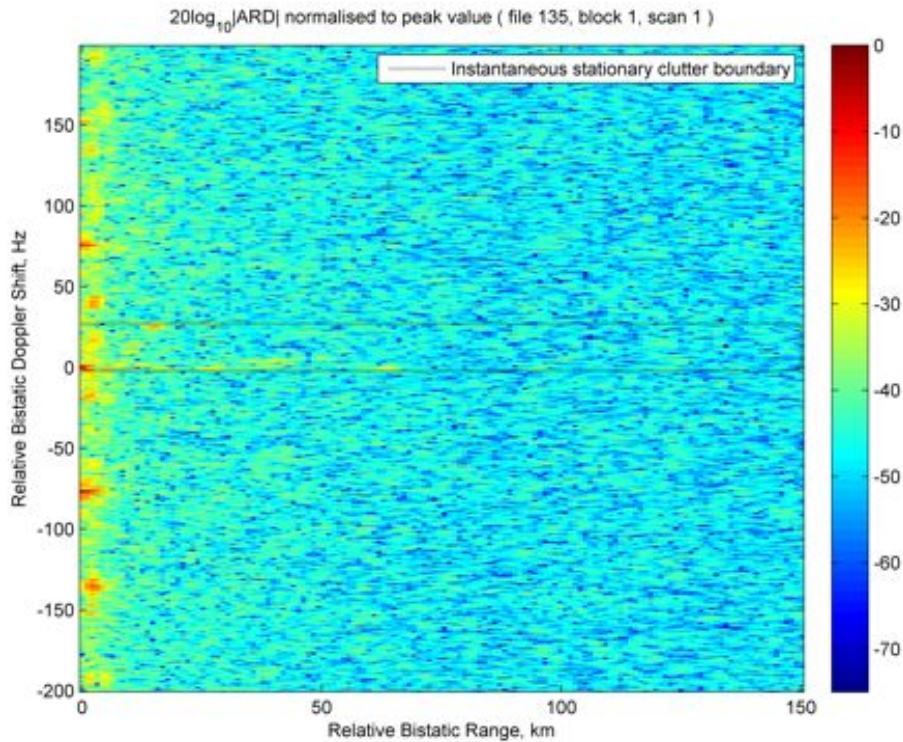
Figure 7.2: ARD surface for use with static Doppler Beam Sharpening Image Formation. The dashed black lines identify the extent of the stationary bistatic clutter in the Doppler dimension.

the clutter patch on the ground. This process is analogous to Doppler Beam Sharpening and yields a cross-range resolution improvement determined by the coherent processing interval, τ_{int}, the wavelength, the receiver velocity and the clutter look angle, as shown in Equation 7.9.

$$\delta_L = 2\sin^{-1}\left(\frac{\lambda}{2\tau_{int}|\mathbf{v_R}|\sin\theta_\mathbf{L}}\right) \tag{7.9}$$

A plot of the variation of cross-range beam width with look angle is shown for varying receiver speeds in Figure 7.3. The cross-range angle is narrowest in the direction normal to the receiver velocity at $\theta_L = \pm 90°$ and increases away from the normal. Resolution is lost in the direction of travel, $\theta_L = 0°$, and in the direction opposite to the direction of travel, $\theta_L = 0°$ and $\pm 180°$, i.e. in the same direction as it is lost in the monostatic case. For typical operating values and assuming that the clutter patch remains in the receiver beamwidth for the entire CPI, the cross-range resolution approaches $1°$, equating to 175 m at 10 km from the receiver, significantly better than the range resolution which is at best around 2 km for the single FM channels used in this work.

For a given bistatic range, R_B, the receiver-to-target range of the clutter patch, R_R, is the quantity of interest. Since the bistatic range and the desired look vector are known,
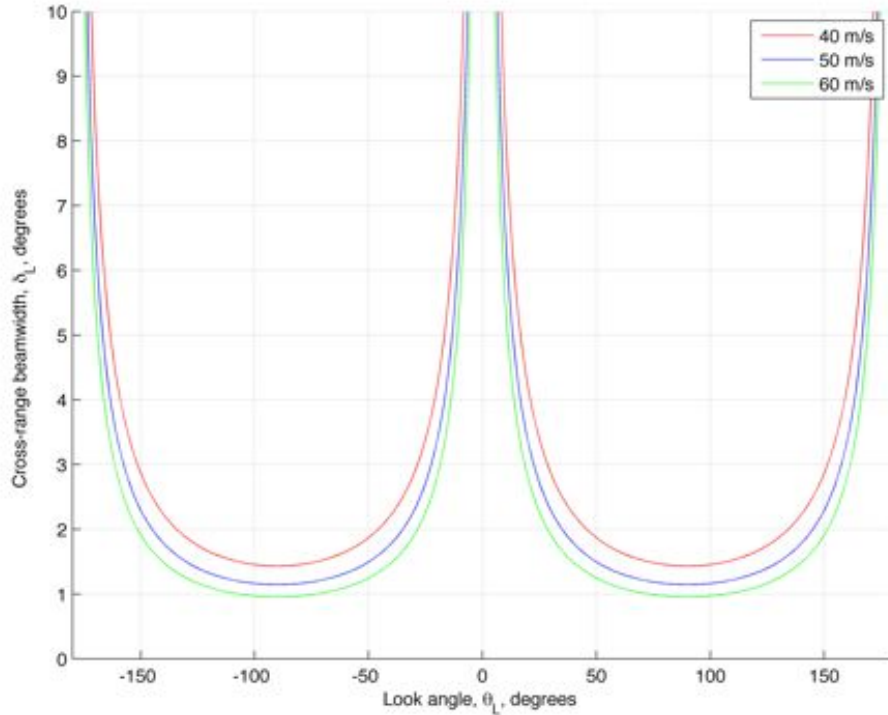
Figure 7.3: Variation in cross-range beam width with clutter look angle. The receiver speed is varied from 40 m/s to 60 m/s.

R_R is calculated using Equation 7.10.

$$R_R = \frac{R_B^2 + 2LR_B}{2\left(R_B + L(1 - \mathbf{u_T} \cdot \mathbf{u_L})\right)} \tag{7.10}$$

The look angle and receiver-to-target range can now be calculated from the range-Doppler surface and therefore, the stationary clutter can be transformed from the relative bistatic range and Doppler domain, into the more useful receiver-to-target and look angle domain. An example product of this transformation is shown in Figure 7.4. The two images correspond to there being two solutions of look angle, θ_L^+ and θ_L^-.

The receiver-to-target range allows the clutter cell area, A_C, to be approximated as a rectangle, as described by Equation 7.11 where $\Delta R_B = c/2B\cos(\beta/2)$, is the range resolution of the system, dependent on the instantaneous modulation bandwidth, B, bistatic angle, β, and δ_L is the angular bin width for the required look angle, in radians.

$$A_C = \Delta R_B R_R \delta_L \tag{7.11}$$

Using this simplification, the variation in clutter cell area for an example scenario is shown in Figure 7.5. The clutter cell area is a function of the range and cross-range resolution
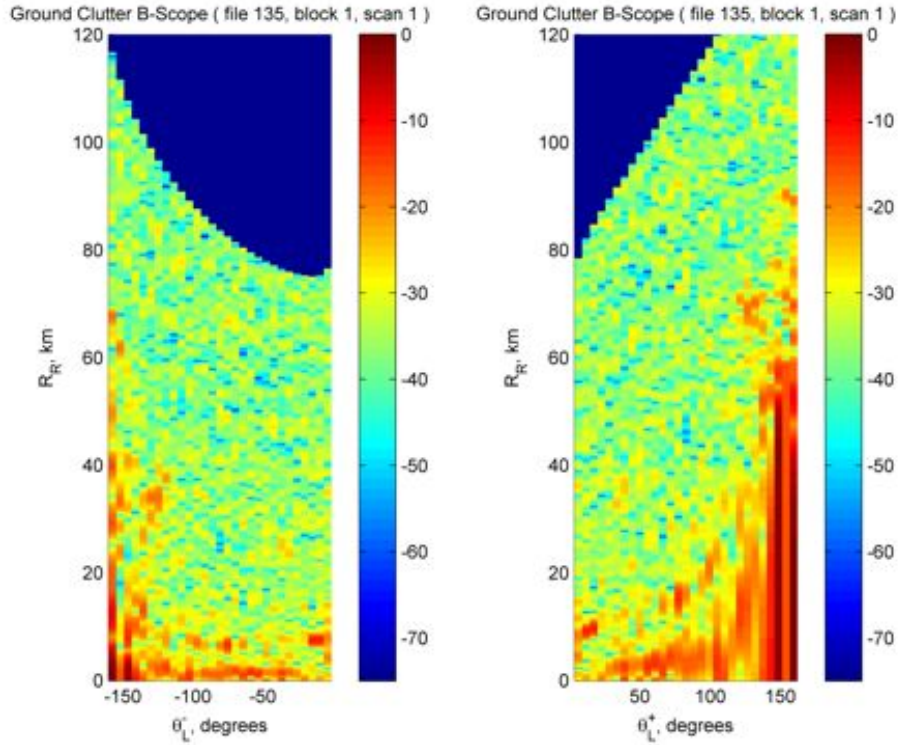
Figure 7.4: The stationary clutter component of the ARD surface transformed into slant range to target vs receiver look angle. The two images correspond to the ambiguity in the look angle.

therefore the resolution is lost in the direction of the receiver travel and in the opposite direction, as expected. Equally, in the vicinity of the baseline the clutter cell area increases. The finest resolution for a given imaging geometry will be achieved when the receiver is positioned to place the imaging target for $\beta = 0°$ and when operating with look angles normal to the direction of travel.

Plotting in cartesian coordinates requires a correction to reference the points to grid North. In cartesian coordinates, the location of a point in Cartesian space is shown in Equation 7.13 where θ_N is the bearing of the receiver velocity vector reference to grid North and RX_X and RX_Y are the x and y coordinates of the receiver position.

$$x = R_R \sin(\theta_L + \theta_N) + RX_X \tag{7.12}$$

$$y = R_R \cos(\theta_L + \theta_N) + RX_Y \tag{7.13}$$

An example of the completed transformation is shown in Figure 7.6. The dashed lines indicate the bin widths, which increase away from the normal with loss of resolution in the direction of travel and the direction opposite to the direction of travel, as expected. In this image, the left-right look angle ambiguity is present and the responses can not be
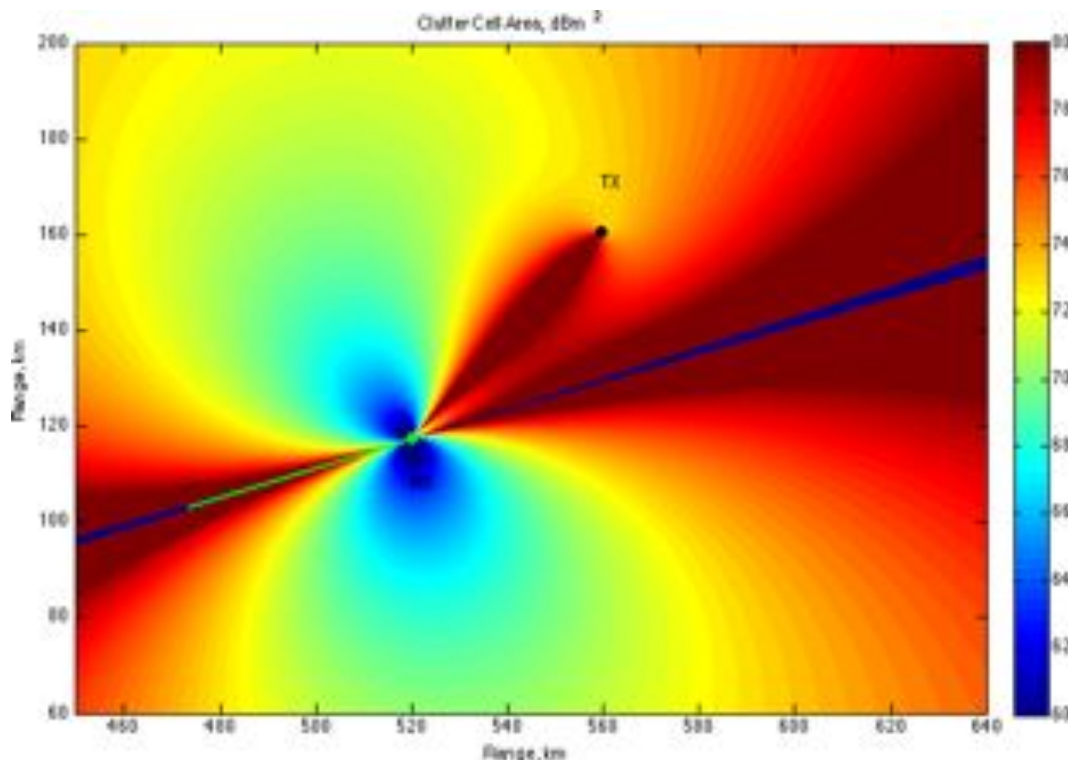
Figure 7.5: Clutter cell area assuming a rectangular clutter patch.

uniquely geolocated. A clear high response is seen in the vicinity of London and this is a common feature of all the processed data. This is to be expected since the dense urban area present as high RCS targets. The response remains in the same Cartesian location as the receiver continues on its course. This is the first demonstration of imaging using FM as an illuminator and an airborne passive bistatic receiver. The resolution is coarse since the range-resolution is poor and the system installation sub-optimal but for a cheap two channel system, it is an interesting demonstration of the state of the art.

In summary, a three stage process allows a range-Doppler bin in the ARD surface to be physically located on the surface of the Earth as Cartesian coordinates (x, y) with an ambiguity as dictated by the ambiguous look angle. For each range-Doppler bin, there will be two solutions and two sets of Cartesian coordinates. The three stage transformation is summarised in Table 7.1.

7.3   Clutter RCS Estimation

Offline, MATLAB was used to convert the raw ADC samples to 200 kHz bandwidth baseband complex signals. The signal from the antenna on the same side of the aircraft as the transmitter was chosen as the 'reference' channel and treated as the direct signal from the transmitter, whereas the signal from the antenna on the opposite side of the aircraft to

Table 7.1: Referencing stationary clutter in the range-Doppler surface to a physical location on the Earth's surface.

Stage	Format	Coordinates	Description
1	Range-Doppler plane	(R_B, f_B)	Relative bistatic range-Doppler surface $$f_{B_{MIN}} \leq f_B \leq f_{B_{MAX}}$$ Where: $$f_{B_{MIN}} = -\frac{|\mathbf{v_R}|}{\lambda}\left(1 + \cos\theta_{TX}\right)$$ $$f_{B_{MAX}} = \frac{|\mathbf{v_R}|}{\lambda}\left(1 - \cos\theta_{TX}\right)$$
2	B-Scope	(R_R, θ_L)	Physical location with reference to the receiver's velocity vector $$R_R = \frac{R_B^2 + 2LR_B}{2(R_B + L(1 - \mathbf{u_T} \cdot \mathbf{u_L}))}$$ $$\theta_L = \pm\cos^{-1}\left(\frac{1}{|\mathbf{v_R}|}\left(\lambda f_B + \mathbf{v_R} \cdot \mathbf{u_L}\right)\right)$$
3	Plan Position Indicator	(x, y)	Physical location on the Earth's surface relative to grid North and receiver location $$x = R_R \sin(\theta_L + \theta_N) + RX_X$$ $$y = R_R \cos(\theta_L + \theta_N) + RX_Y$$
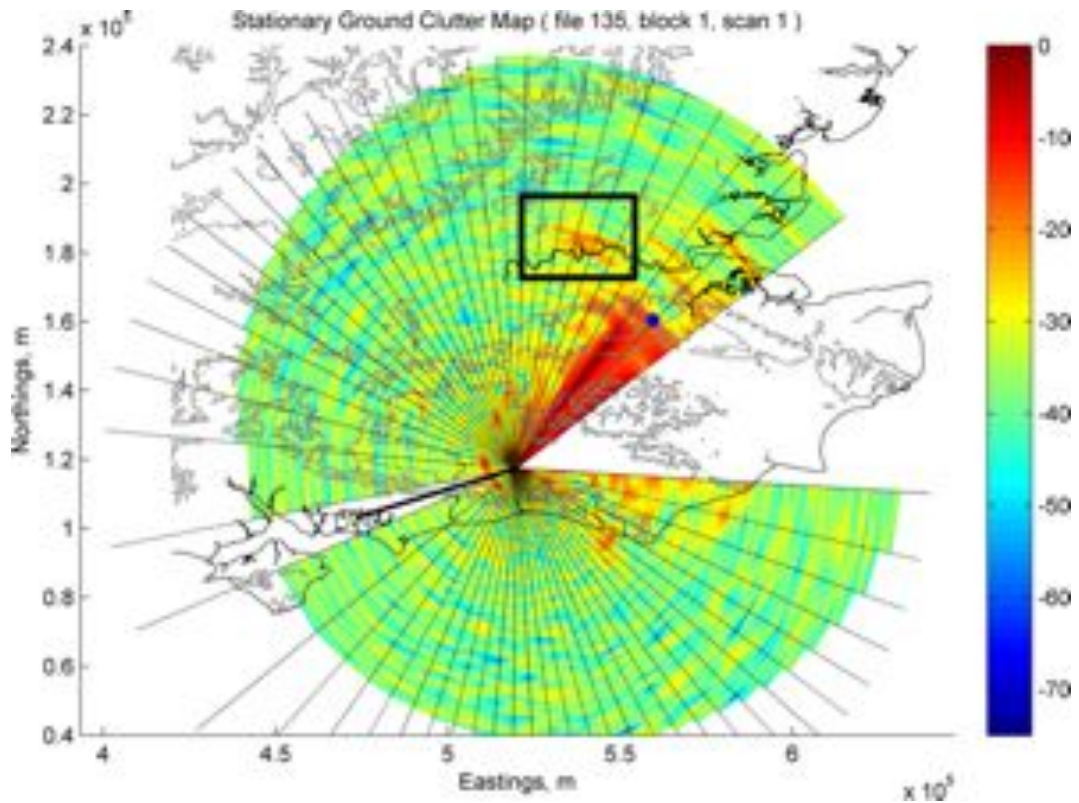
Figure 7.6: The output of the Doppler Beam Sharpening algorithm. The box denotes the high response seen over London. The dashed lines indicate the bin angular bin widths which increase away from the normal.

the transmitter was chosen as the surveillance channel. In order to maximise the clutter-to-noise ratio of the output processing, the level of the direct signal in the surveillance channel was reduced by filtering the surveillance channel, using an NLMS adaptive filter [74] to reduce the direct signal component, as for the air target detection case. The filtered surveillance signal is then cross-correlated with the reference signal to produce the Amplitude Range-Doppler (ARD) surface.

In order to calculate the surface clutter reflectivity a five stage process is applied to the coarse sharpened images:

i. Truncate ARD surface at noise floor

The noise floor of the ARD surface is set at the median amplitude of the surface values. The ARD is then truncated at the noise floor to ensure that the noise is not mapped to the Cartesian plane.

ii. Select stationary clutter Doppler bins
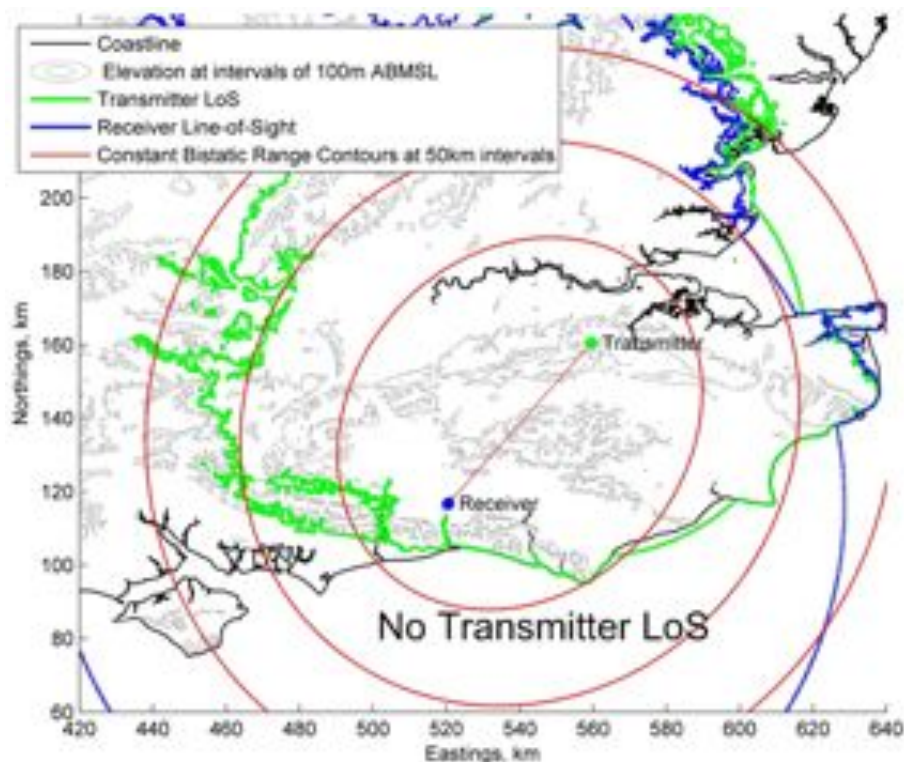
Figure 7.7: Transmitter to ground line of sight (green line) and receiver to ground line of sight (blue line), assuming a 4/3 earth model. The English Channel is not illuminated by the transmitter; therefore, the look angle of returns appearing to be from this area can be rejected. DTED data from EDINA Digimap Ordnance Survey Service, Panorama DTM 4965, http://edina.ac.uk/digimap, January 2012

The stationary clutter Doppler bins in the ARD are isolated and Equation 7.8 used to give the look angle for each Doppler bin. This process assumes that the clutter is stationary and yields two solutions, θ_L^+ and θ_L^-. Ideally the directivity of the receive antenna would be used to remove the ambiguity in look angle; however, in this experimental implementation, the receive antenna has no useful directivity and hence both solutions have to be considered valid at this stage.

iii. Uniquely identify physical location of clutter patch

In order to examine the clutter, the unique value of θ_L is necessary. In order for the clutter power to be measured at the receiver, it must have line-of-sight to the transmitter and to the receiver. Figure 7.7 shows the LoS limited coverage for the Wrotham antenna which is at an altitude of 370 m above mean sea level [61], calculated using the 4/3 earth approximation ignoring shadowing and diffraction effects. as discussed in Section 3.2. Figure 7.7 shows that the English Channel is not in the transmitter LoS therefore there will be no returns from the sea clutter in this area since it is not illuminated by the transmitter. The returns that appear to originate from this area can instead be attributed to the other

solution and a mask is constructed and applied to uniquely identify the clutter locations.

iv. Correct for digital filtering in spatial domain

The operation of the NLMS direct signal suppression filter is analogous to placing a null in the receive radiation pattern in the direction of the transmitter. The filter works to adjusts the phase of the reference signal so that it sums in antiphase with the direct signal in the direction of the transmitter, hence cancelling the direct signal from the surveillance channel. At directions away from the transmitter the signals are no longer in antiphase and the system can detect clutter. There will therefore be a relative power gain, between $-\infty$ dB and +6dB, in the clutter map which is dependent on the clutter direction with respect to the transmitter direction, described by G_{filter} in Equation (7.14).

$$G_{filter}(\theta_L) = \left| 1 - e^{j\frac{2\pi d}{\lambda}(\sin\theta_{TX} - \sin\theta_L)} \right|^2 \tag{7.14}$$

Where θ_{TX} is the direction of the transmitter relative to the aircraft heading, θ_L is the look angle to the clutter patch, relative to the aircraft heading, and d is the separation of the antennas, 0.4λ in this case. To compensate for the cardioid pattern which the cancellation introduces, the pattern is subtracted from the logarithmically-scaled clutter map.

v. Calculate bistatic RCS of clutter

Assuming that the transmitter Effective Radiated Power, $P_T G_T$, is constant in all directions towards the ground and the receiver antenna gain is omnidirectional with a constant gain of G_R, the clutter-to-noise ratio (CNR) in a 1/3 Hz bandwidth at the receiver output after matched filter processing and direct signal filter compensation, can be estimated as shown in Equation (7.15).

$$CNR = \frac{P_T G_T G_R \lambda^2}{(4\pi)^3 R_T^2 R_R^2 k T_0 F} \sigma_C \tag{7.15}$$

Where k is Boltzmann's constant, T_0 is 290K and F is the receiver noise factor at the output of the receiver. With the clutter location uniquely identified, the bistatic RCS for each pixel, σ_C, can then be estimated. The parameters for this system are displayed in Table 7.2. The installed receive antenna gain was estimated from the levels of the direct signal and is low since the antenna was a simple rod antenna that had to be placed on the inside of the window. An example plot of the clutter power relative to the ARD surface noise floor in the Cartesian plane is shown in Figure 7.8.

Table 7.2: Typical system parameters.

Parameter	Value
$P_T G_T$	250 kW
λ	3.37 m
G_R	-20 dBi
N	20 dB
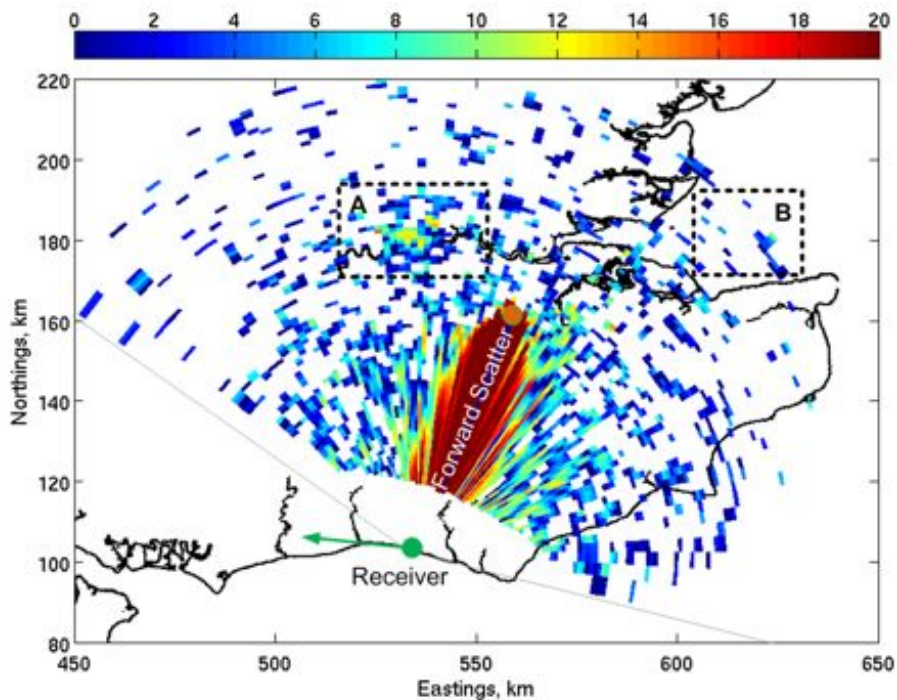
Figure 7.8: Example of a clutter-to-noise ratio plot (0 to 20 dB). Box A shows the high returns from central London and Box B shows that the system has the potential to examine sea clutter.

The processed stationary clutter image of Figure 7.8 demonstrates the basic imaging capability of this technique. Box A outlines the high returns in the vicinity of central London and Box B shows that the system has the coverage to examine sea clutter as well as land and urban clutter. Doppler Beam Sharpening typically yields clutter cells with areas of the order of 10^7 m^2 hence increasing the CPI further would help to improve the coarse resolution of this system.

Over multiple looks, the bins in Figure 7.8 are compiled together to allow frequency analysis and examination of the variation in bistatic RCS with their associated variables, as demonstrated in the next section.

7.4   Bistatic Clutter Analysis

The processing described in Section 7.2 was applied to forty separate coherently processed looks for the situation where the receiver was travelling at a near constant velocity and altitude. The variation in RCS with transmit and receiver grazing angles and bistatic angles was then investigated. The size of the clutter cell means that a varied terrain analysis can not be conducted. For example, a clutter cell will likely contain both urban and rural clutter. The aim of this analysis is not to comprehensively define the clutter behaviour or to accurately measure the RCS, but to gain an insight into the likely levels of clutter. Currently, values for VHF bistatic clutter RCS are assumed based on extrapolation from clutter measurements at significantly higher frequencies. In the same manner, the polarisation of the receiver is not defined, due to antenna coupling issues, therefore the RCS values estimated in this work are a useful first step in validating typically assumed values.

7.4.1   Clutter RCS Variation with Grazing Angles

The surface height of the clutter cells were approximated as the mean height over the clutter cell[1] and in turn the mean clutter patch heights were used to estimate the transmit and receive grazing angles. The further away from the transmitter and receiver, the less sensitive the grazing angle is to variation in height within a clutter cell. In this case, with the mask applied to the data in the Cartesian plane, the vast majority of clutter cells have transmit and receive grazing angles of less than 1° and so analysis of clutter behaviour over a range of grazing angles is not possible.

In order to gain an insight into the dependence of grazing angle on the bistatic RCS, a further experimental flight trial would be required. A greater spread of grazing angles could be achieved by flying higher or by including a roll manoeuvre in the flight profile. The latter option would require an Inertial Navigation System (INS) in conjunction with the GPS receiver in order to correctly capture the receiver's motion.

7.4.2   Clutter RCS Variation with Bistatic Angle

There is full variation in bistatic angle across the compiled looks, therefore the variation of clutter behaviour with bistatic angle was investigated. The clutter statistics were estimated

---

[1]DTED data from EDINA Digimap Ordnance Survey Service, Panorama DTM 4965, http://edina.ac.uk/digimap, January 2012

by collating the separate looks, ignoring the variation in clutter type across the scene and ignoring the receive polarisation.

The median clutter power, σ_C, is plotted in Figure 7.9 for bistatic angles between 20° and 160°. The result demonstrates a relatively smooth relationship between the median σ_C and bistatic angle. With the larger bistatic angles, the σ_C increases. This behaves as expected since as the clutter approaches the forward scatter region, the forward scatter enhancement effect will increase the RCS of the clutter markedly, which is demonstrated here. The results here are dependent on the specific geometry however there is an obvious null in bistatic angle between 60° to 80° and then the σ_C increases as the bistatic angle reduces and heads into the pseudo-monostatic zone. The median normalised clutter RCS,
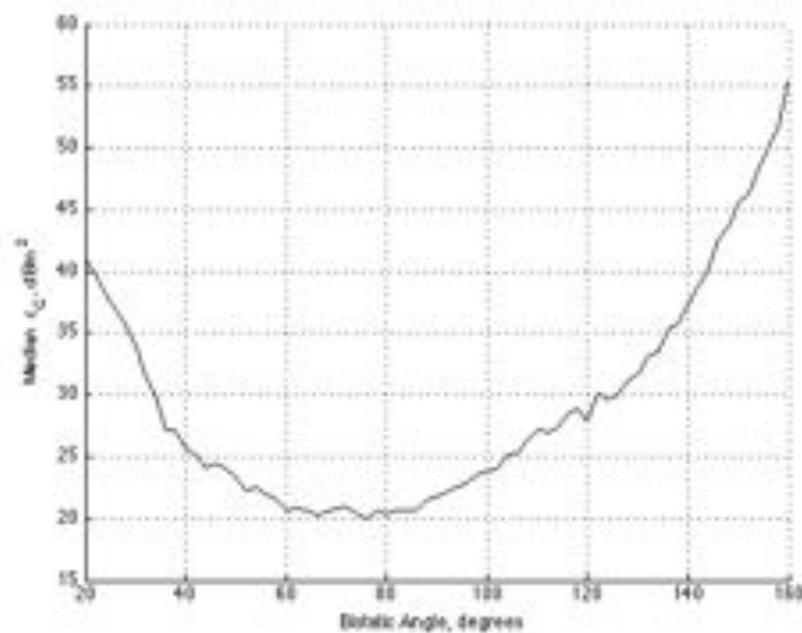
Figure 7.9: Variation in median clutter power, σ_C, with bistatic angle for low transmit and receive grazing angle.

σ_0, is plotted with respect to bistatic angle in Figure 7.10 where $\sigma_C = \sigma_0 A_C$, with A_C defined in Equation 7.11. Calculating the specific reflectivity in this way implicitly includes any propagation factors within the value of σ_0 and σ_0. Again the median normalised clutter RCS exhibits a smooth variation with bistatic angle, with a minimum occurring for bistatic angles from 60° to 90°, rising up to a maximum as the bistatic angle approaches 180°, isolating the clutter cells close to and on the baseline. For low bistatic angles, the normalised clutter RCS increases from the minimum, representing clutter in the pseudo-monostatic region. The surface clutter power plot includes the area of the clutter cell and this curve is similar in shape to the normalised clutter RCS curve for low grazing angle
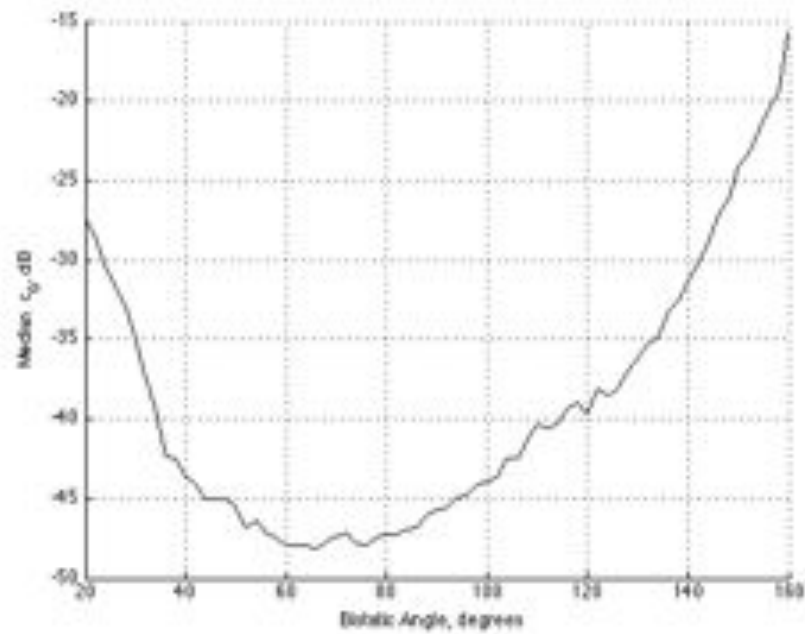
Figure 7.10: Variation in median normalised RCS, σ_0, with bistatic angle for low transmit and receive grazing angle.

clutter (less than 1°).

The measured values of σ_0 give the normalised RCS of generic ground clutter to be of the order of -45 to -15 dB and shows a definite relationship with the bistatic angle.

7.5 Conclusion

A Doppler Beam Sharpening technique for cross-range resolution improvement has been developed and applied to data collected from an airborne passive bistatic radar demonstrator system. The potential of this technique is demonstrated through the application to real data to produce coarse resolution imaging of ground clutter in the surveillance area. High returns from major extended features such as London have been observed. The resolution achievable using FM as an illuminator is poor due to its low modulation bandwidth. Using a wideband digital waveform, such as DAB or DTV, would provide a more useful resolution. Current work on fusing multiple DTV waveforms to form a wideband illuminating signal, would provide resolution that would give an interpretable view of the surface. Equally, flying faster and integrating longer would provide narrower cross-range dimensions. In conjunction with a SAR based image formation approach, as opposed to the amplitude Doppler Beam Sharpening technique used here, would be the next logical step in the development of airborne passive bistatic imaging.

The analysis of the experimentally measured clutter returns gives an insight into the behaviour of stationary ground clutter and allows the median clutter level variation with bistatic angle to be estimated. The measured clutter values are reasonable and increase both in the region of the baseline and also in the pseudo-monostatic region, with the values measured between -45 to -15 dB. The shape of the response suggests that for a given target RCS, the receiver's mobility can be used to set up the geometry so that the area of interest is placed within bistatic angles of between 40° and 100° and so reduce the clutter levels considerably when compared with trying to detect a target in clutter from a pseudo-monostatic or forward scatter geometry, where the median normalised clutter RCS increases.

This initial analysis will allow future system performance planning and clutter simulation to be based on measured low grazing angle clutter behaviour for this VHF passive bistatic system. This is the first time this processing has been applied to an airborne passive radar system using FM as an illuminator and the first demonstration of a passive bistatic image formation and collecting actual data. This work was published at the peer reviewed Radar 2012 conference [3] and was shortlisted for the best student paper award.

Chapter 8

Conclusions and Future Work

This chapter highlights the key findings of this research and identifies the specific areas of further investigation that will allow for the realisation of the unique capability that Airborne PBR would provide as part of a next generation sensor suite. A summary of the key findings is discussed in Section 8.1 and the future work identified is in Section 8.2.

8.1 Summary of Findings

As stated in the introduction to this work, the purpose of this research was to demonstrate the successful operation of an airborne passive bistatic radar using FM broadcasts as the illuminator for air target detection and to gain a quantitative understanding of the behaviour of VHF bistatic clutter.

A literature review was performed in order to identify and understand the state of the art in airborne passive radar technology. Compared to the relative maturity of static ground based passive radar, there was very little documented research on the airborne application of passive radar and less still on practical results. It was apparent that collecting and analysing real airborne experimental data would add substantially to the published research in the development of techniques for airborne passive radar. Specifically, the detection of targets had not been conclusively demonstrated and there was very little understanding of the airborne clutter behaviour at VHF.

Since this was an area where focussed research could have a measurable impact, a quantitative study of the airborne passive radar problem was performed in order to estimate the feasibility and utility of a simple PBR system in detection of air targets. A deterministic model was constructed and used to examine the likely coverage of an airborne passive radar, with an FM illuminator, assuming conservative estimates for the receiver parameters. The

results of this work identified a useable coverage area, typically in the vicinity of the receiver and transmitter, and identified the following performance limiting factors:

- The sensitivity of the system is limited by the dynamic range of the front-end ADC

- The transmitter has to be dynamically selected in order to optimise resolution and coverage

- The coherent processing interval has to be optimised to ensure that the time-bandwidth product is maximised whilst preventing target range and Doppler walk

The model provided a foundation from which to scope and quantify the physical design of a two-channel demonstrator system.

In order to collect the airborne experimental data, the receiver was designed to the specifications dictated by the quantitative simulation with the additional constraints associated with operating the system independently on the aircraft. The battery powered two channel system was constructed and tested and was found to be linear and have acceptable noise performance. The system was tested to ensure that there were no RFI issues with the on board safety critical systems and that the RF sources on the aircraft did not interfere with the receiver.

Having developed a robust data collection system, it was imperative that the airborne experiments be conducted using the most favourable modulations and geometries in order to achieve the main effort of air target detection. The deterministic simulation combined with historic air truth data fed into the optimisation of the experimental flight profiles. The intention was to perform the experiments near to the London airspace, the air truth data suggested that the density of air traffic was constant, therefore this was an effective method of designing an appropriate flight path, to ensure that the probability of detection of an aircraft was maximised.

The demonstrator was then flown on two experimental data collection flights, with the demonstrator system installed and the data processed for the detection of air targets and the characterisation of ground clutter data.

A processing scheme for air target detection was developed and the airborne data processed for the detection of air targets. The output of the first experiment displayed clear high velocity responses outside of the stationary and moving ground clutter bandwidths. These responses mapped on to established aircraft flight paths as identified in the experimental planning phase. The second experiment was conducted in parallel with air truth

data collection, in order to identify specific air target detections. The detailed analysis of the system detections, confirmed that the demonstrator had detected air targets. The high correlation between the air targets and the system detection, demonstrating for the first time, the detection of an airborne target from an airborne passive bistatic receiver.

Collecting real data, allowed the behaviour of VHF bistatic clutter to be investigated. The motion of the receiver during the flight was used to create a Doppler Beam Sharpened clutter map of the surface, in effect, a coarse surface imaging technique. The creation of the surface image, allowed the clutter variation in the spatial domain to be analysed. The imaging technique allowed the physical georeferencing of the clutter bins in the cartesian plane allowing the transmit and receive ranges to be estimated and hence, the normalised bistatic clutter RCS of the stationary clutter patch to be calculated. This is the first time that the Doppler Beam Sharpening technique has been demonstrated on real data.

The analysis of the normalised clutter RCS gave realistic values for the surface clutter and insight in its variation with bistatic angle for low grazing-angle surface clutter.

The main contributions of this work can therefore be summarised as follows:

- Development of a low cost lightweight air mobile passive FM receiver

- Development of novel signal processing algorithms for passive air target detection and ground imaging

- Demonstrated the first detection of an air target using an airborne FM passive bistatic radar

- Demonstrated the first Doppler beam sharpened image of stationary ground clutter using an airborne FM passive bistatic radar

- Quantified the estimated levels of clutter cross-section variation with bistatic angle.

8.2 Future Work

This work has identified key areas of further research that will increase the TRL of airborne passive radar.

- **Direct Signal Interference** For an ADC with finite dynamic range, the strength of the direct signal will reduce the receiver's sensitivity to the detection of low RCS targets and this is major limiting factor of the system performance. The DSI can be

reduced digitally, post signal capture and also in the analogue domain, prior to the ADC. Analogue cancellation is an established technique however scaling for multiple receive elements as part of an array, would introduce complexity and increase the size, weight and power requirements of the system. A more elegant approach would be to employ a high dynamic range ADC, typically greater than 16 bits, and a receive array of more than two elements. This would allow direct sampling of the RF signal without the coherence and non-linear effects of a complex analogue canceller front-end. Taking advantage of the adaptive angular nulling and adaptive direct signal suppression filtering techniques used in the communications industry would give the most efficient signal capture and allow detection sensitivity to be increased.

- **Airborne VHF Antenna Array** A multi-element receive array would allow adaptive beam forming to introduce adaptive nulls in the directions of the transmitter and strong multipath. The design and installation of a VHF array for an airborne platform will be an important aspect of any future work, especially for an LO platform. Augmenting the poor range resolution with Angle of Arrival information would allow the receiver to locate a target using a single baseline which would give a single-pulse 2D target location capability and reduce the large location ambiguities experienced in this work.

- **Resolution** The range resolution of the target detections demonstrated in this work is poor due to the narrow and variable modulation bandwidth of the FM signal. Fusing multiple FM channels together has been demonstrated to improve the range resolution and bandwidth. However there is a limit to the performance that can be achieved with FM. There would be a very useful piece of future work to look at building a broadband demonstrator system that could take advantage of the high power but poor resolution FM waveforms, to detect the targets at a long stand off distance, then switch to a digital signal to perform accurate target location at shorter range. A multi band system that could exploit signals of opportunity from 80 MHz to 10 GHz could make use of broadcast radio services such as DAB, broadcast TV services such as DVB-T and civil and military air traffic control and weather radars.

- **Air Target Tracking and Localisation** The target detections shown in this work, need to be associated together to form tracks in order for the radar output to be of practical use. An understanding of target tracking for poor range resolution bistatic

systems would feed into understanding how many degrees of freedom are required in the receive array and the necessary track update rate. The influence of missed detections and high altitude performance could also be quantified. Demonstrating a robust bistatic tracker would provide the impetus for the development of a next generation demonstrator system.

- **Illuminators** In the same way that a radar resource manager adaptively selects and optimises a multi-function radar's parameters, in a passive system, an illuminator manager system is required in order to make best use of the plethora of available illuminators. For example, the adaptive selection of high power FM signals for horizon scanning interleaved with the use of cell phone basestations or DAB for local threat detection would be an integral part of any passive system. Equally there are new modulation standards that have been recently introduced, such as WiMax and 4G that will give an airborne passive radar a wider selection of illuminators and detection geometries.

- **Clutter** The insights into bistatic clutter achieved in this work would need to be supported by further experimental flights in order to gather more data for analysis. The system would need to be upgraded in order to give increased resolution and to ensure that the receiver noise floor was low enough to allow more of the clutter to be seen. This would require a new lower noise front-end and longer integration times to achieve a finer cross-range resolution. In order to ensure that the Doppler Beam Sharpening processing gives sharp results, an improved navigation solution would be required, fusing the 1 Hz GPS update with an Inertial Navigation System measurement. A satisfactory navigation system of this type can be purchased off the shelf.

The business case for development and exploitation of airborne PBR will need to engage with the end-users to understand their capability gaps and where a passive bistatic system might offer capability that can not be gained in other ways. As stated previously, an obvious application of a passive radar system is on an LO platform, to complement the passive EO/IR sensors in developing a situational awareness capability. Having a robust picture of airborne threats and the ability to perform GMTI type processing, using nothing more than organic communication and broadcast signals would provide a definite capability for an LO UAV. This would allow the development of covert mission profiles for Intelligence,

Surveillance and Reconnaissance missions where the platform enters a hostile airspace, operates its passive sensors and then leaves the hostile airspace, having maintained the platform's stealth throughout the entire mission.

At the time of writing, this preliminary research demonstrates the state of the art in airborne passive bistatic radar. As nations begin to invest heavily in LO technology, future research and development, centred on the areas identified in this work, will yield the necessary performance to increase the survivability and capability of an LO platform.

Bibliography

1 J. Brown, K. Woodbridge, A. Stove, and S. Watts. Air target detection using airborne passive bistatic radar. Electronics Letters, 2010.

2 J. Brown, K. Woodbridge, H. Griffiths, A. Stove, S. Watts. Passive bistatic radar experiments from an airborne platform. IEEE Aerospace and Electronic Systems Magazine, 2012.

3 J. Brown, K. Woodbridge, A. Stove, and S. Watts. VHF airborne passive bistatic radar ground clutter investigation. IET International Radar Conference, 2012.

4 N. J. Willis. Bistatic Radar, volume 8. SciTech Publishing, 2005.

5 M. C. Jackson. The geometry of bistatic radar systems. IEE Proceedings on Communications, Radar and Signal Processing, 1986.

6 M. Malanowski and K. Kulpa. Analysis of integration gain in passive radar. International Radar Conference, 2008.

7 N. J. Willis and H.D. Griffiths. Advances in Bistatic Radar. SciTech Publishing, 2007.

8 H.D. Griffiths and C. J. Baker. The signal and interference environment in passive bistatic radar. IEEE Conference on Decision and Control, 2007.

9 N. Levanon and E. Mozeson. Radar Signals. John Wiley and Sons, 2004.

10 T. Tsao, D. Weiner, P. Varshney, H. Schwarzlander, M. Slamani, and S. Borek. Ambiguity function for a bistatic radar. Proceedings of the IEEE International Symposium on Time-Frequency and Time-Scale Analysis, volume 33, pages 497-500, 1997.

11 C. J. Baker, H.D. Griffiths, and I. Papoutsis. Passive coherent location radar systems. Part 2: Waveform properties. IEE Proceedings on Radar, Sonar and Navigation, 2005.

12 J. D. Sahr and F. D. Lind. The Manastash Ridge radar: A passive bistatic radar for upper atmospheric radio science. Radio Science, 1997.

13 C.L. Zoeller, M.C. Budge, and M.J. Moody. Passive coherent location radar demonstration. IEEE Proceedings of the Thirty-Fourth Southeastern Symposium on System Theory, pages 358-362, 2002.

14 P. Howland, D. Maksimiuk, and G. Reitsma. FM radio based bistatic radar. IEE Proceedings on Radar, Sonar and Navigation, 2005.

15 DW OHagan. Signal and Interference Analysis: Proposed Analogue Signal Suppression Techniques for PCL Radar. Radar Conference, 2006.

16 H.D. Griffiths and C. J. Baker. Passive coherent location radar systems. Part 1: Performance prediction. IEE Proceedings on Radar, Sonar and Navigation, 2005.

17 F Colone, R Cardinali, and P Lombardo. Cancellation of clutter and multipath in passive radar using a sequential approach. IEEE Radar Conference, 2006.

18 R. Cardinali, F. Colone, P. Lombardo, O. Crognale, A. Cosmi, and a. Lauri. Multipath cancellation on reference antenna for passive radar which exploits FM transmission. IET International Conference on Radar Systems 2007, pages 192-192, 2007.

19 S. Heunis, Y. Paichard, and M. Inggs. Passive radar using a software-defined radio platform and open source software tools. IEEE Radar Conference 2011, pages 879-884, 2011.

20 C. Bongioanni, F. Colone, and P. Lombardo. Performance analysis of a multi- frequency FM based Passive Bistatic Radar. IEEE Radar Conference, pages 1-6, 2008.

21 H.D. Griffiths, C. J. Baker, H Ghaleb, R. Ramakrishnan, and E. Willman. Measurement and analysis of ambiguity functions of off-air signals for passive coherent location. Electronics Letters, 2003.

22 K. E. Olsen and K. Woodbridge. FM based passive bistatic radar range resolution improvement. International Radar Symposium, 2011.

23 K. E. Olsen. FM based passive bistatic radar target range improvement – Part II. International Radar Symposium, 2010.

24 K. E. Olsen and K. Woodbridge. Analysis of the performance of a multiband passive bistatic radar processing scheme. International Waveform Diversity and Design Conference, 2010.

25 D. Gould, R. Pollard, C. Sarno, and P. Tittensor. A Multiband Passive Radar Demonstrator. International Radar Symposium, 2006.

26 D. Gould, R. Pollard, C. Sarno, and P. Tittensor. Developments to a multiband passive radar demonstrator system. IET International Conference on Radar Systems, 2007.

27 D. Shephard and G. Richards. Passive target tracking using transmitters of opportunity. Target Tracking and Data Fusion, 2008.

28 H. J. Yardley. Bistatic radar based on DAB illuminators: The evolution of a practical system. IEEE Radar Conference, pages 688-692, 2007.

29 C. Coleman and H. Yardley. DAB based passive radar: Performance calculations and trials. International Radar Conference, pages 691-694, 2008.

30 F Berizzi, M Martorella, D. Petri, M. Conti, and A. Capria. USRP technology for multiband passive radar. IEEE Radar Conference, pages 225-229, 2010.

31 D. Petri, A. Capria, M. Conti, F Berizzi, M Martorella, and E.D. Mese. High range resolution multichannel DVB-T passive radar : aerial target detection. Tyrrhenian International Workshop on Digital Communications - Enhanced Surveillance of Aircraft and Vehicles, pages 129-132, 2011.

32 J. Fawcette. Vulnerable radar seeks a safe sanctuary. Microwave Systems News, 1980.

33 J. S. Bailey and G. A. Gray. Sanctuary signal processing requirements. Circuits and Systems, 1977.

34 M. Buchbinder, F. Esposito, and H. Perini. Sanctuary receive antenna system. Antennas and Propagation Society International Symposium, pages 146-149, 1980.

35 R. Klemm. Introduction to space-time adaptive processing. Electronics Communication Engineering Journal, 1999.

36 R. Klemm. Principles of Space-Time Adaptive Processing. IET, 2002.

37 K. P. Ong. Signal processing for airborne bistatic radar. PhD Thesis, University of Edinburgh, 2003.

38 F. Colone, M Labriola, and F Poli. A pre-Doppler approach for reduced loss bistatic STAP. International Conference on Radar, 2006.

39 W. L. Melvin. Adaptive cancellation method for geometry induced nonstationary bistatic clutter environments. IEEE Transactions On Aerospace And Electronic Systems, 2007.

40 X. Meng, T. Wang, J. Wu, and Z. Bao. Bistatic clutter analysis and range ambiguity resolving for space time adaptive processing. IET Radar, Sonar and Navigation, 2009.

41 R. Klemm. Principles of space–time adaptive processing, 3rd Edition, The Institute of Engineering and Technology, 2006.

42 W. L. Melvin and M. J. Callahan. Bistatic STAP: application to airborne radar. IEEE Radar Conference, 2002.

43 J. R. Rasmusson, M. Blom, B. Flood, P. O. Frolind, A. Gustavsson, T. Jonsson, B. Larsson, G. Stenstrom, and L. M. H. Ulander. Bistatic VHF and UHF SAR for urban environments. SPIE, 2007.

44 A Barmettler, L Zuberbuhler, and E Meier. Swiss airborne monostatic and bistatic dual-pol SAR experiment at the VHF band. EUSAR, 2008.

45 L.M.H. Ulander, A Barmettler, B. Flood, P. O. Frolind, A. Gustavsson, T. Jonsson, E. Meier, J. Rasmusson, and G. Stenstrom. Signal-to-clutter ratio enhancement in bistatic very high frequency band SAR images of truck vehicles in forested and urban terrain. IET Radar, Sonar and Navigation, 2010.

46 R. Baque, P. Dreuillet, O.R. du Plessis, H. Cantalloube, L.M.H. Ulander, G. Stenstro, T. Jonsson, and A. Gustavsson. LORAMbis A bistatic VHF/UHF SAR experiment for FOPEN. 2010 IEEE Radar Conference, 2010.

47 R. Baque, P. Dreuillet, and OR du Plessis. Results of the LORAMbis bistatic VHF/UHF SAR experiment for FOPEN. IEEE Radar Conference, 2011.

48 W. Chao, W. Yongliang, L. Rongfeng, and F. Xikun. On concept and SCR of PCL AEW utilizing illuminators of opportunity. International Radar Conference, 2006.

49 D.K.P. Tan, M. Lesturgie, Hongbo Sun, and Yilong Lu. Target detection performance analysis for airborne passive bistatic radar. In 2010 IEEE International Geoscience and Remote Sensing Symposium, number 1, pages 35533556, 2010.

50 D. K. P. Tan, M. Lesturgie, H. Sun, and Y. Lu. Signal analysis of airborne passive radar using transmissions of opportunity. IEEE CIE International Radar Conference, pages 169-172, 2011.

51 M. Malanowski, K. Kulpa, and Jacek Misiurewicz. PaRaDe - PAssive RAdar DEmonstrator family development at Warsaw University of Technology. IEEE Microwaves, Radar and Remote Sensing Symposium, 2008.

52 M. Malanowski and K. Kulpa. Digital beamforming for Passive Coherent Location radar. IEEE Radar Conference, 2008.

53 B. Dawidowicz and K. S. Kulpa. Experimental results from PCL radar on moving platform. International Radar Symposium, 2008.

54 K. Kulpa, M. Malanowski, P. Samczynski, J. Misiurewicz, and M. Smolarczyk. On-board PCL systems for airborne platform protection. Tyrrhenian International Workshop on Digital Communications - Enhanced Surveillance of Aircraft and Vehicles, 2011.

55 K. Kulpa, M. Malanowski, P. Samczynski, and B. Dawidowicz. The concept of airborne passive radar. IEEE Microwaves, Radar and Remote Sensing Symposium, 2011.

56 B. Dawidowicz, K. Kulpa, and M. Malanowski. Suppression of the ground clutter in airborne PCL radar using DPCA technique. European Radar Conference, 2009.

57 B. Dawidowicz, K.S. Kulpa, M. Malanowski, J. Misiurewicz, P. Samczynski, and M. Smolarczyk. DPCA detection of moving Targets in airborne passive radar. IEEE Transactions on Aerospace and Electronic Systems, 2012.

58 J. Raout, a. Santori, and E. Moreau. Spacetime clutter rejection and target passive detection using the APES method. IET Signal Processing, 2010.

59 B. Taylor and A. Thompson. The international system of units (SI). National Institute of Standards and Technology, 2008

60 J.D. Kraus and R.J. Marhefka. Antennas for All Applications. McGraw-Hill, 2003.

61 G. H. Millard. The introduction of mixed polarization for vhf sound broadcasting: The Wrotham installation. Technical report, BBC, 1982.

62 E. F. Knott, J. F. Shaeffer, and M. T. Tuley. Radar Cross Section. SciTech Publishing, 2004.

63 PicoScope 4000 Series, PicoTechnology. Retrieved from http://www.picotech.com/precision-oscilloscopes.html, 2012

64 QRP2000 USB-Controlled Synthesizer. Retrieved from http://www.sdr-kits.net, 2012.

65 R. G. Vaughan, N. L. Scott, and D. R. White. The theory of bandpass sampling. IEEE Signal Processing, 1991.

66 D. W. OHagan and C. J. Baker. Passive Bistatic Radar (PBR) using FM radio illuminators of opportunity. New Trends for Environmental Monitoring Using Passive Systems, 2008.

67 Cherokee Archer II Pilot's Operating Handbook, Number 761. Notre Dame Pilot Initiative, 2004.

68 BBC National FM Radio Stations, retrieved from http://www.bbc.co.uk/reception/transmitters/radio/, 2012.

69 Ofcom. Technical Parameters for UK VHF, MF and DAB Transmitters. Retrieved from http://stakeholders.ofcom.org.uk/broadcasting/guidance/tech-guidance/tech_parameters/, 2012.

70 BBC. BBC Local FM Radio Stations. Retrieved from http://www.bbc.co.uk/reception/transmitters/radio/localy_radio_rhc.shtml, 2012.

71 F. Colone, R. Cardinali, P. Lombardo, O. Crognale, A. Cosmi, A. Lauri, and T .Bucciarelli. Space-time constant modulus algorithm for multipath removal on the reference signal exploited by passive bistatic radar. IET Radar, Sonar & Navigation, 2009.

72 W. L. Melvin and J. A. Scheer. Principles of modern radar: advanced techniques. SciTech, 2012.

73 J. Treichler and B. Agee. A new approach to multipath correction of constant modulus signals. IEEE Transactions on Acoustics, Speech, and Signal Processing, 1983.

74 F. Colone, D. W. OHagan, P. Lombardo, and C. J. Baker. A Multistage processing algorithm for disturbance removal and target detection in passive bistatic radar. IEEE Transactions on Aerospace and Electronic Systems, 2009.

75 K. Kulpa. The CLEAN type algorithms for radar signal processing. IEEE Microwaves, Radar and Remote Sensing Symposium, 2008.

Bibliography

[1] J. Brown, K. Woodbridge, A. Stove, and S. Watts. Air target detection using airborne passive bistatic radar. *Electronics Letters*, 46(20):1396, 2010.

[2] James; Brown, Karl; Woodbridge, Andy; Stove, and Simon Watts. VHF airborne passive bistatic radar ground clutter investigation. In *2012 IET International Radar Conference on Radar Systems*, 2012.

[3] James Brown, Karl Woodbridge, Andy Stove, and Simon Watts. VHF AIRBORNE PASSIVE BISTATIC RADAR GROUND CLUTTER INVESTIGATION. In IET, editor, *IET Radar Conference 2012*, pages 2–5, Glasgow, 2012. IET.

[4] Nicholas J. Willis. *Bistatic Radar*, volume 8. SciTech Publishing, 2005.

[5] M C Jackson. The geometry of bistatic radar systems. *Communications, Radar and Signal Processing, IEE Proceedings F*, 133(7):604 –612, 1986.

[6] M. Malanowski and K. Kulpa. Analysis of integration gain in passive radar. *2008 International Radar Conference*, (7):323–328, 2008.

[7] Nicholas J. Willis and H.D. Griffiths. *Advances in Bistatic Radar*. SciTech Publishing, 2007.

[8] H.D. Griffiths and C. J. Baker. The signal and interference environment in passive bistatic radar. *, Decision and Control, 2007. IDC'07*, pages 1–10, 2007.

[9] Nadav Levanon and Eli Mozeson. *Radar Signals*. John Wiley & Sons, 2004.

[10] T. Tsao, D. Weiner, P. Varshney, H. Schwarzlander, M. Slamani, and S. Borek. Ambiguity function for a bistatic radar. In *[1992] Proceedings of the IEEE-SP International Symposium on Time-Frequency and Time-Scale Analysis*, volume 33, pages 497–500. IEEE, 1997.

[11] C. J. Baker, H.D. Griffiths, and I. Papoutsis. Passive coherent location radar systems. Part 2: Waveform properties. *IEE Proceedings - Radar, Sonar and Navigation*, 152(3):160, 2005.

[12] J. D. Sahr and F. D. Lind. The Manastash Ridge radar: A passive bistatic radar for upper atmospheric radio science. *Radio Science*, 1997.

[13] C.L. Zoeller, M.C. Budge, and M.J. Moody. Passive coherent location radar demonstration. In *Proceedings of the Thirty-Fourth Southeastern Symposium on System Theory (Cat. No.02EX540)*, pages 358–362. IEEE, 2002.

[14] P. Howland, D. Maksimiuk, and G. Reitsma. FM radio based bistatic radar. *IEE Proceedings - Radar, Sonar and Navigation*, 152(3):107, 2005.

[15] DW O'Hagan. Signal and Interference Analysis: Proposed Analogue Signal Suppression Techniques for PCL Radar. *Radar Conference, 2006. . . .*, 9(September):296–298, 2006.

[16] H.D. Griffiths and C. J. Baker. Passive coherent location radar systems. Part 1: Performance prediction. *IEE Proceedings - Radar, Sonar and Navigation*, 152(3):153, 2005.

[17] F Colone, R Cardinali, P Lombardo, and Infocom Dpt. Cancellation of clutter and multipath in passive radar using a sequential approach. pages 393–399, 2006.

[18] R. Cardinali, F. Colone, P. Lombardo, O. Crognale, a. Cosmi, and a. Lauri. Multipath cancellation on reference antenna for passive radar which exploits FM transmission. *IET International Conference on Radar Systems 2007*, pages 192–192, 2007.

[19] S. Heunis, Y. Paichard, and M. Inggs. Passive radar using a software-defined radio platform and opensource software tools. In *2011 IEEE Radar Conference*, pages 879–884, 2011.

[20] Carlo Bongioanni, F. Colone, and P. Lombardo. Performance analysis of a multi-frequency FM based Passive Bistatic Radar. *2008 IEEE Radar Conference*, pages 1–6, May 2008.

[21] H.D. Griffiths, C. J. Baker, H Ghaleb, R. Ramakrishnan, and E. Willman. Measurement and analysis of ambiguity functions of off-air signals for passive coherent location. *Electronics Letters*, 39(13):1005–1007, 2003.

[22] Karl Erik Olsen and Karl Woodbridge. FM Based Passive Bistatic Radar Range Resolution Improvement.

[23] KE Olsen. FM based passive bistatic radar target range improvement-Part II. *Radar Symposium (IRS), . . .*, 2010.

[24] Karl Erik Olsen and K. Woodbridge. Analysis of the performance of a multiband passive bistatic radar processing scheme. *2010 International Waveform Diversity and Design Conference*, pages 000142–000149, August 2010.

[25] Dale Gould, Robert Pollard, Carlos Sarno, and Paul Tittensor. A Multiband Passive Radar Demonstrator. *2006 International Radar Symposium*, pages 1–4, May 2006.

[26] D. Gould, R. Pollard, C. Sarno, and P. Tittensor. Developments to a multiband passive radar demonstrator system. *IET International Conference on Radar Systems 2007*, pages 188–188, 2007.

[27] D Shephard and G Richards. Passive target tracking using transmitters of opportunity. *Target Tracking and Data Fusion: . . .*, pages 151–157, 2008.

[28] Heath J. Yardley. Bistatic Radar Based on DAB Illuminators: The Evolution of a Practical System. *2007 IEEE Radar Conference*, pages 688–692, April 2007.

[29] Cristopher Coleman and Heath Yardley. DAB based passive radar: Performance calculations and trials. *2008 International Conference on Radar*, pages 691–694, September 2008.

[30] F Berizzi, M Martorella, D. Petri, M. Conti, and A. Capria. USRP technology for multiband passive radar. *2010 IEEE Radar Conference*, pages 225–229, 2010.

[31] D. Petri, A. Capria, M. Conti, F Berizzi, M Martorella, and E.D. Mese. High Range Resolution Multichannel DVB-T Passive Radar : Aerial Target Detection. In *2011 Tyrrhenian International Workshop on Digital Communications - Enhanced Surveillance of Aircraft and Vehicles*, pages 129–132, 2011.

[32] J Fawcette. Vulnerable radar seeks a safe sanctuary. *Microwave Systems News*, 1980.

[33] JS Bailey and GA Gray. Sanctuary Signal Processing Requirements. *Circuits, Systems and*, 75(C):1–6, 1977.

[34] M. Buchbinder, F. Esposito, and H. Perini. SANCTUARY RECEIVE ANTENNA SYSTEM. In *Antennas and Propagation Society International Symposium, 1980*, number 1, pages 146–149, 1980.

[35] R. Klemm. Introduction to space-time adaptive processing. *Electronics Communication Engineering Journal*, 11(1):5–12, 1999.

[36] Richard Klemm. *Principles of Space-Time Adaptive Processing*. IET, 2002.

[37] KP Ong. *Signal processing for airborne bistatic radar*. Phd, University of Edinburgh, 2003.

[38] F. Colone, M Labriola, and F Poli. A pre-Doppler approach for reduced loss bistatic STAP. *Radar, 2006. CIE'06.*, 22:8–11, 2006.

[39] William L Melvin and Senior Member. Adaptive Cancellation Method for Geometry-Induced Nonstationary Bistatic Clutter Environments. *IEEE Transactions On Aerospace And Electronic Systems*, 43(2), 2007.

[40] X. Meng, T. Wang, J. Wu, and Z. Bao. Bistatic clutter analysis and range ambiguity resolving for space time adaptive processing. *IET Radar, Sonar & Navigation*, 3(5):502, 2009.

[41] L E Chevalier. Space-time processing for bistatic radar. *ReCALL*.

[42] WL Melvin and MJ Callahan. Bistatic STAP: application to airborne radar. *IEEE Radar Conference*, 2002.

[43] Johan R. Rasmusson, Martin Blom, B. Flood, P.-O. Frolind, A. Gustavsson, T. Jonsson, Björn Larsson, Gunnar Stenström, and L.M.H. Ulander. Bistatic VHF and UHF SAR for urban environments. *Proceedings of SPIE*, 6547:654705–654705–12, 2007.

[44] A Barmettler, L Zuberbuhler, and E Meier. Swiss Airborne Monostatic and Bistatic Dual-Pol SAR Experiment at the VHF-Band. *2008 7th (EUSAR)*, pages 2–5, 2008.

[45] L.M.H. Ulander, A Barmettler, B. Flood, P.-O. Frolind, a. Gustavsson, T. Jonsson, E. Meier, J. Rasmusson, and G. Stenstrom. Signal-to-clutter ratio enhancement in bistatic very high frequency (VHF)-band SAR images of truck vehicles in forested and urban terrain. *IET Radar, Sonar & Navigation*, 4(3):438, 2010.

[46] R. Baque, P. Dreuillet, O.R. du Plessis, H. Cantalloube, L.M.H. Ulander, G. Stenstro, T. Jonsson, and A. Gustavsson. LORAMbis A bistatic VHF/UHF SAR experiment for FOPEN. *2010 IEEE Radar Conference*, pages 832–837, 2010.

[47] R. Baque, P. Dreuillet, and OR du Plessis. Results of the LORAMbis bistatic VHF/UHF SAR experiment for FOPEN. *2011 IEEE Radar Conference*, 2011.

[48] Wang Chao, Wang Yongliang, Li Rongfeng, and Fan Xikun. On Concept and SCR of PCL AEW Utilizing Illuminators of Opportunity. In *International Conference on Radar 2006*, pages 1–3, 2006.

[49] D.K.P. Tan, M. Lesturgie, Hongbo Sun, and Yilong Lu. Target detection performance analysis for airborne passive bistatic radar. In *2010 IEEE International Geoscience and Remote Sensing Symposium*, number 1, pages 3553–3556, 2010.

[50] Danny Kai Pin Tan, Marc Lesturgie, Hongbo Sun, and Yilong Lu. Signal analysis of airborne passive radar using transmissions of opportunity. *Proceedings of 2011 IEEE CIE International Conference on Radar*, pages 169–172, October 2011.

[51] M. Malanowski, K. Kulpa, and Jacek Misiurewicz. PaRaDe - PAssive RAdar DEmonstrator family development at Warsaw University of Technology. In *2008 Microwaves, Radar and Remote Sensing Symposium*, pages 75–78. IEEE, September 2008.

[52] M. Malanowski and K. Kulpa. Digital beamforming for Passive Coherent Location radar. In *IEEE Radar Conference 2008*, pages 1–6, 2008.

[53] Bartek Dawidowicz and Krzysztof S. Kulpa. Experimental results from PCL radar on moving platform. *2008 International Radar Symposium*, pages 1–4, May 2008.

[54] K. Kulpa, M. Malanowski, P. Samczynski, J. Misiurewicz, and M. Smolarczyk. Onboard PCL systems for airborne platform protection. In *2011 Tyrrhenian International Workshop on Digital Communications - Enhanced Surveillance of Aircraft and Vehicles*, number 1, pages 119–122, 2011.

[55] K. Kulpa, M. Malanowski, P. Samczynski, and B. Dawidowicz. The concept of airborne passive radar. *2011 Microwaves, Radar and Remote Sensing Symposium*, pages 267–270, August 2011.

[56] B. Dawidowicz, K. Kulpa, and M. Malanowski. Suppression of the ground clutter in airborne PCL radar using DPCA technique. In *2009 European Radar Conference*, pages 306 –309, 2009.

[57] B. Dawidowicz, K.S. Kulpa, M. Malanowski, J. Misiurewicz, P. Samczynski, and M. Smolarczyk. DPCA Detection of Moving Targets in Airborne Passive Radar. *IEEE Transactions on Aerospace and Electronic Systems*, 48(2):1347–1357, 2012.

[58] J. Raout, a. Santori, and E. Moreau. Spacetime clutter rejection and target passive detection using the APES method. *IET Signal Processing*, 4(3):298, 2010.

[59] CH Page. The international system of units (SI). 1974.

[60] J.D. Kraus and R.J. Marhefka. *Antennas for All Applications*. McGraw-Hill, 2003.

[61] GH Millard. The introduction of mixed polarization for vhf sound broadcasting: The Wrotham installation. Technical report, BBC, 1982.

[62] Eugene F. Knott, John F. Shaeffer, and Michael T. Tuley. *Radar Cross Section*. SciTech Publishing, 2004.

[63] PicoTechnology. PicoScope 4000 Series.

[64] QRP2000 USB-Controlled Synthesizer, 2012.

[65] RG Vaughan, NL Scott, and DR White. The theory of bandpass sampling. *Signal Processing, IEEE*, 39:1973 – 1984, 1991.

[66] D. W. O'Hagan and C. J. Baker. Passive Bistatic Radar (PBR) using FM radio illuminators of opportunity. *2008 New Trends for Environmental Monitoring Using Passive Systems*, pages 1–6, October 2008.

[67] *Cherokee Archer II Pilot s Operating Handbook*. Number 761. Notre Dame Pilot Initiative, 2004.

[68] BBC. BBC National FM Radio Stations.

[69] Ofcom. Technical Parameters for UK VHF, MF and DAB Transmitters.

[70] BBC. BBC Local FM Radio Stations.

[71] F Colone R Cardinali, P Lombardo O Crognale, and A Cosmi A Lauri T Bucciarelli. Space-time constant modulus algorithm for multipath removal on the reference signal exploited by passive bistatic radar. (November 2008), 2009.

[72] William L Melvin and James A Scheer. *Principles of Modern Radar: Advanced Techniques*. SciTech, 2012.

[73] J. Treichler and B. Agee. A new approach to multipath correction of constant modulus signals. *IEEE Transactions on Acoustics, Speech, and Signal Processing*, 31(2):459–472, April 1983.

[74] F. Colone, D. W. O'Hagan, P. Lombardo, and C. J. Baker. A Multistage Processing Algorithm for Disturbance Removal and Target Detection in Passive Bistatic Radar. *IEEE Transactions on Aerospace and Electronic Systems*, 45(2):698–722, April 2009.

[75] K. Kulpa. The CLEAN type algorithms for radar signal processing. *2008 Microwaves, Radar and Remote Sensing Symposium*, pages 152–157, September 2008.